4D Control of Tissue Development and Blood Vasculature using Photo-mediated Chemistries

Christopher Kenji Arakawa

A dissertation

submitted in partial fulfillment of the

requirements for the degree of

Doctor of Philosophy

University of Washington

2018

Reading Committee:

Cole A. DeForest, Chair

William M. Mahoney

Ying Zheng

Program Authorized to Offer Degree:

Bioengineering

University of Washington

Abstract

4D Control of Tissue Development and Blood Vasculature using Photo-mediated Chemistries

Christopher Kenji Arakawa

Chair of the Supervisory Committee:

Cole A. DeForest

Department of Chemical Engineering

Organ function relies on the synergistic interactions and conserved organization between all its system components. Blood, blood vessels, extracellular matrix (ECM), and parenchyma interact dynamically, existing in a state of constant cross-talk and regulation. Yet for all we have discovered about physiologic and pathophysiologic organ function, our capacity to recapitulate these events has been limited. Currently, there does not exist the necessary set of tools required to create *de novo* tissues or organs. This thesis aims to address these pertinent hurdles in tissue engineering by exploring new means to generate complex tissues using a combination of tunable synthetic hydrogels and photo-mediated chemistries. A preliminary data section followed by two main aims outline these goals. In the preliminary data section, the interactions between matrix and parenchyma are investigated by creating 3D tissues from human pluripotent stem cells (hPSC) encapsulated within tunable cytocompatible poly(ethylene glycol) (PEG) hydrogels

formed via strain-promoted azide-alkyne cycloaddition (SPAAC). In this section, material and cellular variables are optimized to both create functional cardiac tissues from hPSC-derived cardiomyocytes (CM) using PEG hydrogels as well as first maintain and then differentiate hPSCs into mesodermal-derived tissues within fully defined synthetic matrices. As these tissues require vascularization to be supplied with adequate oxygen and nutrients, we were then motivated to explore of the interactions between vasculature and parenchyma. In aim 1, a novel photodegradation-based vascular fabrication methodology is developed, wherein PEG hydrogels are modified with a photodegradable ortho-nitrobenzyl moiety. Combining this novel material with a programmable multiphoton laser, blood vessels are generated with complete 4D control to create multicellular vascularized tissues with some of the most complex vessel networks to date. These devices feature single-micron fabrication resolution, intraluminal structures, and interconnected hierarchical branching networks. To expand our methodology to naturally occurring polymers and to investigate the interactions between blood and vasculature, in aim 2, we develop a multiphoton photoablation fabrication technique and in the process create the first *in vitro* engineered human capillaries. Utilizing these devices, we then study the physiological and pathophysiological hemodynamics associated with severe malaria, probing the mechanisms that give rise to microvascular occlusion and sequestration during infection. Findings here demonstrate the first human model of microvascular sequestration with insights into the biophysical and biomolecular contributions of infected red blood cells to malarial disease. Together this work systematically identifies the gaps in our knowledge to create complex tissues and addresses them by inventing and rigorously testing new photo-mediated fabrication techniques. Work here to construct 3D tissues with complete synthetic control and to generate complex vascular networks permits the study of intricate interactions between all organ system

components. These findings represent the first of many mechanisms once observed only in *in vivo* systems which can now be recapitulated in a dish with greater control of all cellular and structural variables.

Acknowledgements

While the work presented here is a testament of my life as a Ph.D. student, it has only been made possible through the whole-hearted love, support, and guidance of my family, friends, and mentors. I cannot begin to express my gratitude to each and every one of you. You are all are the most important aspects of my life, and I am always humbled to be surrounded by so many incredible people.

First and foremost, I would like to thank my Ph.D. advisor, Dr. Cole DeForest, for his absolute support and guidance throughout my time at UW. Cole, you are and continue to be a positive, enthusiastic, and brilliant mentor dedicated to the well-being of your students. Thank you for always being a role-model of the ideal academic and always being willing to grab a beer or literally jump for joy when I've come to you with good news. Your ever curious and encouraging outlook on science and research is infectious. I am so incredibly thankful to have been a part of the DeForest Lab.

Thank you to my co-mentor and collaborator Dr. Ying Zheng. Ying, your smile, laugh, positive attitude and confidence in me as a researcher has made my Ph.D. experience fun, thought-provoking, and an absolute joy. I feel so fortunate to have been able to work with you and the entire Zheng lab. Thank you for your generosity and mentorship throughout my time as a graduate student.

In addition to my Ph.D. advisors, I have been privileged to have been able to work with so many incredible mentors and collaborators throughout my training here at UW. Research, science, and medicine hinges on strong, active, and fun collaborations. I feel that I have learned

so much from each of you. Thank you to Dr. Benjamin Freedman, Dr. Chuck Murry, Dr. Bill Mahoney, Dr. Dan Ratner, Dr. Joe Smith, Dr. Jill Watanabe, Dr. Dale Hailey, Dr. Doug Paauw and Dr. Jamey Cheek. I hope that I can one day be as phenomenal of a mentor and role model to others as you have all been to me.

To my labmates (Emily Ruskowitz, Celina Gunnarsson, Caitlin Howard, Barry Badeau, Surya Kotha, Jared Shadish, Christian Mandrycky, Yoon Jung Choi, Eric Yang, and Sam Rayner), my medical school classmates (Daniel Oh, Maria Islam, Takashi Sakano, Alisha Wang, and Danee Hidano) and my friends (Shivani Dharmaraja, Kevin Tan, Byron Kwan, Tina Zhou, Lan Tran and Brian Lee) thank you for always being there for the highs and lows of grad school. You guys are the best and I would not made it through my Ph.D. without you!

Most importantly, thank you to my parents Patrick and Makiye Arakawa and to my entire family for your unconditional love and support. Throughout my life, you have encouraged me to pursue all of my many interests. Along the way, you've lead by example, teaching me to value people above all else. You and the principles you've instilled in me have made me the person I am today.

TABLE OF CONTENTS

LIST OF FIGURES

CHAPTER 1: INTRODUCTION AND SIGNIFICANCE

While it is natural that we take a reductionist approach to study biology, no tissue in the human body is comprised of a single type of cell nor do any consist of an individual monolayer. Organs and tissues are arranged in complex but conserved 3D architectures consisting of a myriad of cells, biomacromolecules and fluids, constantly interacting and dynamically changing with time. They are constructed from not only cells but are encased in extracellular matrix, a mixture of proteins, glycosaminoglycans, and bioactive molecules. This matrix provides structural and biochemical support, allows for cell adhesion and cell-cell communication and can initiate differentiation[1]. Through these blocks of matrix and cells traverse a network of interconnected blood vessels delivering nutrients to and removing wastes from their microenvironment[2]. Blood constituents within those vessels deliver biochemical signaling factors from distant organs, support wound healing and repair, and provide immunological protection from pathogens[3]. Only when vasculature, matrix, healthy tissue, and blood exist together and work cooperatively can organ function be sustained.

These elements of vasculature, matrix, tissue, and blood are the building blocks of life and develop early during embryogenesis as they are necessary to sustain multicellular organismal function. Matrix exists immediately upon embryo development, followed shortly thereafter by cellular compartmentalization and organization at or before the blastula stage (day 3.5), while the heart, vasculature, and premature blood develop as tissues begin to exceed the limits of diffusion (~2 weeks)[4]. As a consequence of an intricate choreography of thousands of individual

bioactive molecules at the correct concentrations in both space and time, reproducible organogenesis spontaneously occurs[5]. This system of vessels, tissues, and matrix persist into adulthood and must be maintained to sustain life. Uninterrupted blood flow, delivery of nutrients, matrix regulation and remodeling, and hierarchical tissue organization are all critical components. Pathological perturbations resulting from infectious disease, chronic disease, or trauma can dramatically hinder proper function.

Yet for all we have discovered about normal physiology and despite the many observations made throughout history about endogenous stages of tissue regeneration, our capacity to recreate those events to better understand pathogenesis or replace those tissues after insult have been limited and crude. Conventional molecular biology techniques have been utilized exhaustively to understand observed biological phenomena, however there simply does not exist a toolbox of techniques to build tissues from the ground up. To not only better understand this complex system and those diseases which afflict it, but to also create replacement tissues *in vitro*, we must develop novel means to probe, tune, and control biology in both space and time. We must consider not only the cellular components of tissue function but must address practical limitations of nutrient delivery, architectural organization, and the interplay of many different tissues together if we are to truly build a functional organ system.

In this thesis, I will introduce several novel tools which I have utilized to build complex tissues and better understand the interactions between blood, vasculature, and parenchyma. I will demonstrate how these tools have been used in the construction of 3D tissues, vascularization of tissue engineered constructs, and the study of pathological perturbations in the setting of infectious disease. I will first outline the relevant history of tissue engineering and regenerative

medicine, and then demonstrate experimentally how I have used photoresponsive biomaterials and photochemical techniques to shed new light on these biological phenomena.

CHAPTER 2: REVIEW OF LITERATURE

Modified from *Biology and Engineering of Stem Cell Niches*, Elsevier. 295-314 (2017)[6]

A. Extracellular Matrix

The extracellular matrix is a non-cellular proteinaceous scaffolding which is present in all organs and tissues, dictates tissue architecture and mechanics, is rich with cell-signaling factors, and is necessary to sustain multicellular organism life[1]. Constructed from about 300 glycosaminoglycans and proteins, known as the core matrisome[7], matrix composition can vary drastically as it is tailored to be organ-specific. Mechanically, ECM derived from different tissues in the human body can span a stiffness range of greater than eight orders of magnitude, demonstrate various degrees of viscoelasticity, and vary dramatically in their water content[8]. Biologically, ECM proteins are known to trigger cell signaling events resulting in differences in attachment, proliferation, survival, and even differentiation[9]. These biological differences are a result of direct interactions between cell surface receptors and ECM proteins, as well as through the sequestration of growth factors (epidermal growth factor, fibroblast growth factor, Wnts and others) through both nonspecific and specific binding events[10].

Direct ECM-cell interactions are largely conveyed and interpreted through the specialized cell adhesion molecule family of integrins[11]. These heterodimeric proteins consist of a single α and β subunit which upon complexation form a single integrin receptor. As often α and β subunits comprise both the intracellular and extracellular domains, signal transduction and ECM

specificity are unique to the combination of subunits[12]. Intracellularly these signals can be transmitted through a number of different kinases including those of the focal adhesion kinase and Src kinase families[13].

Though often overlooked, ECM composition and structure are not static. This dynamic microenvironment can undergo drastic turnover and be significantly altered when balance of ECM production and remodeling is disturbed. Matrix proteins, for example, play a critical role in the stabilization of wounds upon injury and can heal in dramatically different ways depending on the nature of the injury[11]. Degradation and remodeling are largely attributed to enzyme-cleavable domains within ECM proteins and their enzyme counterpart, the matrix metalloproteinase (MMP). This >28 member family of calcium-dependent zinc-containing endopeptidases is thought to play a major role in cell proliferation, migration, angiogenesis, host defense, cancer biology and cell differentiation as MMPs can release bound growth factors and directly alter the properties of the matrix surrounding the cell[14].

B. Hydrogels for 3D Cell Culture and Tissue Engineering

1. Introduction

As made evident through the description of ECM proteins and scaffolding, all cells and tissues *in vivo* exist in a dynamic 3D microenvironment that is in constant flux. As such, it is natural that *in vitro* experiments should likewise be conducted in 3D. While the majority of biological research today remains grounded in 2D experiments in which cell culture is performed on a monolayer of cells cultured on plastic, overwhelming evidence has shown that cell behavior in development, cancer, and general cell culture is more native in 3D as compared with traditional 2D culture[15]. This should come as no surprise as cell polarity, substrate stiffness,

signaling density, and even diffusion are all inherently and obviously abnormal when cells are cultured on tissue culture plastic. To better recapitulate human cell function, a new platform in which cell culture and experimentation can be performed is necessary.

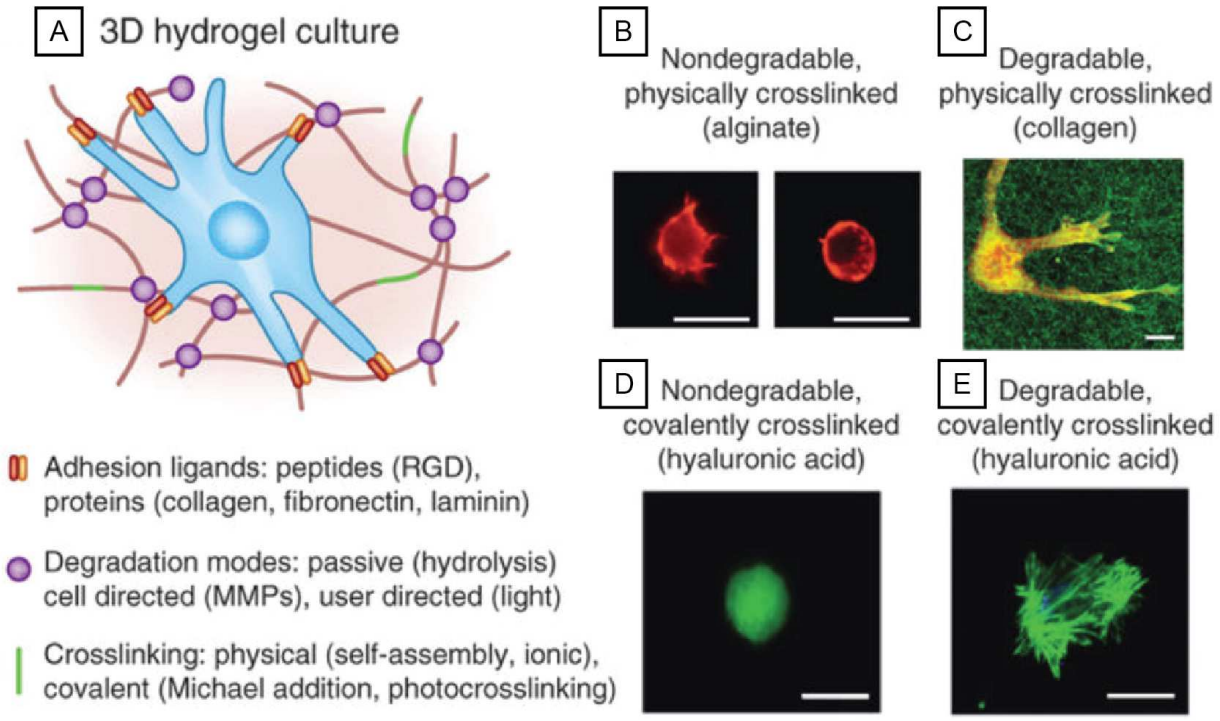

Figure 2-1: Variable aspects of 3D hydrogel culture platforms

Adhesion ligands, degradation modes, and crosslinking of hydrogels vary based on hydrogel chemical composition. B) Mouse mesenchymal stem cells (MSC) cultured in both soft (left) and stiff (right) alginate gels demonstrate round morphology. C) Bovine fibroblasts spread within degradable type 1 collagen hydrogels at low stiffness. D-E) human MSCs cultured in hyaluronic acid hydrogels crosslinked with nondegradable (D) or degradable (E) peptide crosslinkers demonstrate rounded and spread morphology respectively. Figure adapted from Caliari et al.[16].

One of the most successful demonstrations of a biomimetic 3D culture platform to date is the polymeric hydrogel[17]. These water-swollen interconnected crosslinked networks exhibit tissue-like elasticity, can form under mild conditions, and allow for adequate mass transport of

nutrients through its matrix. In addition to their defining qualities as a class of materials, hydrogel networks furthermore allow for alteration of their biochemical and physical properties[18] depending on their chemical composition, the reaction mechanism utilized to initiate gelation as well as the crosslinking density upon reaching reaction equilibrium[19] (**Figure 2-1**). Crosslinking density is especially critical as polymer network and rubber elasticity theory can be used to predict and relate mechanical modulus, water content, and diffusivity of a molecule traversing through the polymer network.

Here I classify polymeric hydrogels as either naturally derived or synthetic based on the origin of their prepolymer constituents. Emphasis has been placed on those hydrogels and biomacromolecules utilized in this thesis.

2. Naturally Derived Hydrogels

Due to their undisputed success through evolutionary development, natural-based materials are popular choices when generating and utilizing biomaterials to study and understand cell function, build tissues, and create *in vitro* models of disease. As both the building blocks and final structure exist within nature, naturally derived biomaterials have evolved to support cell adhesion, proliferation, migration, and differentiation by binding their natural receptors and epitopes[15]. Furthermore, these materials exhibit little toxicity, incur minimal inflammatory responses, function and are stable in physiological conditions, and are often biodegradable and bioactive[20]. For these reasons, natural biomaterials are useful for both tissue engineering applications and especially for the culture of embryonic stem cells.

Yet also as a consequence of harvesting these biomacromolecules from their native tissues, commercially available polymers vary significantly in molecular weight and purity.

Moreover, processing to generate usable constructs results in extensive variability in chemical modification, minimal control over chemical structure, biochemical signaling, mechanical properties, and microarchitectural organization and design. The factors which make naturally based biomaterial successful cannot be decoupled from their inherent properties and thus studying specific mechanisms and biological cues are extremely difficult if not impossible.

a) Collagen

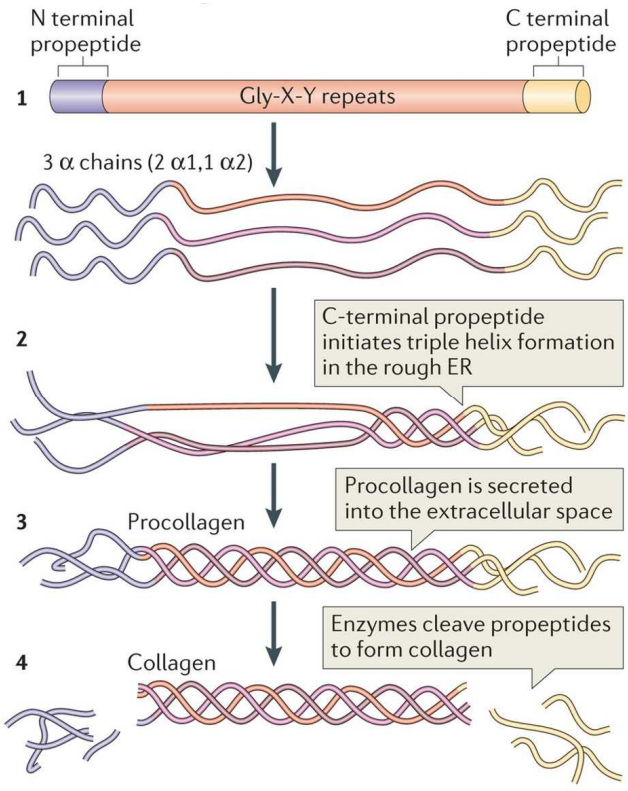

Figure 2-2: Molecular structure of collagen

1) The individual collagen molecule is constructed from a series of GXY repeats flanked by amino- and carboxy-terminal propeptide sequences. Together three α chains form the triple helix structure of procollagen and collagen. 2) Inside the rough endoplasmic reticulum of a cell, 2 α1 chains and one α2 chain begin helix formation at the c-terminal end to form procollagen. 3-4) Procollagen is then secreted into the extracellular space where metalloproteinase enzymes cleave the amino- and carboxy-terminal propeptides to form the mature collagen molecule. Figure adapted from Mouw et al.[21].

Of the myriad of naturally occurring biomaterials, collagen is perhaps the most widely utilized. Collagens represent a family of fibrous proteins found in nearly every mammalian tissue that provide mechanical support and structural integrity to the ECM. Though collagen production and secretion by resident fibroblasts is highly expressed in load-bearing tissues such as tendon and bone, these proteins are also abundant in skin, cartilage, and a number of internal organs.

At least 28 isoforms of collagen have been identified, composed of >40 distinct polypeptide chains[22]. Over 90% of the collagen in the human body is of Type I, which is found in skin, tendon, vascular ligature, and bone. Type II is derived from cartilage; III from reticular fibers in skin and blood vessels; IV from basement membrane, and V from cell surfaces as well as hair. Common to all types, collagen molecules self-assemble from three α chains as a result of their molecular structure (**Figure 2-2**). Each polyproline peptide α chain contains thousands of repeats of the -X-Y-Gly- sequence, where X and Y can be any amino acids but are most commonly proline and non-proteinogenic hydroxyproline (Hyp) residues that drive left-handed chain helicity[23]. The glycine residue is critical in enabling tight packing and assembly of three α chains into a single tropocollagen molecule, a right-handed triple helix-containing structure stabled by intermolecular hydrogen bonding. The tropocollagen rods can self-assemble with a quarter-staggered structure into fibrils which further self-assemble into inelastic load-bearing collagen fibers with low extensibility (~15%) that provide structural support to many mammalian tissues[24].

b) Matrigel/Geltrex

Matrigel® is perhaps the best known and most successful natural-based ECM coating utilized to culture pluripotent stem cells and is comprised of a heterogeneous mixture of

gelatinous proteins that are secreted and isolated from Engelbreth-Holm-Swarm (EHS) mouse sarcoma cells[25]. Laminin, collagen, and entactin are the primary protein species present, though proteoglycans and growth factors (*e.g.*, transforming growth factor β, epithelial growth factor) are also abundant[26]. As Matrigel and its commercial competitor Geltrex® are an amalgamation of numerous proteins and glycosaminoglycans, the factors most critical to ensure hPSC survival and attachment are largely unknown. Furthermore, while it is clear that hPSCs remain pluripotent when cultured on either substrate, the contribution of each of its many factors cannot be determined. Finally, though cell response to heterogeneous protein mixtures like Matrigel® and Geltrex is generally quite favorable, it should be noted that these materials vary significantly from lot to lot and may not be appropriate for experiments where knowledge of precise material composition is required.

3. Synthetic Biomaterials

As cell types, function and application vary dramatically on a case-by-case basis, many believe specifically tailored materials are necessary to truly optimize function and understand the factors which govern biological function. In this respect, synthetic materials have unique advantages over their naturally derived counterparts including: precise tuning over material properties (e.g., matrix biofunctionalization, network stiffness), no concern over batch-to-batch variability influencing cell function as the material is chemically defined, and selective inclusion properties absent from natural materials (e.g., stimuli-responsivity)[15,17].

a) PEG based materials structure and unique properties

Poly(ethylene glycol) (PEG) is among the most well-understood and utilized synthetic polymers and has been FDA approved as a material for numerous implantable devices, surface coatings, and polymer drug conjugates. PEG is hydrophilic, unlike polybutylene oxide or polymethylene oxide (polymers containing one more or one less methylene group than PEG, respectively)[27]. This unique property is believed to be a product of the specific length of the PEG polymer that allows for thermodynamically favorable interactions with individual water molecules. As a result, PEG chains create a "hydrated" layer[27], masking the underlying bulk material and protecting it from proteins, including blood coagulants, cell surface binding motifs, and antibodies[28]. PEG is furthermore extremely versatile as it can be readily be chemically modified with a myriad of functional groups, used to create complex dendrimers and polymers with well-defined molecular weights, and altered to promote cell attachment or protein conjugation. In tissue engineering and stem cell culture, PEG hydrogels have emerged as one of the most successful synthetic polymer systems, paving the way to study and understand effects of the extracellular niche on stem cell fate. Early research concentrated on the development of PEG diacrylate monomers crosslinked together through thermo- or photopolymerization[29]. While non-degradable in its most basic form, PEG polymers can be crosslinked using degradable polymer or peptide chain crosslinkers to become biodegradable or can be conjugated with pendant conjugates to become more bioactive. Using these and many other techniques, PEG hydrogels have been optimized to culture stem cells from functional cartilage, bone, neural tissue, and pancreatic islets[30].

b) Click chemistry-based polymerization

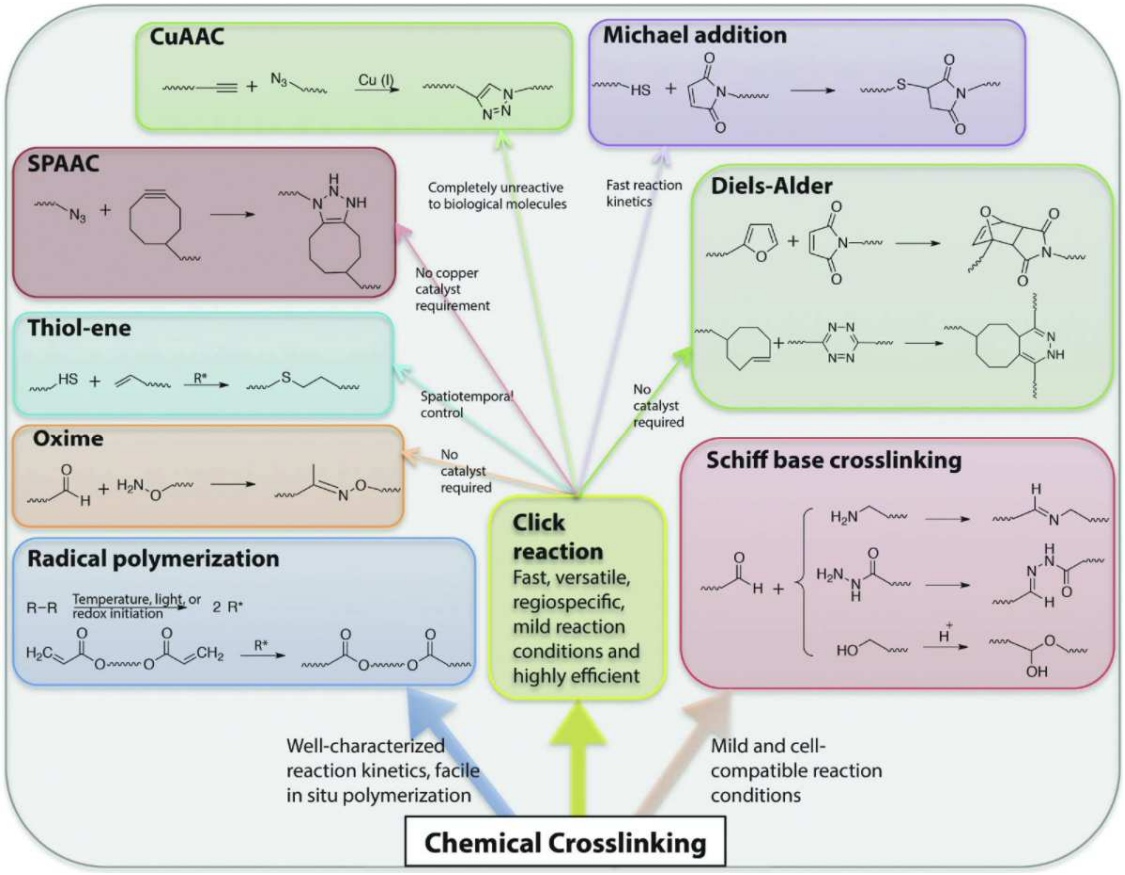

Figure 2-3: Chemical methodologies of hydrogel formation or post-polymerization modification

Demonstrated are a wide variety of chemical reactions utilized to functionalize, crosslink, or modify hydrogel networks. Classified as either radical polymerization, click reaction, or Schiff base crosslinking, each methodology demonstrates unique advantages and disadvantages in regard to either its use or synthesis. Figure adapted from Kharkar et al.[31].

While many means to initiate hydrogel formation exist, few are as powerful or as versatile as click chemistry-based polymerization. Click chemistry, first introduced by K. B. Sharpless in 2001, describes a set of reactions which all proceed with high yields, occur quickly, are regiospecific, and simple to perform[32]. For their ease of use, speed and efficiency, click chemistry based hydrogel formation has become an extremely popular[19,33,34]. Examples of click-

reaction based hydrogels in bioengineering include but are not limited to the copper(I)-catalyzed azide-alkyne cycloaddition (CuAAC), thiol-ene, Diels-Alder, oxime, and strain-promoted azide-alkyne cycloaddition reactions[31] (**Figure 2-3**). Attributed to their specificity upon reaction, many of the aforementioned mechanisms are especially powerful when utilized in tissue engineering as they are also regarded as bioorthogonal[35], or able to occur in or around a living system without interfering with native biochemical processes. Afforded by their bioorthogonal nature and as compared with other polymerization schema, including widely utilized free-radical polymerization methods, in which noxious free radicals are utilized to propagate polymerization, many click-based polymerization reactions are considered completely cytocompatible. Work by ourselves and others has demonstrated that these click-based hydrogels can be formed in the presence of live cells with little to no impact on cell viability or function[19].

4. Stimuli Responsive biomaterials

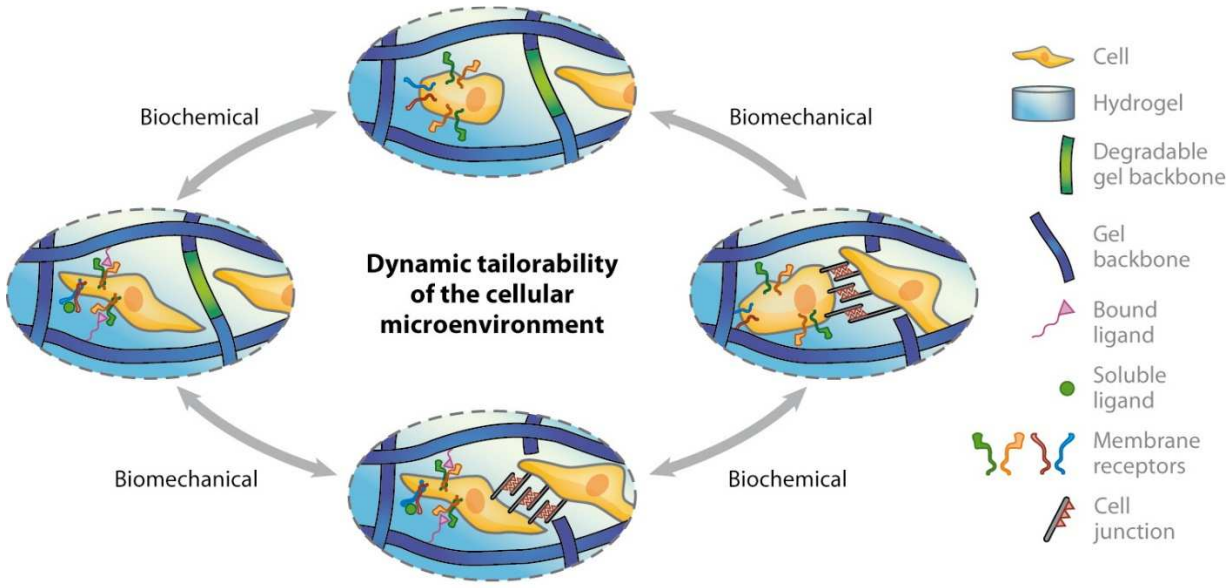

Figure 2-4: Stimuli responsive materials to tune the cellular microenvironment

Through the development of stimuli responsive materials, the biomechanical, biophysical, and biochemical properties of the cellular microenvironment can be modified with respect to both space and time. By utilizing bioorthogonal chemistries single aspects of the microenvironment can be tuned independently. These advancements seek to recapitulate the dynamic nature and function of a cell *in vivo*. Figure adapted from DeForest et al.[17].

In addition to those standard properties of hydrogels, through the introduction of stimuli responsive agents it is possible to tune and alter hydrogel properties on command (**Figure 2-4**). Biochemical, biomechanical, and structural changes can be incurred upon the delivery of the predetermined cues. These "smart materials" can respond to factors introduced by cells within the matrix, external stimuli, or changes to the hydrogel microenvironment.

a) Enzyme-Degradable Polymers

Just as the natural ECM can be remodeled, rebuilt, and redesigned by the native cell population, synthetic smart biomaterials can also be modified by cells grown on or within its

matrix. This cell-mediated degradation is critical for cell survival, cell proliferation and whole tissue regeneration[36]. To accomplish this goal, tissue engineers leverage differential expression of proteinases, present in either the local microenvironment of implantation or by a specific cell type. Specifically, the matrix metalloproteinase (MMP) family of enzymes is considered when designing degradable materials. Approximately 30 different MMP's have been identified and both enzymes and their substrates have been well-studied and documented. Extensive work by Nagase et al.[37] and the Hubbell research group[38] have identified specific peptide sequences which can be utilized for the design of smart enzyme-degradable cell culture platforms. By utilizing enzyme-degradable peptides as crosslinking agents in otherwise non-degradable materials, cells can more readily degrade the artificial microenvironment and replace it with their own naturally occurring matrix[30]. These MMP-cleavable crosslinking agents have become a cornerstone of most hydrogel platforms[39]. Plasmin-, collagenase-, and other enzyme-labile sequences have also been incorporated into biopolymer systems to yield biodegradable culture systems[40].

b) Photoresponsive Polymers

Light is a unique stimulus, allotting exquisite spatiotemporal control and a non-invasive means of initiating change within a given material. Over the past decade, significant research has been conducted to generate chemistries capable of leveraging our understanding of light and optics for tissue engineering purposes[18]. In particular photolysis, or the use of light to degrade a material or chemical tether has been studied for on-demand drug delivery, scaffold fabrication, and the generation of materials with tunable mechanical properties[41]. These linkers include, *o*-nitrobenzyl esters, diphenyliodonium carboxylates, coumarin methyl esters and their derivatives

each of which degrade when subjected to a specific wavelength of light[18] (**Table 2-1**)[42]. Kinetics of photolysis, products of photocleavage, and reaction biocompatibility are well-understood. Utilizing these linkers in the backbone of hydrogel and scaffold constructs allows for site-specific degradation, while utilizing these molecules as linkers to biotherapeutics allow for on-demand drug release[19,43]. When applied in tissue engineering, photodegradable hydrogels have seen widespread use. We and others have demonstrated exquisite control of photodegradation and alteration of hydrogel properties utilizing light-based chemistries to alter hydrogel architecture, and control cell migration.

Though not explicitly highlighted as part of my thesis research, it is of note that the same spatiotemporal control demonstrated for photodegradation can similarly be utilized for photopolymerization. In particular, light-initiated polymerizations have gained popularity for their ability to encapsulate and deliver cells into complex defects by injection and subsequent transdermal light treatments[44]. Like other radical chain polymerization techniques, photopolymerizable monomers most frequently contain unsaturated vinyl functionalities. By utilizing photoinitiators like riboflavin or Irgacure and the correct wavelength of light, energy is imparted on the initiator and a free radical is generated. This free radical then propagates through unreacted double bonds found in the polymer, producing crosslinks between adjacent polymer chains. It is important to note that cell death may occur either due to the generation of free radicals or from UV light exposure (as many photoinitiators require high energy UV light to initiate polymerization). Significant work has been conducted to utilize visible light or IR responsive photoinitiators, as well as safer water soluble polymers including PEG, chitosan, and gelatin[45–47].

Type of reaction	Functional group or reaction	Representative Mechanism	Relative Rate	4D Cell Culture
Cleavage	Nitrobenzyl	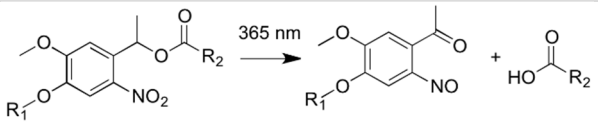	+ +	✓✓✓
	Coumarin	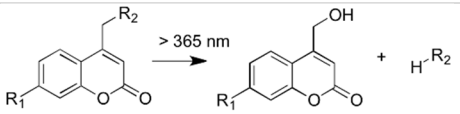	+ + +	✓✓
	Disulfide	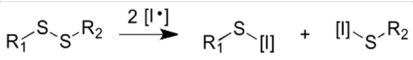	++	✓
Isomerization	Azobenzene	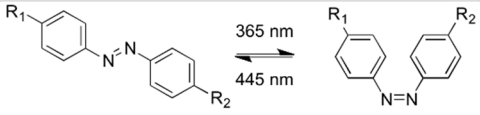	+ +	✓
Addition	Acrylate	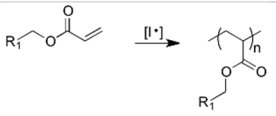	+++	✓✓✓
	Photocaged Michael Addition	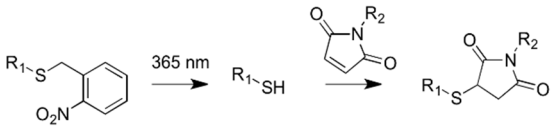	+ +	✓✓
	Thiol-ene	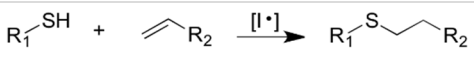	+++	✓✓
	CuAAC	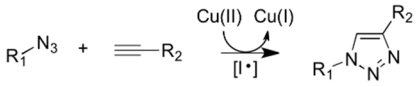	+	✓
	FXIIIa Catalyzed	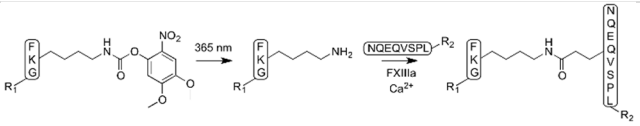	+	✓
	Oxime Ligation	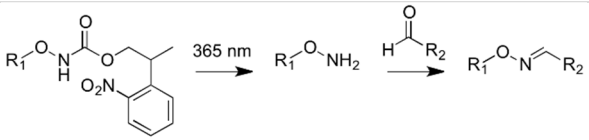	+ +	✓

Table 2-1: Photoresponsive functional groups and their representative mechanisms

Relative reaction rate is indicated with plus signs (+). Relative usage for each reaction for both drug delivery and 4D cell culture is indicated with check marks. Table modified from Ruskowitz et al.[42]

C. Tissue Engineering

As described earlier, great advancements have been made in the field of tissue engineering and regenerative medicine; however, major hurdles remain in the form of vascular engineering and engineering of tissue architecture and development. Here are outlined those approaches developed thus far to direct differentiation and create vasculature.

1. Directed Differentiation of Embryonic Stem Cells

hPSCs have shown significant promise in both regenerative medicine and for *in vitro* disease modeling as both embryonic stem cells and induced pluripotent stem cells have both been shown to be able to differentiate into all three germ layers. Furthermore, directed differentiation protocols have been developed and optimized to generate, among others, heart, kidney, and endothelial cell (EC) types. The capacity to generate and apply these cells and tissues is briefly outlined below.

a) Cardiomyocyte differentiation and tissue engineering

As cardiovascular disease is the leading cause of mortality in the United States, accounting for 1 in 4 deaths[48] increased efforts have been made to create replacement cardiac tissue from renewable stem cell sources. Tissue engineering and regenerative medicine solutions are uniquely necessary in the treatment of cardiac disease as the heart demonstrates an extremely limited intrinsic regenerative capacity. For example, should a patient suffer from a myocardial infarction (MI), a condition which afflicts roughly 720,000 cases/year[49] and carries an associated cost of $190 billion[50], scar formation, and loss of tissue function are almost inevitable. While current medical therapies aim to limit the extent of damage during a heart

attack through rapid perfusion or pharmacologically decreasing oxygen demand, if ischemia persists for >20 minutes, permanent damage ensues. Post-ischemic treatments to improve or maintain heart function are largely limited to either heart replacement or use of a left ventricular assist device. To allow a return to normal function, disinhibited by the effects of MI for these millions of patients, will require artificial intervention through stem cell and tissue-engineering techniques.

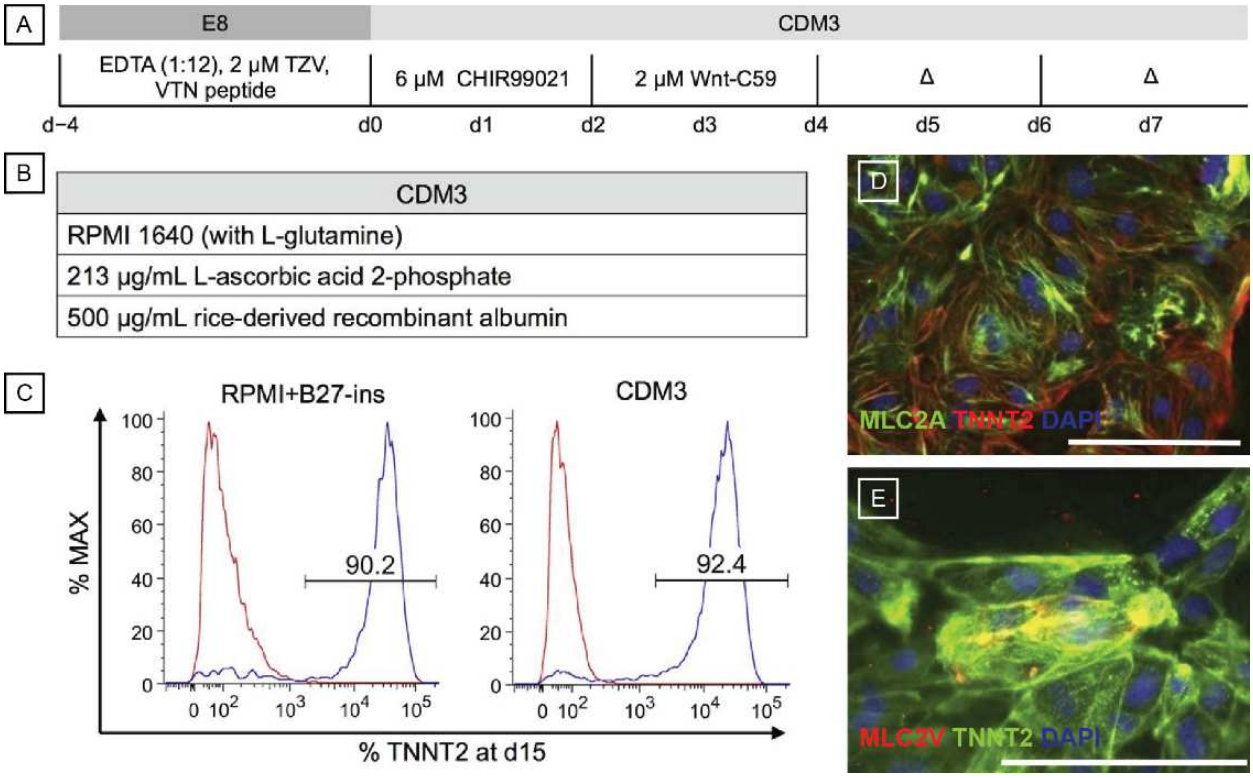

Figure 2-5: Biphasic control of Wnt signaling in hPSCs using defined chemical conditions gives rise to high purity cardiomyocyte populations

A-B) Using only small molecule modulators of the Wnt pathway, hPSCs can be guided toward cardiomyocyte phenotypes with high purity (C). Atrial (D) and Ventricular (E) subtypes were observed in culture. Figure adapted from Burridge et al.[51].

Toward this goal many have found success by learning and borrowing from cardiac developmental biology to direct the differentiation of hPSCs toward cardiac lineages (ventricular, atrial, pacemaking subtypes). Developmentally, the heart arises from the splanchnic portion of the lateral plate mesoderm and first begins to develop on day 18-19 following fertilization. This splanchnic mesoderm then develops into two distinct cell populations: the primary and secondary heart fields. Briefly, mesoderm within this cardiogenic area develops into two cord like structures, which over a three-day period become hollow tubes. Those areas derived from the primary heart field then fuse to form the primitive heart tube (day 21) followed shortly by partial fusion of the cranial portion of the secondary heart field. The primitive heart tube then folds to form a U-shape, then an S shape, before finally septating to emerge as the familiar four-chambered heart. Herein, cells of the primary heart field develop into the atria and left ventricle, while cells derived from the secondary heart field develop into the right ventricle and outflow tracks.

While no *in vitro* human heart tube models have been demonstrated, directed cardiac differentiation has found great success. Historically this has been performed through control of the Wnt, nodal and bone morphogenic protein (BMP) signaling pathways; however, recent findings suggest that only control of Wnt signaling is required (**Figure 2-5**). Thorough research has shown that in the presence of a cocktail of 27 supplementing factors (B27 supplement) and while subjecting cells to a biphasic Wnt activation and repression, differences in nodal and BMP signaling during early mesodermal differentiation can dictate the development of cardiomyocytes, cardiogenic-mesoderm-derived endothelial cells, and hemogenic-mesoderm-derived endothelial cells[52]. However, more recent cardiac-specific differentiation protocols have suggested that adequate cardiac yields can be achieved through control of only Wnt signaling

and can be performed in a simple basal RPMI 1640 (Roswell Park Memorial institute) media supplemented with only L-ascorbic acid 2-phosphate and recombinant human albumin. Extensive characterization of these differentiated cardiomyocytes by electrical conduction, mechanical contraction, protein production and gene expression assays confirm the generation of robust cardiomyocyte populations suggesting that Wnt is indeed the most critical factor necessary for cardiac differentiation[51].

b) Renal Tissue Engineering- Kidney Organoids

Protocols to direct the differentiation of hPSC towards kidney phenotypes have recently made dramatic progress, encouraged largely from a need to treat chronic kidney disease (CKD). Like heart disease, CKD is a major public health problem afflicting 5-10% of the world population and was responsible for approximately 950,000 deaths in 2013[53]. For patients who progress to end-stage kidney disease (ESRD) only two options exist: hemodialysis or transplantation. As a consequence of a lack of viable alternative options, the estimated 3.6 years to find a donor, the graft failure rate even with immunosuppression, and the abysmal 5 year survival rate for long term dialysis[54], great efforts have been made to develop an artificial means to regenerate the kidney and determine new ways to study human kidney development *in vitro*.

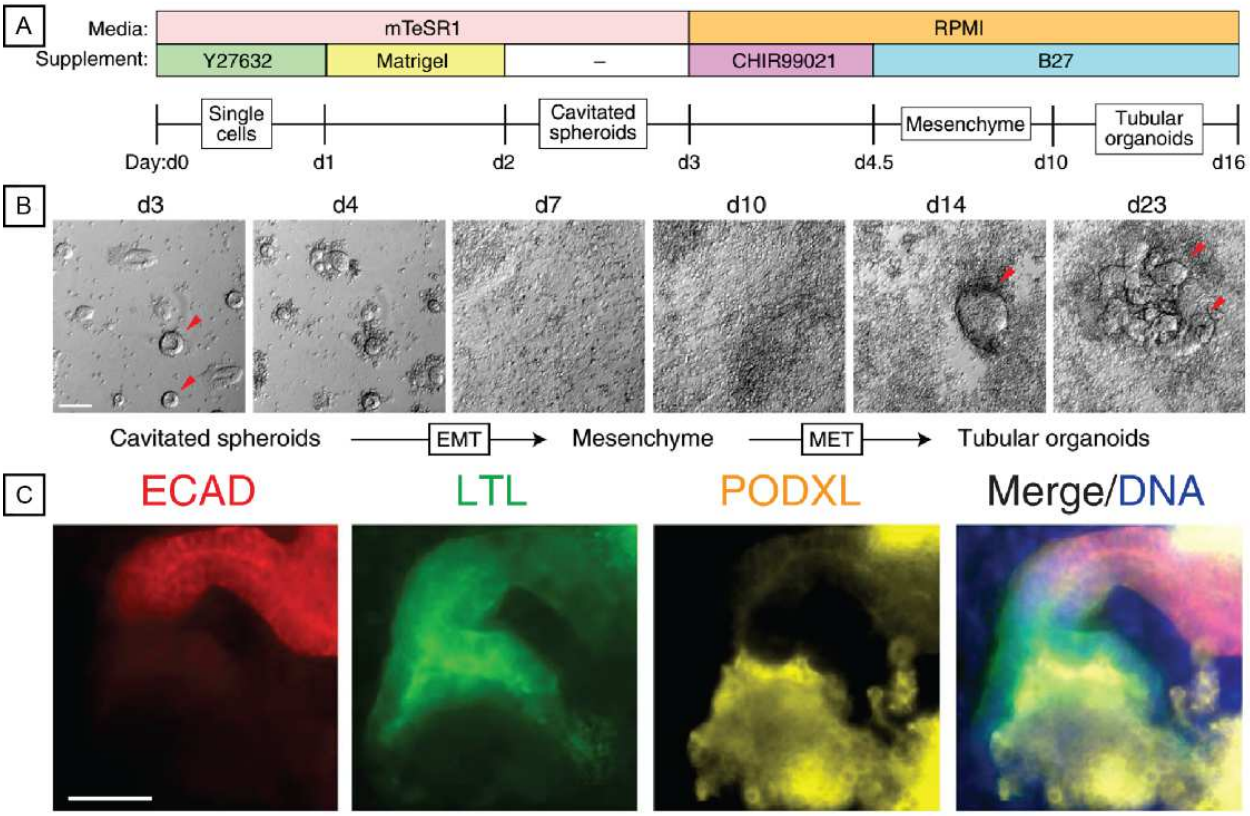

Figure 2-6: Kidney organoids are readily generated from hPSCs by controlling Wnt signaling

By controlling Wnt signaling, Kidney organoids complete with distal tubule ($ECAD^+$), proximal tubule (LTL^+) and podocytes ($PODXL^+$) cell populations could be observed. A critical cavitated spheroid stage was determined to be necessary to initiate kidney differentiation. Figure adapted from Freedman et al.[55].

Developmentally, the final form of the adult kidney arises from two distinct populations of cells known as the metanephric mesenchyme (which gives rise to the glomerulus, proximal tubule, loop of Henle and distal tubule) and the ureteric bud (which gives rise to the collecting duct, renal pelvis and ureter)[56]. Though both initially are derived from the intermediate mesoderm during early embryogenesis, the two diverge both spatially and functionally before reuniting again to become the mature kidney. Upon uniting, interactions between these two tissues beginning at week 10 and ending between weeks 32 and 36 of gestation, are believed to

give rise to the nephron, kidney architecture, and overall organization[57], ultimately permitting for the countercurrent exchange processes necessary for urine concentration and nutrient reabsorption. As one might expect, the developed kidney is thus a complex tissue, containing many different cell types, arranged in a very well-organized manner, with advanced function.

Though a human model for kidney development does not exist and despite the many hurdles facing kidney tissue engineering, recent findings utilizing hPSCs to create kidney derivatives have been groundbreaking. Work by our collaborators and others have demonstrated the capacity for hESCs and hiPSCs to undergo directed differentiation into nephron progenitor cells (NPC)[56,58], ureteric bud derivatives[59,60], and nephron organoids[55,61]. Interestingly, the kidney organoids formed during directed differentiation assume clear tissue organization and tubule formation (**Figure 2-6**). Furthermore, utilization of gene-editing techniques has allowed for the study of genetic disease in these model platforms. The Freedman research group was the first to demonstrate a human model for polycystic kidney disease (PKD) by developing hPSC cell lines containing mutations in both polycystin 1 and polycystin 2[55,62]. By then differentiating those populations into kidney organoids they were able to recapitulate cytogenesis, as observed in PKD patients.

2. Vascular Engineering

While great strides have been made to develop organ specific cell types, all tissue-engineered constructs require a perfusable vasculature. The ability to generate vascularized tissues has become a cornerstone of regenerative medicine and is recognized as a major hurdle which must be addressed in order for tissue engineering constructs to become clinically translational[63]. These vessel networks are not only critical to the supply of nutrients, but play an integral part in organ function, local signaling, long-range paracrine signaling, and critical blood-parenchyma interactions.

To date there have been many attempts to create vascularized tissues with varying degrees of success. Bioprinting, pioneered by the Atala group at Wake Forest, has proposed a ground up approach to organ tissue engineering in which different cellular components can be printed using "bio inks". Utilizing 3D printing, their group can generate nearly scaffold-free organs using only cells[64–66] and has demonstrated that whole tissues can be printed with spatial control of cellular deposition. While these techniques have allotted researchers to generate general arrangement of cells, bioprinting cannot generate vasculature beyond a resolution of 500 μm.

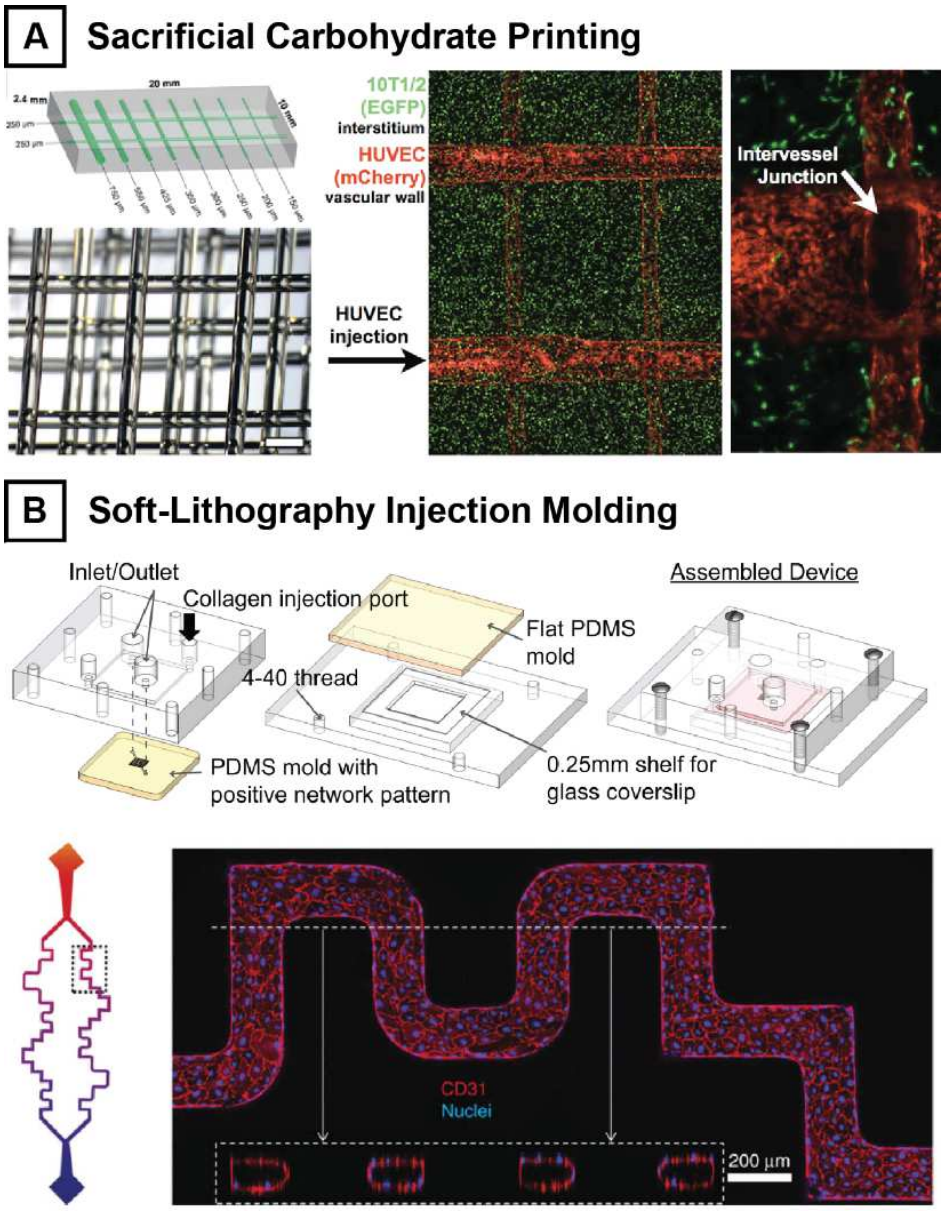

Figure 2-7: Microvascular fabrication techniques

A) Sacrificial carbohydrate 3D printing has been successful in generating interconnected 3D networks in the presence of living cells with fabrication limitations of ~100 µm[67]. B) Soft-lithography injection molding has been utilized to generate stable microvascular fluidic devices with well characterized junctional staining and control of flow and shear stress. Figure adapted from sources[68,69].

In an innovative use of 3D printing, the Chen group at University of Pennsylvania and the Khademhosseini group at UCLA have independently developed means to print sacrificial

polysaccharide-based wires (sucrose and alginate, respectively) generated by vitrification or extrusion and guided using a programmable mechanical dispenser (**Figure 2-7A**)[67,70]. The vascular network is then infiltrated using a hydrogel matrix. The sacrificial wires can then be rapidly degraded leaving patent channels. Though both systems can generate medium-sized >100-200 μm channels, resolution is limited by the brittle mechanical properties of the vitrulized glass or the extrusion process. Furthermore, such channels have limited control of vascular generation in the z-dimension as they require a layer-by-layer approach to build a sacrificial matrix.

One of the most successful demonstration and utilization of microvascular networks to date has been generated using soft lithography, a technique pioneered largely by the Zheng lab (**Figure 2-7B**)[71,72]. Here, a positive polydimethylsiloxane (PDMS) stamp of the vessel network is cast from a lithographically patterned negative silicon wafer master mold. This newly generated stamp and a flat unpatterned PDMS slab are then pushed into concentrated unpolymerized type-1 collagen within a plexiglass jig and allowed to form top and bottom gel pieces containing the vessel design. Subsequent removal of stamps and assembly of top and bottom portions using mechanical pressure seals the channel network. Channels are then endothelialized and vessel networks can be cultured. Using this technique, work has been successful in studying a myriad of physiological and pathologic vessel and blood phenomena including: angiogenesis[73], thrombosis, von Willebrand factor generation and release[69], tight junction formation and vessel permeability[71], as well as vascularization of cardiac tissues[74].

D. Disease Modeling

With advancements made in tissue engineering, 3D fabrication, and directed differentiation, interest has developed to not only regenerate healthy tissue, but also model pathologic states to better understand mechanism of disease[75]. By building *de novo* tissues in a controlled and complete engineered fashion, researchers are allotted greater complexity as compared with 2D cell culture while simultaneously are granted greater control of both cell type and system design as compared with animal models. One can add or remove individual cell types, alter matrix properties and can change structure on demand to determine those factors most pertinent to pathoetiology. These controls and ability to recreate human tissues are even more critical in diseases like malaria which are complex, specific to human infection, and pose an immediate threat to global health. In these final sections, I will outline pertinent research conducted to understand the pathogenesis of malaria and the need for a new model of disease.

1. Malaria

In 2016, 214 million cases of malaria infections were recorded, resulting in approximately 445,000 deaths. Of these deaths 91% of all cases occurred in sub-Saharan Africa and nearly 66% were in children under the age of five[76]. While the introduction of artemisinin combination therapies has been exceptionally effective in treating infections[77], in the past two years, concerns have been raised as new artesunate and piperaquine-resistant strains of Plasmodium falciparum, have emerged in the Greater Mekong subregions of South East Asia[78–80]. Epidemiological studies suggest that these strains are outcompeting other variants and becoming dominant throughout the region[81]. Regional experts fear that without alternative

treatments or a greater understanding of disease[82], a multi-drug resistant malaria strain may result in a repeat of the chloroquine disaster of the 1980s, which claimed millions of lives[83].

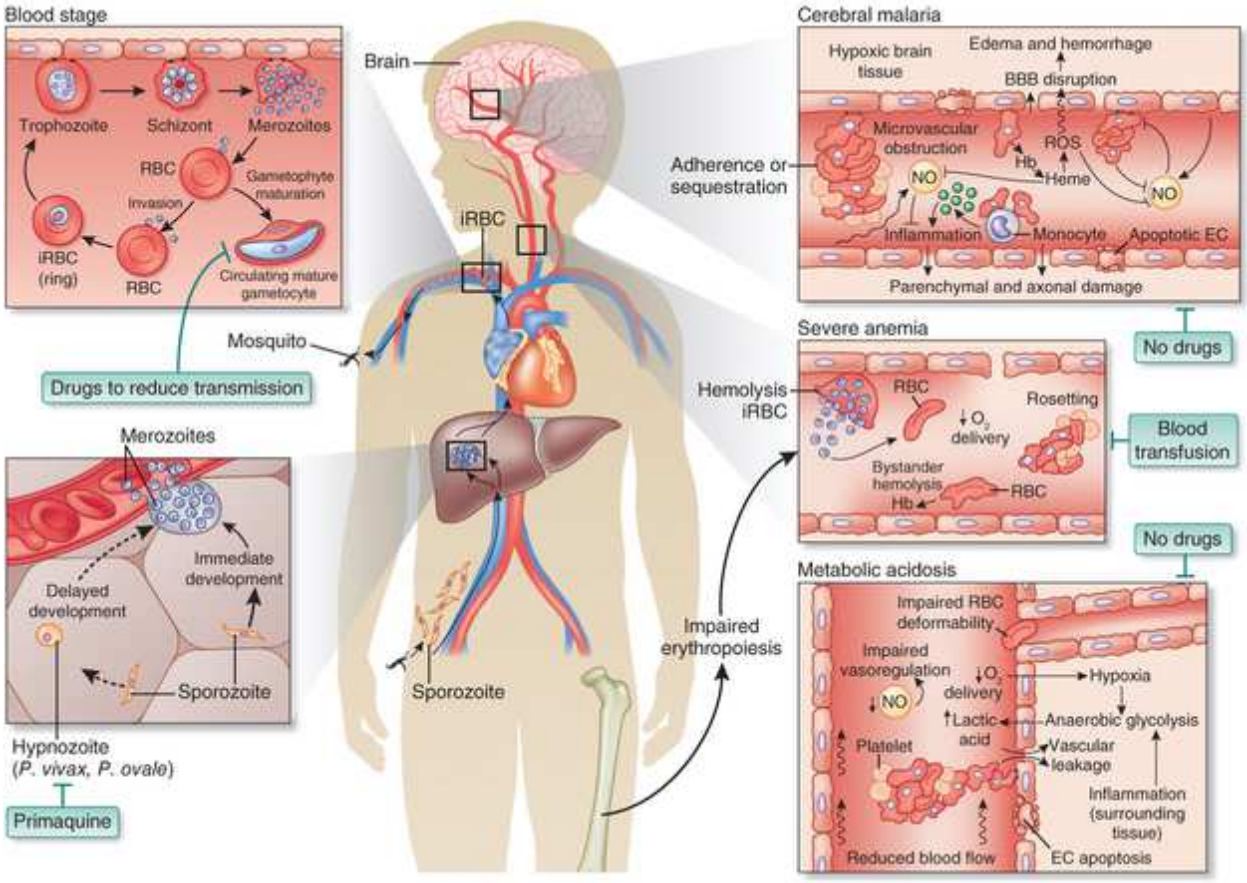

Figure 2-8: Pathogenesis of severe malaria in children

The parasitic life cycle of malaria involves two hosts: the vector, a malaria-infected female *Anopheles* mosquito, and the human. During a mosquito's blood meal, sporozoites are injected into the human host vasculature, travel to the liver and infect host hepatocytes. There they mature into schizonts which rupture and release merozoites which infect normal erythrocytes. Within IRBCs the parasites undergo asexual multiplication (erythrocytic schizogony), mature into ring stage trophozoites, to schizonts, and then rupture to release new merozoites to begin the erythrocytic cycle again. Patients can progress to severe malaria as the disease begins to effect specific organ systems as a result of sequestration, vaso-occlusion, or severe anemia. Figure adapted from Miller et al.[84].

Concerns surround the potential spread of these resistant strains from South East Asia to Sub-Saharan Africa, where malaria is both endemic and a significant cause of death[85]. As physical exam findings are non-specific (e.g., fever, night sweats, chills, muscle aches, vomiting) and because as many as one-third of patients can remain asymptomatic, too often victims can go untreated and progress to stages of severe disease (**Figure 2-8**). Those suspected to have developed severe malaria demonstrate heightened confusion, coma, focal neurologic signs, severe anemia, respiratory distress, and an increased parasite biomass or parasitemia > 5%, and can progress to death[86].

a) Sequestration of Infected Red Blood Cells

A key process in the etiology of severe malaria, and a potential target for treatment, is the sequestration of infected red blood cells (IRBC) to the endothelium of the host microvasculature (**Figure 2-8**)[87,88]. First observed over a century ago by Italian pathologists Bignami and Marchiafava, sequestration has long been thought to be essential to development of symptoms and disease[89]. During the mature blood stage of infection, parasites dramatically alter both the biophysical and biomolecular structure of the host cell[90], allowing IRBCs to exit circulation, accumulate in blood vessels, and avoid splenic filtration[91]. While sequestration can be observed throughout the vascular network, accumulation is largely focused in the capillary and post-capillary venule[92]. Several key proteins and modifications are believed to be paramount to IRBC sequestration and parasite survival.

b) Knob Associated Histidine Rich Protein

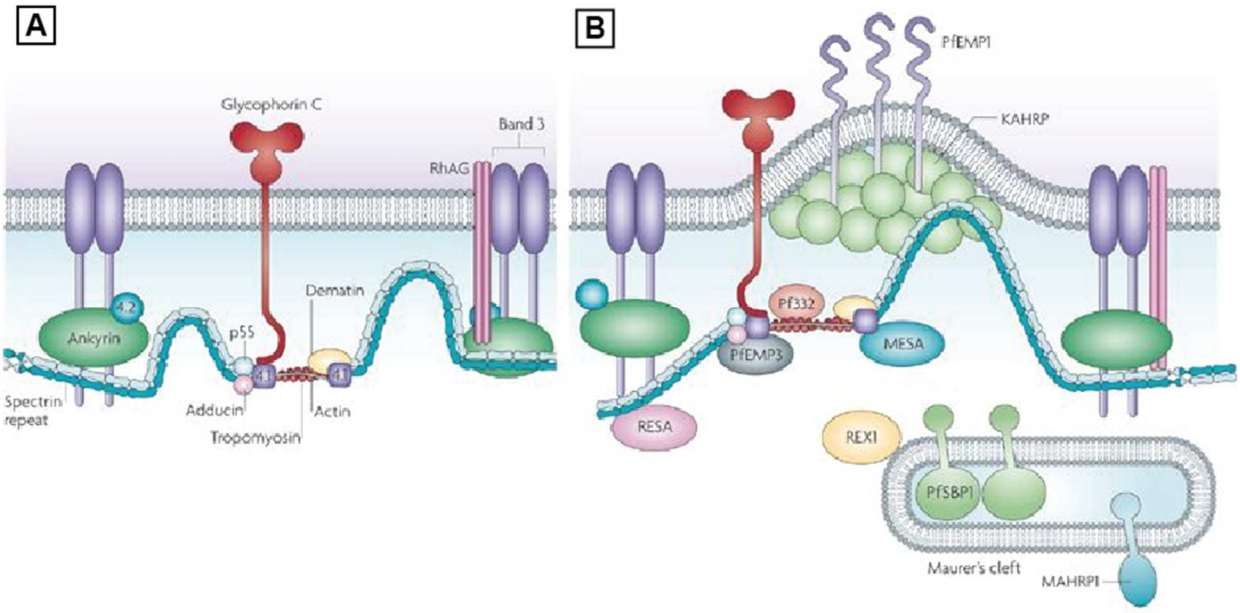

Figure 2-9: Membrane-associated modifications in uninfected and *Plasmodium falciparum*-infected red blood cells

a) Uninfected RBCs are constructed with hinged spectrin heterodimers that can expand and change shape upon deformation. At their tail junctions they complex with actin, are stabilized by protein 4.1R and are tethered to the cell membrane by ankyrin, protein 4.1R, p55 and glycophorin C. b) In mature-stage parasitized IRBCs, knob-associated His-rich protein (KAHRP) self-assembles into conical structures which bind spectrin, Pf332, mature-parasite-infected erythrocyte surface antigen (MESA), and Plasmodium falciparum erythrocyte membrane protein 3 (PfEMP3) stiffening the IRBC as compared with the normal RBC. The cytoadherent PfEMP1 interacts with and is concentrated at knob-like protrusions, bound by its cytoplasmic portion to KAHRP. Figure adapted from Maier et al.[90].

Perhaps the most obvious physical alteration of RBC shape and size is the loss of the hallmark biconcave shape and the development of electron dense knob-like protrusions[93]. These ~100 nm diameter conical structures appear approximately 16 hours after infection and result from the deposition and self-assembly of knob associated histidine rich protein (KAHRP) on the cytoplasmic region of the host RBC membrane (**Figure 2-9**). KAHRP has been shown to bind both host spectrin and ankyrin, significantly reducing RBC deformability and increasing stiffness

through a combination of membrane stiffening and strain hardening[94]. Computational modeling and microfluidic flow experiments have suggested that mechanical stiffening through KAHRP expression may lead to occlusion of small capillaries, enhance IRBC sequestration, and alter blood hemodynamics.

c) Cytoadherence

Focused at these knob-like protrusions and thought to be the main protein responsible for cytoadhesion of IRBCs is the Plasmodium falciparum Endothelial Membrane Protein 1 (PfEMP1) family[95]. Structurally, this family of proteins consist of three domains: a cytoplasmic region (acidic terminal segment) which binds KAHRP, and two variable extracellular host-binding domains consisting of a Duffy-binding-like region (DBL) and a Cysteine rich interdomain region (CIDR)[96]. These proteins are encoded by *var* genes found in the parasite genome and demonstrate significant polymorphic variation[97]. Believed to be a consequence of evolutionary pressure and a method of immune evasion, each genome contains roughly 60 *var* genes from which sub-variants of PfEMP1 are expressed in a mutually exclusive manner. Subvariants are grouped by both chromosome location as well as their DBL-CIDR head structure. DBL-CIDR combinations are not expressed randomly but instead organized in sequences known as domain cassettes (DC)[98]. Each DC is unique however most have been recognized to bind specific host endothelial receptors including Endothelial Protein C Receptor (EPCR), CD36, chondroitin sulfate, P-selectin, and ICAM-1 (Intercellular Adhesion Molecule 1) among others (**Figure 2-10**)[99].

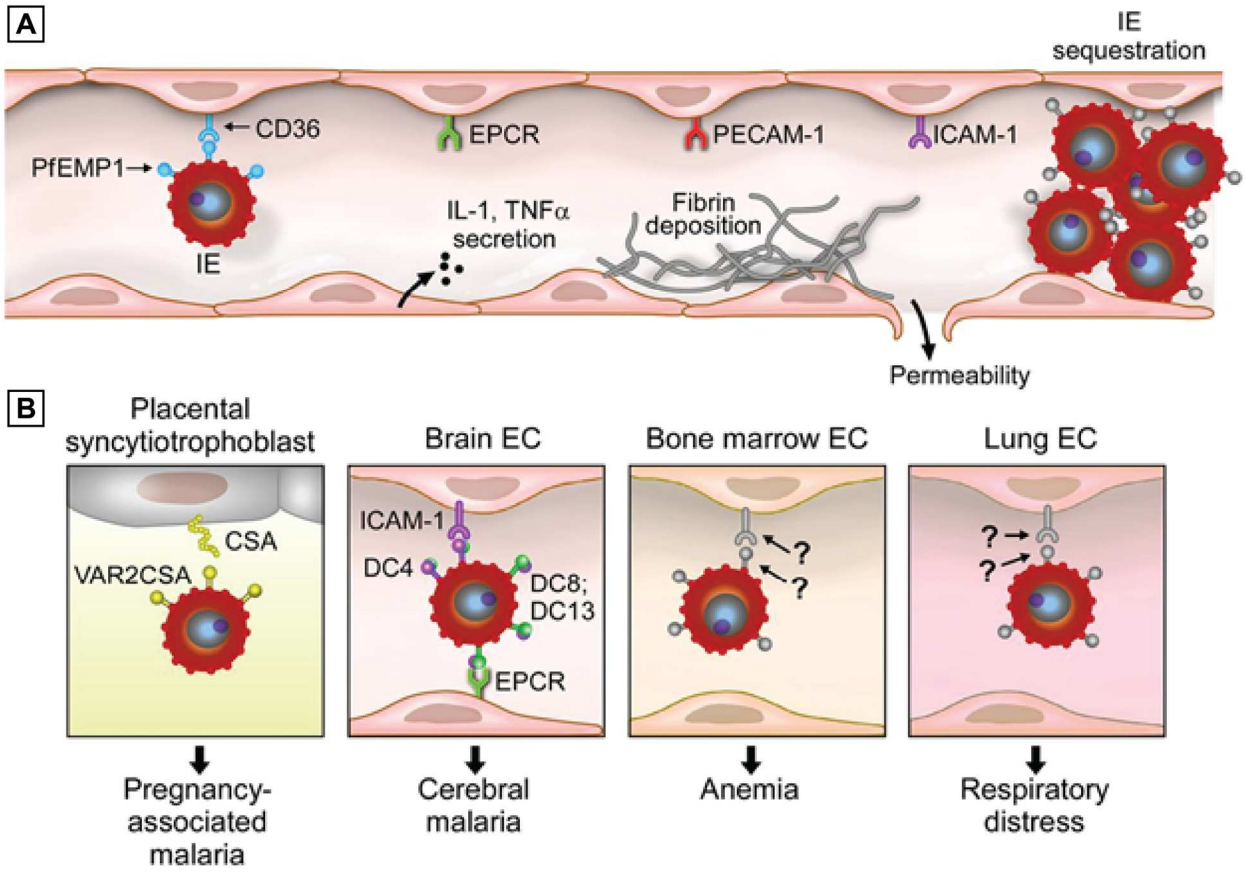

Figure 2-10: Cytoadhesion through PfEMP1 mediates microvascular sequestration of IRBCs

To avoid splenic filtration, parasites induce the expression of PfEMP1 molecules to adhere to the host vasculature and increase circulation time. Clonal expression of PfEMP1 results in subvariants of parasites that bind specific receptors and demonstrate organ-specific sequestration. A) PfEMP1 proteins are organized by the DBL and CIDR head structures called domain cassettes that bind particular endothelial receptors. DC8 and DC13 bind EPCR, DC5 binds PECAM-1, and DC4 binds ICAM-1. B) Organ specific binding as a consequence of PfEMP1 expression has been observed in the placenta, brain, bone marrow, and lung. Figure adapted from Aird et al.[100].

As demonstrated by our collaborators in the Smith Lab (Center for Infectious Disease Research, Seattle, Washington), particular subvariants can convey more dangerous phenotypes as they demonstrate a propensity to bind and sequester in specific organ systems[101]. Of those variants, those that express domain cassettes 8 and 13 are particularly dangerous as they mediate

cerebral binding, are associated with cerebral malaria and severe disease[98], and are strong binders to brain, heart, lung, and bone marrow endothelial cells[102]. DC8 and 13 PfEMP1s are specific for EPCR, an endothelial protein known to regulate blood coagulation, endothelial activation, and endothelial barrier properties[103]. While the exact mechanism by which EPCR-mediated sequestration gives rise to cerebral malaria is being investigated, convincing population studies suggest that EPCR-specific binding plays a critical role.

d) Current Models of Disease

While there are five species of the Plasmodium genus that cause disease in humans, *Plasmodium falciparum* is responsible for roughly 50% of all malaria cases, causes the most dangerous form of malaria, and is specific to human infection[104]. Due to its human specificity and its unique disease-causing characteristics, not observed in other species, *P. falciparum* is very difficult to study *in vivo*. As no animal model of *P. falciparum* infection exists, inferences are instead largely drawn from experiments involving analogous parasite species which infect non-human organisms[105].

A large body of work is conducted using *Plasmodium berghei*, a relative of *P. falciparum* which is easily genetically modified, has a very similar life-cycle, and readily infects certain rodents[106]. Despite its wide use in the development of anti-malaria drugs and to understand the infection process, debates brew over its applicability to study severe disease as the mouse model fails to replicate the pathophysiology of severe malaria in humans. The most prominent shortcomings are *P. berghei*'s lack of a cytoadhesive analog to PfEMP1, low degree of organ sequestration, and dissimilar binding patterns to those observed in human disease. While interest exists to genetically engineering a "falciparumised" *P. berghei*, complications surround the

introduction and expression of a PfEMP1 protein in *P. berghei* as well as generation of a corresponding transgenic mouse that expresses human endothelial receptors and does not reject human RBCs[107,108]. Consequently, little progress has been made to successfully create a humanized rodent model of disease.

Most recently, cautious interest has developed in generating non-human primate models as these species reflect human pathophysiology more closely than their murine counterparts[109]. Several parasites have been proposed in the Japanese and rhesus macaque models including: *P. coatneyi* and *P. knowlesi*[110]. These two strains, unlike *P. berghei*, express var-like genes, demonstrate antigenic variation and adhesion properties[111]. However, it is still unclear whether either are useful models for human cerebral malaria as neither adhesion of IRBCs to cerebral vessels nor clinical signs reflective of human cerebral malaria have been indicated.

As existing *in vivo* models both lack key aspects of pathophysiology and as they only allow for limited control of the biological, chemical, and physical parameters which govern IRBC sequestration, others have turned to mathematical modeling, microfluidics, and human cellular monolayer culture to study parasite infection. In these systems, it has been possible to identify PfEMP1 subvariants and their binding partners[99], examine the mechanical changes which occur upon parasite infection of host erythrocytes, determine organ specific cytoadhesive properties[102], model IRBC margination[112] and assess IRBC capacity to deform through small microfluidic chambers[113,114]. Nevertheless, despite their utility, polydimethylsiloxane (PDMS), glass, and parallel-plate flow chambers containing endothelial cell monolayers do not accurately recapitulate vessel geometry, often fail to capture the cellular contributions to cytoadhesion, do not mimic the vascular matrix and have been unable to recapitulate the small vessel-diameter endothelialized vessels wherein IRBC sequestration is focused. With few alternative options, an

in vitro human model of malaria infection and disease could prove paramount to understanding and combating *P. falciparum* infection.

E. Closing

The field of tissue engineering and its applications are vast, encompassing both the regeneration of replacement tissues as well as disease modeling. While significant advancements in polymer design, stem cell biology, and new fabrication techniques have allotted us greater control of cells and tissues, nontrivial challenges lie ahead. 3D tissue structure and maturation, vascularization, and pathophysiological modeling remain significant tasks yet to be explored. In these challenges lie opportunities to develop new tools to change how we study biology and create solutions to remedy medical need. In the following chapters, work here will attempt to address these issues through the invention of new materials and new approaches to constructing 3D tissues and organs.

CHAPTER 3: THESIS OBJECTIVE AND SPECIFIC AIMS

This thesis aims to utilize light-mediated chemistries and novel hydrogel platforms to generate 3D tissues within synthetic materials, construct 4D vasculature, and generate the world's first capillary networks to study pathological blood-endothelial interactions. Toward these goals, my work is organized into a preliminary data section followed by two main aims. Chapter 4 motivates work by demonstrating the capacity to generate 3D tissues in chemically defined hydrogels. This early work defines the material and biological criteria which facilitate the culture of stem cells and differentiated tissues in synthetic PEG hydrogels. As these tissues require delivery of oxygen and nutrients, Chapter 5 then describes Aim 1, a novel photodegradation based technique to generate 3D blood vasculature with complete spatiotemporal control. Finally, to expand our fabrication techniques to non-degradable materials and to understand the interactions between blood and vasculature, Chapter VI describes Aim 2, the development of a photoablative technique in which femtosecond-pulsed lasers are used to create perfusable capillary networks. These capillaries are then used to study not only physiological hemodynamics but also determine the factors responsible for pathologic IRBC sequestration observed in the setting of severe malarial.

CHAPTER 4: MOTIVATION AND PRELIMINARY RESULTS

A. Introduction

Human development and tissue regeneration are delicate choreographies involving a myriad of cells and bioactive molecules simultaneously interacting in a precisely controlled manner with respect to both space and time[115]. Despite their complexity, these events occur with exquisite reproducibility to give rise to conserved anatomical organization and organ architecture. While a complete model of human development *in vitro* raises both ethical and technical concerns, human embryonic (hESC) and induced pluripotent stem cells (hiPSC) offer insight into these developmental processes and a means to generate replacement tissues. Yet, while hPSCs can give rise to all three germ layers *in vitro*, nearly all culture and subsequent differentiation of hESCs and hiPSCs are confined to 2D platforms which cannot feasibly recapitulate the inherent 3D structure which emerges during embryogenesis[116]. Furthermore, despite the potential of pluripotent stem cells in regenerative medicine, attempts to culture and maintain their stemness in 3D model tissues have proven uniformly unsuccessful. Those widely used natural-based biomaterials (e.g., Matrigel, collagen, fibrin) provide an environment that supports mature cell function, however batch-to-batch variability and ill-defined biochemical signals including growth factors left over from material isolation promote uncontrolled differentiation and maturation into unwanted cell types and at undesired times[16].

Recapitulating the dynamic and heterogeneous aspects of the stem cell niche has proven to be difficult as commonly employed matrix materials lack physiochemical tunability. Unlike culture platforms derived from natural components (e.g., Matrigel), synthetic biomaterials provide a “blank slate” by which user-defined biochemical functionality can be specified.

Chemically defined biodegradable PEG-based hydrogels, developed and advanced by the DeForest lab, however are similarly biocompatible while uniquely permit photopatterned control of network mechanics, biodegradability, and biochemical functionality. Inspired by and in cooperation with our collaborators from the Murry and Freedman labs (University of Washington), we sought to reconstruct cardiac tissues and kidney organoids in click-based synthetic PEG hydrogels to better understand the role of ECM and 3D cell culture on pluripotent stem cell differentiation and development. Findings here served as a baseline for future cellular and biological work conducted using our synthetic PEG-based hydrogels.

B. Generation of Engineered Cardiac Tissues in Synthetic Matrices

We first attempted to build upon platforms and technologies previous explored by ourselves and collaborators by constructing cardiac tissues within synthetic PEG hydrogels. As synthetic hydrogels permit chemical, physical, and mechanical tuneability, we sought to determine the engineering and design criteria to sustain CM viability and optimize function.

Base hydrogels were generated through the copper-free addition of a strained alkyne to a azide via SPAAC chemistry, joining a four-arm poly(ethylene glycol) tetrabicyclononyne (PEG-tetra BCN, 20kDa)[19] and an MMP-cleavable diazide peptide: N_3-RGPQG↓IWGQGRK(N_3)[117]. Previous work by our lab has established that unlike other hydrogel platforms, our SPAAC-based networks form within minutes, are completely cytocompatible, and allow for stoichiometric control of crosslinking density and addition of stimuli responsive elements. Extensive, rheological studies have previously been explored, where notably by altering either the molecular weight of the PEG crosslinker or modulating the azide: cyclooctyne ratio, a wide range of initial mechanical moduli is achievable (G' ~ 1-10 kPa). As mature cardiac tissue is

estimated to have mechanical modulus of roughly 10 kPa[118], our hydrogel matrices mimic the microenvironment of native tissue[117].

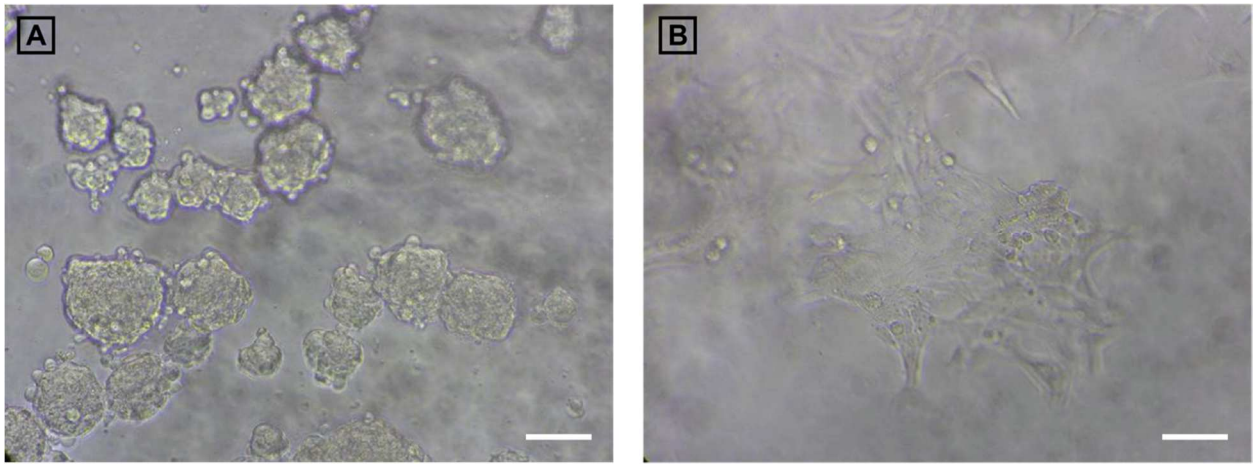

Figure 4-1: RGDS pendant peptide permits stromal cell attachment and spreading

hS27a Stromal Cells were seeded on PEG-BCN/Diazide MMP-cleavable-photodegradable peptide-based hydrogels with A) 0 or B) 1.5mM RGDS-azide pendant ligands. Cells were cultured for 1d and imaged using standard bright-field microscopy. (Scale bar = 20 μm)

As this base hydrogel does not promote cell adhesion, migration, or survival, an azide-functionalized pendant peptide: N_3-RGDS-NH_2 was synthesized and incorporated to support cell attachment[119]. RGDS is a well-established peptide recognized by cell integrin receptors, derived from the ECM protein fibronectin, and widely used in tissue engineering to encourage cell attachment[120]. To confirm RGDS function, hS27a stromal cells were seeded on the surfaces of SPAAC hydrogels conjugated with either 0 or 1.5 mM RGDS. After 24 hours, cells cultured on the surfaces of RGDS-containing hydrogels demonstrated spindle-like cell morphology characteristic of 2D cell culture on tissue culture polystyrene indicating functional integrin binding motifs. (**Figure 4-1**)

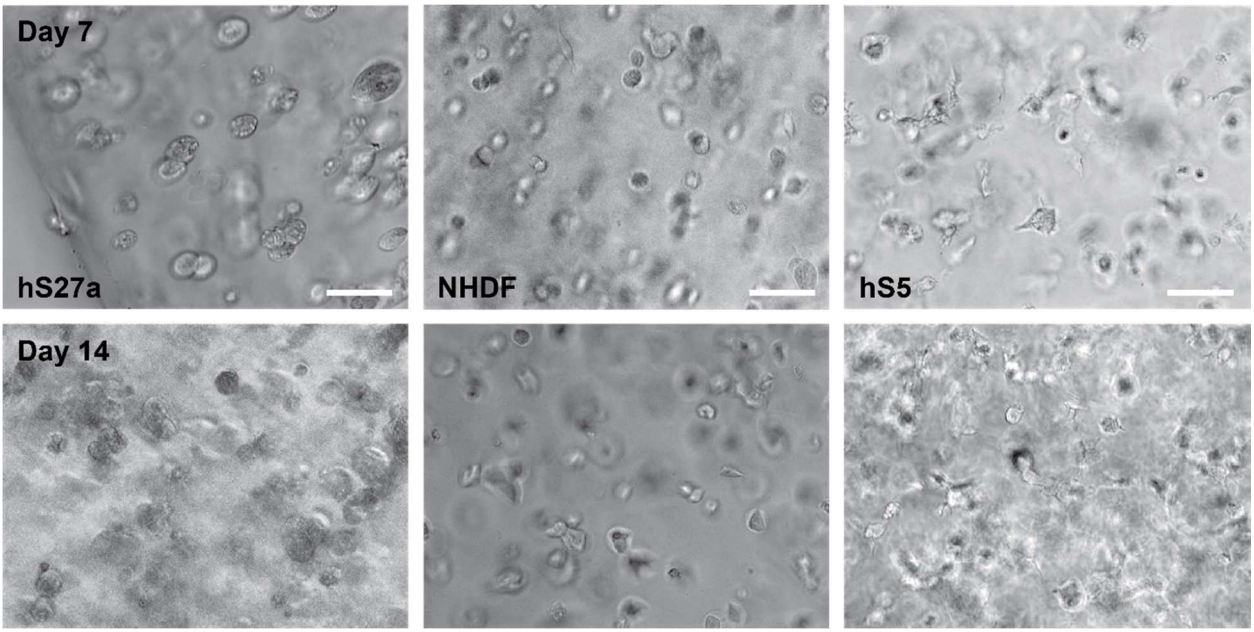

Figure 4-2: hS5, hS27a, and NHDF cells were cultured in SPAAC hydrogels cultured for 2 weeks

NHDF, hS27a, and hS5 cells were cultured in SPAAC hydrogels ($20x10^6$ cells/mL) containing MMP-cleavable crosslinkers and RGDS moieties to encourage cell attachment, proliferation and remodeling. Cultured in their respective medias, cells were observed in 3D culture for 2 weeks by phase contrast microscopy. (Scale bar = 30 μm)

After having confirmed our materials were bioactive in 2D, it was then critical to optimize both cellular and material components to allow for tissue compaction, remodeling, and cell survival in 3D. As it has been demonstrated that stromal cells promote survival and function of CM in 3D culture[74], it was imperative to identify a stromal cell line able to proliferate within and remodel our hydrogels. Normal human dermal fibroblasts (NHDF), and the bone marrow derived stromal cell lines: hS5 and hS27a were encapsulated within 10 wt% PEG hydrogels conjugated with 1.5mM RGDS peptides ($20x10^6$ cells/mL) and cultured for 2 weeks (**Figure 4-2**). While NHDF and hS27as did not show signs of spreading or remodeling, hS5 cells demonstrated cell protrusions as early as day 7 with an increasing number of spindle shaped cells

by day 14. As degradation of encapsulating matrix is required to allow for cell spreading, findings suggest hS5s are more readily able to degrade our synthetic hydrogels. This agrees with the relative MMP expression and remodeling capacity of hS5 cells as compared with hS27a observed by our collaborators in the Zheng and Torok-Storb labs (Fred Hutchinson Cancer Research Center, data not published).

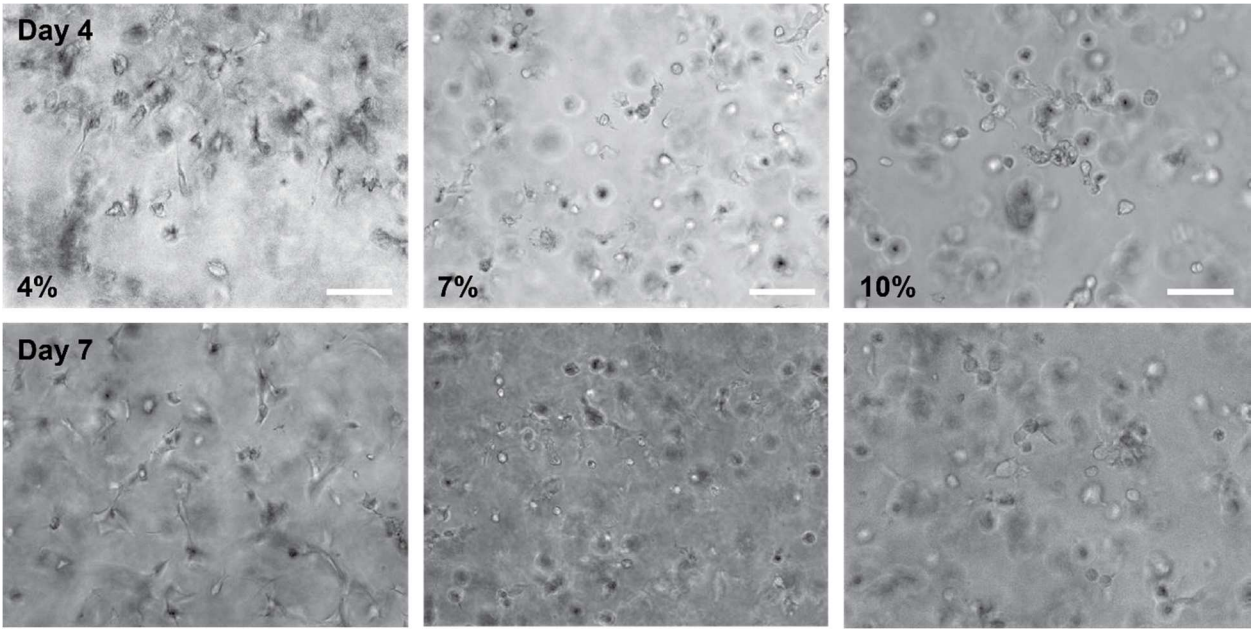

Figure 4-3: hS5 stromal cells encapsulated in 4-10 wt% PEG-BCN/Diazide MMP-cleavable-photodegradable peptide hydrogels containing RGDS

hS5 cells were cultured in SPAAC hydrogels ($20x10^6$ cells/mL) containing MMP-cleavable crosslinkers and RGDS moieties with varying wt% to determine the effect of crosslinking density and mechanical modulus on the capacity of stromal cells to remodel their matrix. Cells were observed in 3D culture 1 week by phase contrast microscopy. (Scale bar = 30 μm)

Matrix stiffness was also considered to further encourage cell remodeling. To modulate stiffness and crosslinking density simultaneously, hS5 cells were cultured within PEG hydrogels of varying weight percentage (4, 7, or 10 wt%). While spreading was observed in all three

conditions, 4% hydrogels proved unstable for long-term culture and began to lose structural integrity by day 7. Meanwhile, cells cultured in 10% hydrogels exhibited very little migration and remodeling. While spreading was observed, most cells remained spherical throughout culture. 7% hydrogels however maintained shape with minimal swelling. Furthermore, cells cultured in 7% hydrogels actively remodeled the matrix and demonstrated robust spreading and proliferation (**Figure 4-3**).

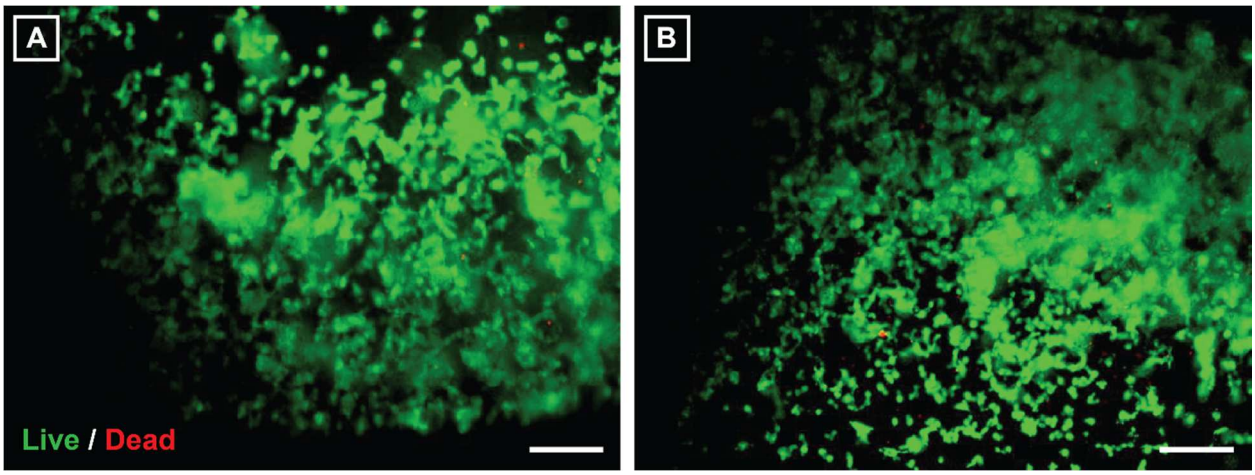

Figure 4-4: Live/Dead Staining of CM encapsulated in PEG hydrogels

1:10 hS5 cells to CM were encapsulated at either A) 20 x 10^6 or B) 40 x 10^6 in PEG hydrogels by mixing dispersed cell pellets in PEG-tetra BCN then mixed with peptide crosslinker just prior to being delivered to PDMS molds. After allowed to polymerize for 1h, hydrogels were placed in 6-well tissue culture dishes and submerged in growth media. CM cultures were stained with Live/Dead stain to determine cell viability 24 hours after encapsulation. (Scale bar = 250 µm)

To construct cardiac tissues, cardiomyocytes were differentiated from RUES-2 hESCs using an established directed differentiation protocol[121,122] at a high purity (94.7% $cTnT^+$), mixed with hS5 cells at a 10:1 ratio (cardiomyocyte: stromal cell) and encapsulated within RGDS containing PEG hydrogels. Cocultures within PEG hydrogels demonstrated little to no observable cell death by LIVE/DEAD staining (Invitrogen) after 24 hours (**Figure 4-4**). To

encourage internal mechanical strain and to promote CM maturation[123], CM/hS5-laden hydrogels were cast in two-post molds **(Figure 4-5)** and successfully cultured for seven weeks. Spontaneous beating was observed by day 4 and compaction and remodeling of the PEG hydrogel progressed over the 7-week period resulting in synchronous tissue-like beating (**Figure 4-6**). To our knowledge, this is one of the first examples of cardiac tissue formation in a PEG hydrogel and demonstrates the capacity for our system to support the viability and function of CM for long term culture.

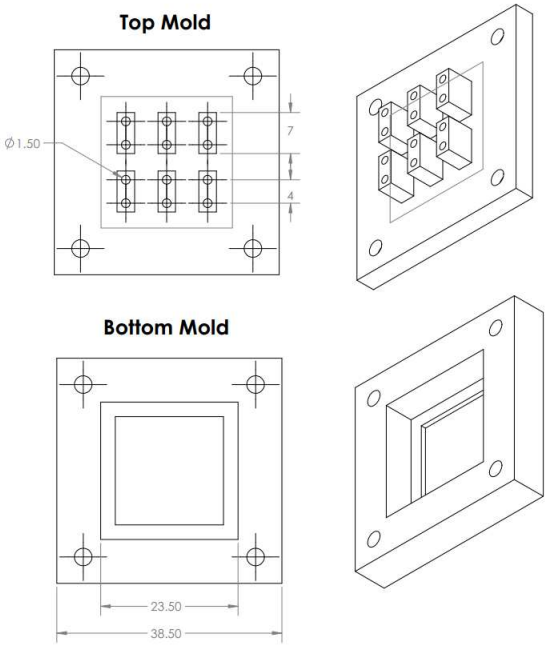

Figure 4-5: 3D printed mold for a dual post PDMS cardiomyocyte culture platform

PDMS post molds were fabricated in 3D printed PLA molds created using CAD design software. PDMS molds were sterilized in ethanol and then used to cast PEG hydrogels containing CM and stromal cells.

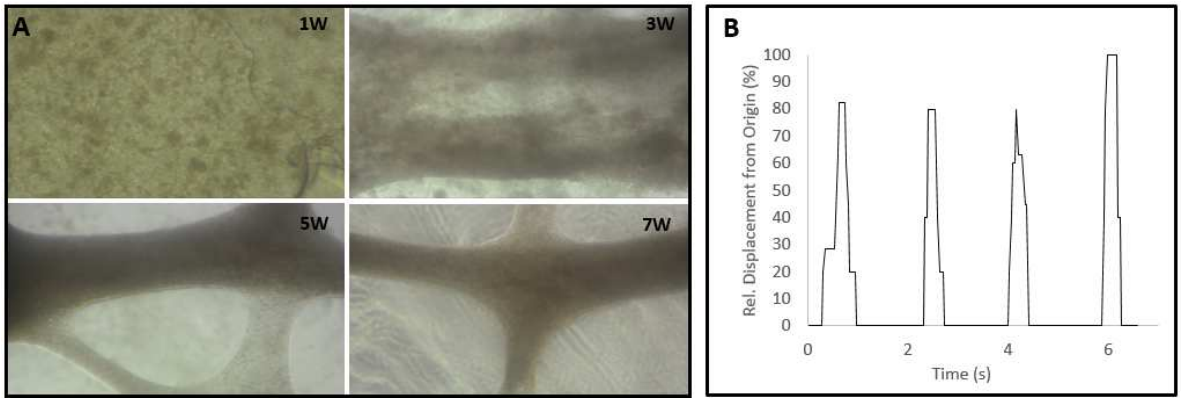

Figure 4-6: Long term culture of CM in PEG hydrogels

A) hES derived CM were grown and cultured in PEG hydrogels cast within a 2-post PDMS mold and imaged using light microscopy for 7 weeks. (frame~ 3 mm) B) CMs were observed to spontaneously contract in 3D after 5 days of culture. Position was analyzed by manual position tracking (ImageJ) of captured video of cell contraction.

C. Directed Differentiation of hPSCs in Defined 3D Chemical Microenvironments

In addition to assembling tissues from differentiated cells, we also attempted to direct differentiation of hPSCs toward renal and cardiac cell types within chemically defined PEG hydrogels. Work here was not simply motivated to construct functional, but also to better understand the factors that govern differentiation in 3D, the role of ECM on tissue development and our ability to recreate those events in synthetic matrices.

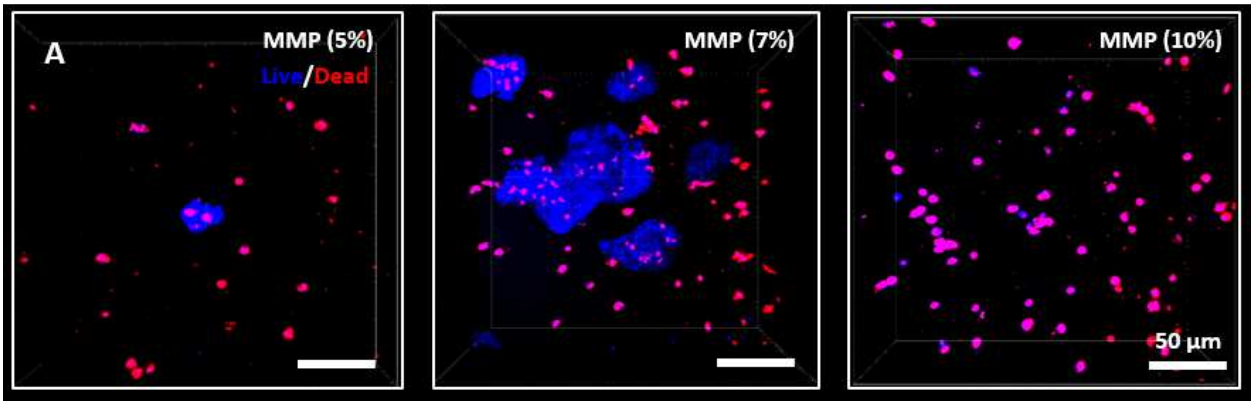

Figure 4-7: Optimization of hydrogel stiffness for hPSC culture

WTC11 hiPSCs were encapsulated within PEG hydrogels to determine optimal hydrogel stiffness during short term culture in 3D. A) As a proxy for stiffness and crosslinking density, PEG hydrogels of varying weight percent were used to culture WTC11 cells in 3D for 7 days. Cell colonies were imaged using a LIVE/DEAD staining kit (Blue = Live, Red = Dead).

The minimum requirements for a successful hPSC culture platform necessitate that encapsulated stem cells retain their pluripotency until differentiation is initiated. To this end, preliminary data of both hESC (H9) and hiPSCs (WTC11) cell culture in click-based PEG-peptide hydrogels were promising. First, matrix stiffness was considered. By altering weight percentage, dramatic differences in cell viability were observed. Here, hydrogel weight percentages of 5, 7, and 10% were considered. Either H9s or WTC11s were encapsulated (1 x

10^6 cells/ mL) within hydrogels generated from 20 kDa four-arm PEG-tetraBCN[19,124–126] and a diazide MMP-cleavable peptide crosslinker, N_3-RGPQG↓IWGQGRK(N_3). No integrin binding moieties were added so as to minimize effects of matrix on stem cell differentiation. Constructs were cultured in mTeSR media supplemented with 5 μM Rock inhibitor for 2 days followed by culture in mTeSR media and subsequently assayed for cell viability using a LIVE/DEAD staining kit (Invitrogen). Both H9 (Data not shown) and WTC11 cells encapsulated in either 5 and 10 wt% hydrogels demonstrated poor viability, with few viable colonies identified in the 5 wt% hydrogels and no viable cells in the stiffer matrices. Cells encapsulated within 7% hydrogels however demonstrated high degrees of viability (**Figure 4-7**). Findings indicate that there exists a critical microenvironment stiffness in which cells maintain the capacity to remodel their surroundings and remain functional.

In addition to survival, cells cultured in PEG hydrogels developed a unique cavitated spheroid morphology upon colony formation (**Figure 4-8A-C**). Visible by both brightfield as well as multiphoton imaging, colonies were dense at the periphery with hollow centers. Single or multiple cavities were recorded. These findings are promising as analogous 2D structures have been recognized by the Freedman group when either hiPSC or hESC are cultured within matrigel on tissue culture polystyrene. This cavitated spheroid stage is regarded as a critical window which must be achieved prior to kidney differentiation[55].

Subsequent immunofluorescent staining of cells after fixation also suggest that viable cells both proliferate within gels and sustain their stemness, as nearly all colonies were observed to be $Oct4^+$ (**Figure 4-8C**). Together this data indicates that culture of hPSCs within PEG hydrogels permits colony formation, maintains stemness, and allows for colony remodeling of their hydrogel matrix.

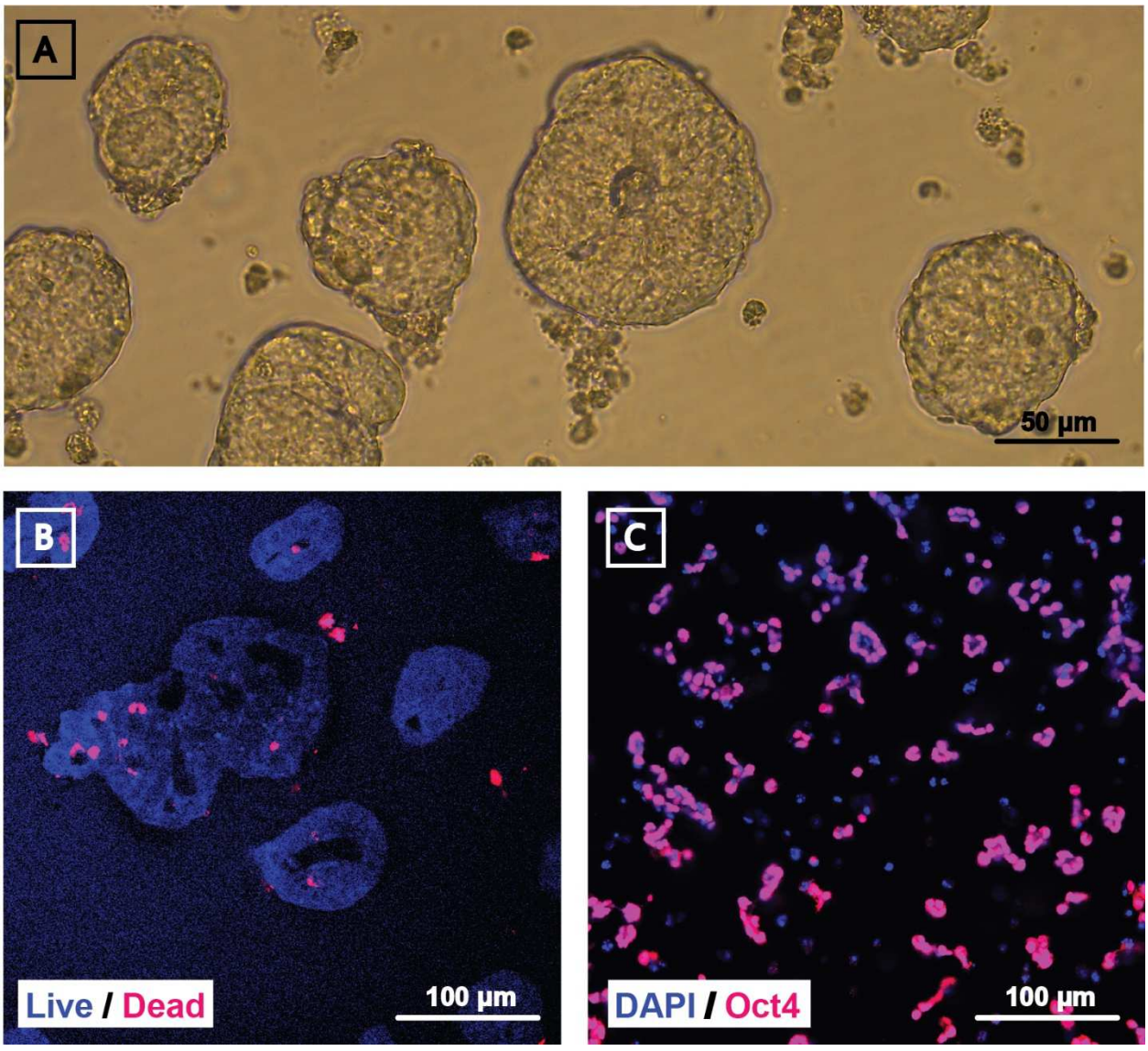

Figure 4-8: hPSC colonies cultured in PEG hydrogels demonstrate polarization and maintain pluripotency

A) Brightfield imaging and B) multiphoton imaging of H9 hESC colonies cultured in PEG hydrogels for 5 days reveals polarized hollow spheroid-like morphologies. C) Confocal imaging of hESC colonies on day 3 demonstrates most cells remain pluripotent (as determined by expression of Oct4).

Having generated a platform which not only supports hPSC culture but also stemness we then proceeded to determine an appropriate differentiation protocol to generate renal and cardiac

tissues. While coordinated actions of many signal transduction pathways occur during development and again iteratively throughout maturation, the canonical Wnt/β-catenin pathway is one of the best characterized and most critical pathways in early embryogenesis[127]. In particular, it is known that Wnt/β-catenin signaling is necessary for both the formation of the primitive streak and throughout gastrulation as it is regarded as the primary driver in mesodermal anterior-posterior axis patterning[128]. Our collaborators and others have utilized this knowledge to create mesodermal-derived cardiac and renal tissues from hPSCs by exclusively manipulating canonical Wnt signaling[51,52,55,62,129]. Robust protocols utilizing high concentrations of Wnt agonists yield kidney organoids complete with podocyte, proximal and distal tubule cell types while those utilizing biphasic low to moderate concentrations of Wnt agonists followed by Wnt inhibition yield cardiomyocyte populations with upward of 90% efficiency.

Utilizing these Wnt-exclusive differentiation protocols to direct hPSC differentiation toward cardiac and kidney lineages in PEG-peptide hydrogels showed great promise. Briefly, either hESCs and hiPSCs were encapsulated in 5 wt% MMP-degradable PEG hydrogels (at seeding densities of 0.5 – 1 million cells/mL), cultured for 2 days in 5 μM ROCK-inhibitor supplemented mTeSR, then treated using either a directed cardiac or kidney differentiation protocol[55,130]. After 4 weeks of culture, tissue morphologies suspected to be of kidney, cardiac, and potentially neuroectoderm origin were observed (**Figure 4-9**). Beating could be observed in all samples treated using the established cardiomyocyte differentiation protocol as early as day 5. Based only on bright-field analysis, cardiac-specific differentiation appeared significantly more efficient using hESCs as compared with hiPSCs.

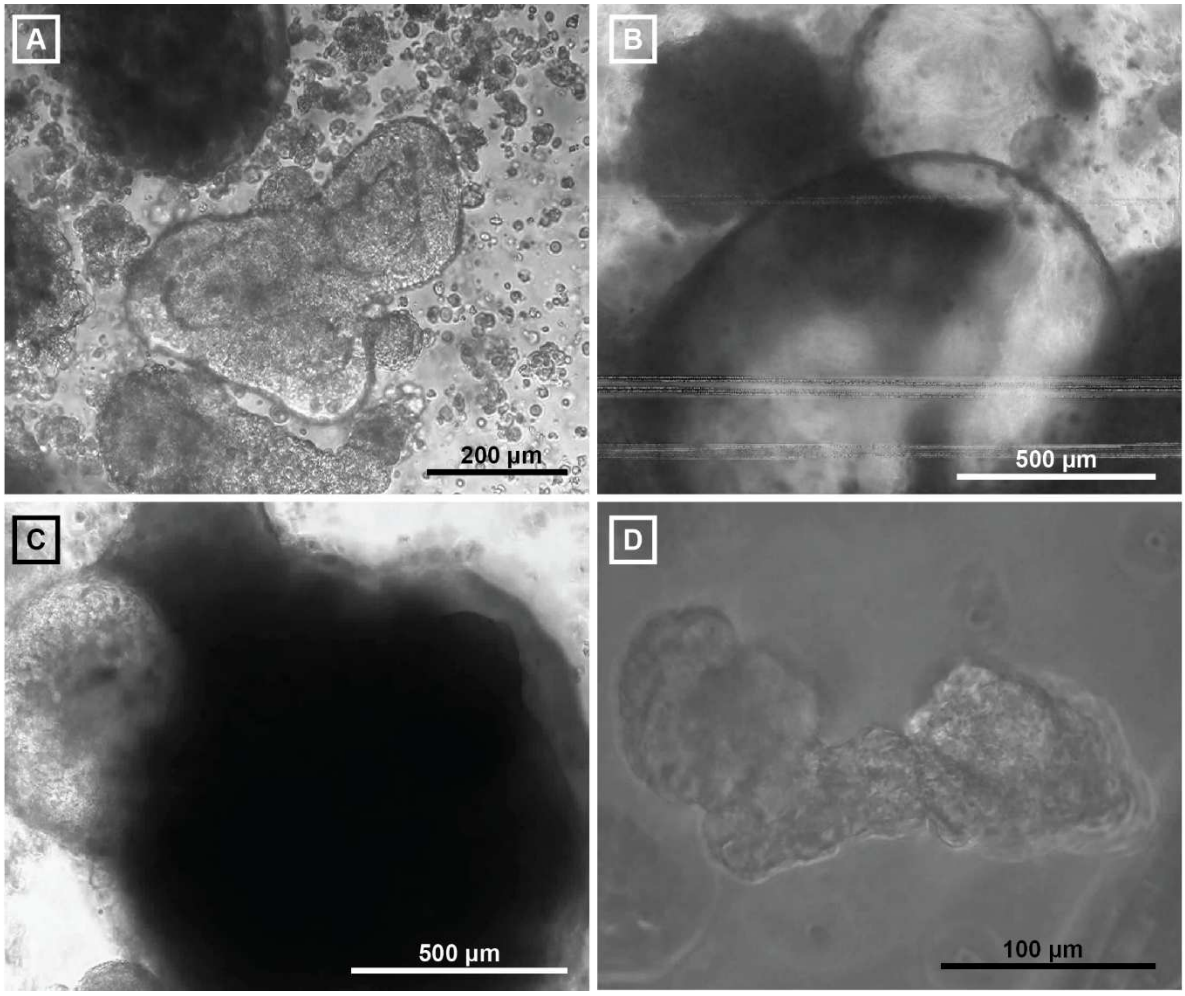

Figure 4-9: Directed differentiation within gels using small molecule Wnt agonists

Directed differentiation protocols were performed on hPSCs cultured in PEG hydrogels. Samples were either treated with A) Low Wnt activation (3 µM CHIR) for 2 days followed by Wnt inhibition (2 µM Wnt-C59), B) directed kidney differentiation: High Wnt activation (12 µM CHIR) for 2 days, or C-D) directed cardiac differentiation: moderate Wnt activation (6 µM) for two days followed by Wnt inactivation (2 µM Wnt-C59) for 2 days. Experiments A-C) utilized hESCs (H9) while Sample D) was performed using hiPSCs (WTC11).

D. Materials and Methods

1. Hydrogel Formation and Peptide Synthesis

Four-armed PEG-tetra BCN and peptides were generated as previously described[117]. Briefly, RGPQGIWGQGRK(Dde)-NH_2 peptides were generated by microwave-assisted Fmoc solid-phase peptide synthesis on Rink amide resin (0.5 mmol scale). Resin and peptide were then treated with hydrazine monohydrate (2 % in DMF) three times, each for ten minutes, to remove the Dde protecting group. N_3-COOH (0.517 g, 4.0 mmol, 4x) was activated with 1-[Bis(dimethylamino)methylene]-1H-1,2,3-triazolo[4,5-b] pyridinium 3-oxid hexafluorophosphate (1.502 g, 3.95 mmol, 3.95x) and DIEA (1.034 g, 8.0 mmol, 8x) in minimal DMF for 5 minutes. This solution was then used to treat the resin-bound peptide for 90 minutes to functionalize both the N-terminus and amino group of the terminal lysine with azides. The peptide was then deprotected and cleaved from the resin using TFA/triisopropylsilane diluted in H_2O (95:2.5:2.5) for 2 hours, precipitated in ice-cold diethyl ether, purified by HPLC, and confirmed by MALDI. RGDS peptides were formed similarly using the sequence N_3-RGDS purified by HPLC and identified by MALDI. Hydrogels were formed by pre-reacting RGDS with PEG-tetra BCN for 1h followed by dilution with PBS and gelation by SPAAC with diazide peptide crosslinker in the desired mold for 1 hour.

2. Stromal Cell Culture and Encapsulation

Normal human dermal fibroblasts (ATCC, VA, USA) were cultured in Fibroblast Basal Medium supplemented with a Fibroblast Growth Kit-Low Serum Supplement (ATCC). hS5 and hS27a stromal cells (Torok-Storb Lab, Fred Hutchinson Cancer Research Center and Zheng Labs, University of Washington) were cultured in RPMI 1640 supplemented with 10% Fetal

Bovine Serum (Corning) and 1% penicillin/streptomycin. Cells were cultured using standard cell culture techniques. Encapsulation was performed by first mixing cell suspensions with the PEG-tetra BCN prepolymer solution, gentle mixing to ensure homogenous distribution of cells, addition of the peptide crosslinker and then gentle mixing again. Polymerizing prepolymer solutions were then pipetted into tissue culture polystyrene well plates.

3. Confirmation of RGDS Function in 2D Cell Culture

To determine the ability of synthesized N_3-RGDS pendant peptides to encourage cell spreading, hS27a stromal cells were seeded on the surfaces of SPAAC hydrogels conjugated with 1.5 mM RGDS were generated at the bottom of 96 well plates. 2D cultures were observed for 24 hours and compared with SPAAC hydrogels containing no RGDS. Cells cultured on the surfaces of RGDS containing hydrogels demonstrated spindle-like cell morphology characteristic of 2D cell culture on tissue culture polystyrene indicating functional RGDS.

4. Encapsulation of Stromal Cells

NHDF, hS27a, and hS5 cells were cultured in SPAAC hydrogels (20 x 10^6 cells/mL) containing MMP cleavable crosslinkers and RGDS moieties to encourage cell attachment, proliferation and remodeling. Cultured in their respective medias, cells were observed in 3D culture for 2 weeks by phase contrast microscopy. To evaluate contribution of matrix mechanics on cell viability and function, hS5 cells were cultured in SPAAC hydrogels (20 x 10^6 cells/mL) containing MMP-cleavable crosslinkers and RGDS moieties with either 4, 7, or 10 wt% to determine the effect of crosslinking density and mechanical modulus on the capacity of stromal

cells to remodel their matrix. Cells were observed after one week in 3D culture by phase contrast microscopy.

5. *LIVE/DEAD Staining and Immunostaining*

To determine viability and to observe stromal and cardiomyocyte populations after encapsulation, living constructs were washed once with PBS and then stained with calcein-ethidium homodimer, using a LIVE/DEAD assay kit (Invitrogen) at 37□ for 30 min. Stained samples were observed by fluorescent microscopy.

Immunostaining of hydrogel constructs was performed using standard protocols. Briefly, constructs were treated with 3.7% formaldehyde for 20 minutes and washed with PBS for three 5-minute intervals. Hydrogels were then submerged in blocking solution containing 2% bovine serum albumin and 0.1% Triton X-100 (Invitrogen) before immunostaining. Primary antibodies were diluted in blocking solution and incubated overnight at 4□. Samples were then washed with PBS three times for 20 minutes each. Solutions were changed into a secondary antibody solution diluted in blocking buffer for 1 hour, washed three times and imaged using a multiphoton microscope (Olympus FV1000 MPE BX61 Microscope). Image analysis was performed using either Image J or IMARIS imaging software.

6. *Directed Differentiation of Cardiomyocytes for the Construction of Cardiac Tissues*

Spontaneously beating cardiomyocytes were generated from RUES2 hESCs (Rockefeller University, NIH 0013) using an established differentiation protocol[131]. Briefly, RUES2s were maintained as undifferentiated colonies using feeder-free mTeSR-1 media supplemented with mTeSR Supplement (STEMCELL Technologies) on Matrigel-coated tissue culture well plates.

One day prior to colony confluence, cell monolayers were treated with 1 μM CHIR 99021 in mTeSR. Upon reaching confluence, induction was started using 100ng/mL rh-Activin A (R&D) diluted in 1x Matrigel for 18 hours. Media was then changed to fresh mTeSR supplemented with 5ng/mL rh-BMP4 (R&D) and 1 μM CHIR. On day 3, media was changed to RPMI supplemented with B27 without insulin and 1% penicillin/streptomycin. On day 7, media is changed again to RPMI supplemented with B27 with insulin and sustained in this final media for the duration of cardiomyocyte culture. Spontaneous beating in 2D culture was observed as early as day 9 or 10 after differentiation was initiated.

7. *Creation of Dual Post PDMS Mold for Cardiomyocyte culture*

PDMS post molds were fabricated using Sylgard 184 PDMS in 3D printed PLA molds. Briefly PDMS was poured into molds, placed under vacuum for 1 day at RT and cured at 80□ for 1 day prior to use[71]. Samples were sterilized in ethanol before cell culture, removed from molds and then used as a mold to cast PEG hydrogels. 6 Microwells were generated per one coverslip.

8. *3D hPSC Culture and Differentiation*

3D hPSC culture was conducted using either WTC11 (hiPSC) or H9 (hESC) however culture conditions for both cell lines were identical. hPSCs were maintained in an undifferentiated state through continuous passaging, cultured as colonies using feeder-free mTeSR-1 media supplemented with mTeSR Supplement on Geltrex coated tissue culture well plates. Passaging was performed using the enzyme-free ReLeaSR reagent while single cell suspensions were created using 1x ACCUTASE cell detachment solution. Cell encapsulation

was performed as single cell suspensions as previously described. Encapsulated cells were cultured in ROCK-inhibitor (Y-27632, STEMCELL Technologies) supplemented media for 2 days to achieve maximum viability.

Differentiation of 3D colonies was performed upon observing cavitated spheroid colony formation and consisted of treatment using known Wnt-exclusively modulated cardiac or kidney differentiation protocols or low concentration Wnt supplementation. All differentiation steps were performed in RPMI supplemented with B27 minus insulin and used known differentiation protocols[55,130]. Cardiac differentiation was conducted by treating hydrogel constructs with 6 μM Wnt activator, CHIR 99021 for two days followed by 2 μM PRCN inhibitor, Wnt-C59 for two days. Kidney differentiation was performed by treating colonies with 12 μM CHIR for 36 hours. Low Wnt activation was performed by treating constructs with 3 μM CHIR for two days followed by two days of 2 μM Wnt-C59. After differentiation protocols were completed, all cultures were subsequently maintained in RPMI plus B27 plus insulin. Colonies were imaged using brightfield microscopy.

E. Conclusions

Findings in this preliminary data section demonstrate the ability to create differentiated tissues within chemically defined hydrogels to better understand the relationship between matrix and tissue. These hydrogel platforms permit the survival and function of differentiated tissues, while simultaneously support and maintain hPSC pluripotency. As we have demonstrated here and elsewhere, click-based PEG hydrogels developed by our lab allow one to control the cell microenvironment through spatial and temporal control of matrix mechanics, chemistries, and biologically active moieties. Yet, while successes here demonstrate that, as a proof of concept, we can tune microenvironment to understand ECM-parenchyma cell interactions, organs consist of more than just specialized cells. To utilize these tissue-engineered constructs in regenerative medicine or in disease modeling, they must be scalable, reflect tissue organization, contain vasculature, and allow for perfusion of blood. To create complex tissues and begin to develop functional organs, we must better understand the relationship between parenchyma, matrix, vasculature, and blood.

In the two main aims of this thesis, I will demonstrate how we can use light-based techniques to create hierarchical 3D blood vessels with complete spatiotemporal control, study the interactions between endothelium and matrix, fabricate the smallest endothelialized vasculature to date, and utilize these capillary networks to understand the complex hematologic pathoetiology of malarial infection.

CHAPTER 5: AIM 1- MULTICELLULAR VASCULARIZED ENGINEERED TISSUES THROUGH USER-PROGRAMMABLE BIOMATERIAL PHOTODEGRADATION

As published in *Advanced Materials*, 29, 1703156 (2017)[125]

A. Abstract

A photodegradable material-based approach to generate endothelialized 3D vascular networks within cell-laden hydrogel biomaterials is introduced. Exploiting multiphoton lithography, microchannel networks spanning all size scales of native human vasculature are readily generated with unprecedented user-defined 4D control. Intraluminal channel architectures are fully customizable, providing new opportunities for next-generation microfluidics and directed cell function.

B. Introduction

Vascularity is an integral aspect of all organ systems as it facilitates transport of oxygen, nutrients, hormones, electrolytes, and cells to and from every tissue within the body[132]. This vast interconnected network helps ensure temperature, pH, oxygen, glucose, and salt homeostasis, permits organ-to-organ hormonal communication, and enables rapid humoral and cell-mediated immune responses through convective transport of blood constituents. As all cells require nutrients and oxygen throughout maturation, blood vessels develop early in embryogenesis and synchronously with the organ systems they support[133]. During this time, vessels constantly change their shape and size to adapt to tissue requirements; adult vascular geometry is therefore four-dimensionally complex and ordered, spanning many scales of size[134].

Hierarchical organization of large arteries, to smaller arterioles, to the smallest capillaries dictates blood flow distribution and minimizes turbulence while the large size range allows for varying function. Centimeter-sized vessels including the aorta permit large convective volume flow while micron-sized capillaries support mass transport through diffusion. Bridging these vessels of differing sizes and structure is a shared and continuous tunica intima lined with endothelial cells, which serves functionally to prevent thrombosis, interpret changes in blood flow and composition, and modulate vascular tone[135]. This complex, hierarchical, and endothelial-lined 3D vascular network is critical for all bodily functions and should not be ignored when developing pathological models or engineering synthetic tissues.

As blood vessels are essential for tissue function, many synthetic approaches to generate macro- and microvasculature *in vitro* have been attempted, largely through additive- or subtractive-based methodologies[136]. Additive techniques generate vascular constructs from the bottom up, either through stacking of 2D constructs[71] or layer-by-layer 3D printing[137–139], where void spaces intentionally left during manufacturing define construct vascularity. Though these approaches have proven successful in generating perfusable vessels of varying geometry, studying endothelial cell function[73], and modeling vascular pathology[69], limited 3D control has been afforded. Additive strategies further suffer from a frequent lack of cytocompatibility during material casting, preventing vessel creation in the presence of live cells, as well as an inability to generate channels with diameters smaller than a few hundred microns[140].

To circumvent the complications of additive manufacturing-based vessel engineering, researchers have turned to subtractive techniques in which a bulk material is generated first followed by vascular void space creation[141]. Of note are recent efforts towards creating complex

3D networks using sacrificial lattices. In their seminal work, Miller *et al* encapsulated 3D-printed sugar glass in bioactive matrices, and then dissolved the lattice to reveal patterned interconnected channel networks[67]. Though this approach enables rapid vessel generation within cell-laden materials, concerns remain over cellular hyperglycemic response following hydration. Moreover, because the sugar network itself is generated through additive manufacturing techniques, the strategy exhibits the same limitations with respect to vessel 3D control, confining features to those >150 μm in size and with limited overhang.

Here and in literature, it has been hypothesized that vascular networks featuring capillary-sized microvessels could be generated using light-mediated subtractive manufacturing techniques[142]. Rastered control of a focused laser within biomaterials enables user-specified vascular creation of virtually any shape[19,143]. Utilization of a pulsed laser source, whereby multiple photons must be absorbed in rapid succession to initiate material dissolution, enables micron-scale control over vessel structure in all three spatial dimensions and provides access to complex and hierarchical networks similar to those found *in vivo*. Vessel geometry can be altered dynamically at any time based on subsequent light exposure, thereby permitting full 4D control over network vascularity, potentially even in the presence of live cells. Despite this unmatched potential, the complete benefit of using light to generate vascular networks within tissue-engineered constructs has not yet been fully realized. Subtractive strategies employing light to date have relied on photoablative methods, whereby large intensities of high-energy light induces material degradation through non-specific chemical bond photolysis, extreme local heating, or microcavitation[144,145]. Though effective in controlling 3D channel geometry, the use of photoablation raises serious concerns over the effects of ablative laser light on cellular integrity

and processes while opening unanswered questions regarding the integrity of surrounding materials. To truly exploit the potential of light-based subtraction for vascular engineering, strategies that employ cytocompatible wavelengths and intensities of light to create multicellular 3D tissues remain in great need.

Herein we introduce a fully cytocompatible fabrication strategy involving precise molecular photolysis to generate complex 3D vascular networks within hydrogel biomaterials. Demonstrated in this work is a versatile class of synthetic peptide-polymer-based materials that supports cellular encapsulation, enzyme-mediated matrix remodeling, and biochemical customization with the capacity for photoprogrammable vascular formation. Through multiphoton lithography-assisted photoscission, perfusable vessels are created within photosensitive gels with features that span nearly all physiological size ranges of interest, hierarchical organization, and complete 4D control. It is further shown that photodegraded channels can be readily modified over time and to display user-defined intraluminal topographies, providing a new and unique route to regulate local cell functions through dynamic and specific biophysical interactions. Finally, we exploit these customizable materials to fabricate the smallest endothelialized vessels to date as well as multilayered vascular structures of unprecedented complexity in the presence of encapsulated stromal cells, signifying crucial steps towards engineering of functional synthetic tissue.

C. Results and Discussion

Photodegradable hydrogels were generated by strain-promoted azide-alkyne cycloaddition between poly(ethylene glycol) tetrabicyclononyne (PEG-tetraBCN, $M_n \sim 20{,}000$ Da) and a diazide-functionalized synthetic peptide [N_3-*o*NB-RGPQGIWGQG*RGDS*GK(N_3)-

NH_2] (**Figure 5-1**). The bioorthogonal nature of the SPAAC reaction enables cells to be encapsulated during hydrogel synthesis with high viability (**Figure 5-1B-C**)[19,119,124]. SPAAC-based networks form rapidly *via* a step-growth polymerization mechanism, ensuring that all material crosslinks include functionalities introduced by the synthetic peptide. Critically, the peptide crosslinker contains a photodegradable *ortho*-nitrobenzyl ester (*o*NB) moiety that undergoes defined molecular photolysis in response to pulsed near infrared light (λ = 740 nm), enabling programmable vessel formation using cytocompatible light within the optical window of biological tissue (**Figure 5-1D**)[19,124,143,146]. The peptide is also engineered to contain the fibronectin-derived, integrin-binding RGDS peptide sequence (italicized)[147]. known to promote general cell attachment, spreading, and proliferation (**Figure 5-1E**). RGDS is of particular interest in vascular engineering as it is binds the highly expressed and angiogenesis-mediating $\alpha_V\beta_5$ and $\alpha_V\beta_3$ integrins, critically associated with capillary sprouting and vascular endothelial growth factor receptor-2 regulation[148,149]. Finally, the crosslinker contains the GPQGIWGQ polypeptide sequence (underlined) that is susceptible to enzymatic cleavage by a wide variety of matrix metalloproteinases (MMPs)[37], ultimately enabling cell-mediated gel remodeling (**Figure 5-1F**). These combined aspects provide for a material that is cytocompatible, promotes endothelialization, supports matrix remodeling by encapsulated cells, and enables user-programmable vessel formation through well-defined photodegradation chemistry. Though photodegradable hydrogels have demonstrated substantial utility in dynamic cell culture[19,143,150,151], their usage has been confined to bulk material softening, surface erosion, or void creation isolated to locations within materials; perfusable vessel structures have not yet been created *via* biomaterial photodegradation.

To control gel photodegradation and vessel formation over single micron-resolved volumes while maximizing cytocompatibility, multiphoton lithography was employed. As multiphoton excitation requires near-simultaneous absorption of two independent photons, photochemically initiated events are largely confined to the laser focal point, thereby affording sub-micron control in all three spatial dimensions. Furthermore, by employing pulsed near infrared light whose wavelength falls within the optical window of biological tissue, precise photochemistries can be performed deep within materials while minimizing phototoxicity concerns for cells above and below the focal point. Since the photolabile *o*NB moiety is included in every hydrogel crosslink, complete photodegradation occurs rapidly as guided by programmed laser rastering and a computer-controlled piezoelectric stage. Though the theoretical x- and y-patterning resolution of this strategy is limited only by the wavelength of light employed, z-resolution and fabrication depth limitations are governed practically by the utilized optics (e.g., working distance of objective, laser power, wavelength). To permit real-time visualization of material photodegradation and channel formation, gels were fluorescently labeled with an azide-functionalized fluorescein during formulation. Channel patency and perfusability were then confirmed post-fabrication by flowing and nonspecifically coating channel walls with red-fluorescent polystyrene beads (FluoSpheres®, 0.22 μm or 2 μm diameter, Invitrogen) or direct endothelial seeding within channel lumens.

In order to demonstrate the wide range over which multiphoton photolysis can be utilized to create perfusable channels, five photodegraded vessels of decreasing widths and heights were generated in the Y-direction between two large inlet/outlet channels (500 μm diameter, separated by ~1.5 mm) introduced by needle-based subtraction molding in the X-direction (**Figure 5-2A-B**). Microvessels with cross sections as large as 200 μm x 200 μm and as small as 10 μm x 10

μm were generated. Fluorescent imaging of the entire channel lengths revealed complete material degradation, removal of sol material for all sizes, and facile perfusion with 0.22 μm diameter fluorescent beads. Perfusable channels could be photogenerated at any z-location throughout the entire gel thickness (1.2 mm, Supplementary Figure 5-7) without altering photodegradation parameters (e.g., laser intensity, voxel dwell time). To demonstrate that similar control over vessel structure is afforded in 3D, four parallel channels were generated in the Y-direction between the inlet and outlet channels, and then joined together at two locations by four interconnecting channels in the X-direction, and four interconnecting channels in the Z-direction (all with 50 μm x 50 μm cross sections, **Figure 5-2B-C**). Upon perfusion with fluorescent beads, intact lumens were observed with clear interconnecting channels in all three X, Y, and Z planes. As photodegradation can be initiated on demand, we sought to demonstrate that network structure could be evolved over time post-fabrication. Interconnected channels (40 μm x 40 μm cross sections) were modified sequentially through successive material photodegradation (**Figure 5-2D**). Channel patency was confirmed by fluorescent bead perfusion following iterative network alteration. Collectively, these studies highlight the ability to create and modify perfusable synthetic vasculature of user-defined size and geometry with unmatched 4D control.

Critical to the development of large-scale engineered tissue is the capacity to support cell metabolism through strategies extending past simple diffusion. In normal physiology, this is accomplished by a complex structural hierarchy of blood vessels where 3D branching allows for size-dependent function and directional flow control. Conversely, disturbance of physiological flow patterns as a consequence of pathologies like tumor growth can lead to abnormal neovascularization, disruption of endothelial function, and redistribution of blood flow[152,153]. Though recapitulation of vascular geometry has proven difficult to achieve through conventional

strategies (e.g., soft lithography, additive manufacturing), vessel customization afforded through channel photodegradation opens new doors towards recreating physiologically relevant structures. To demonstrate the unique capacity to create complex hierarchical vessel networks in a controlled 3D manner, a single channel (300 μm x 300 μm cross section) was generated in series with four smaller channels (100 μm x 100 μm cross sections) connected to sixteen even smaller channels (25 μm x 25 μm cross sections) (**Figure 5-3A-B**). This vascular network captures the structural complexity of blood vessel hierarchy, allows for study of complex 3D flow, and accentuates the power of multiphoton degradation in vascular construction and design.

In addition to creating hierarchical 3D structure, successful generation of vascular constructs for tissue engineering applications requires process scalability. To assess whether such scalability is afforded by photodegradation-based vessel fabrication, rapid prototyping of cm-sized fluidic networks was attempted. **Figure 5-3C** illustrates a perfusable device consisting of a single inlet and outlet (500 μm x 100 μm cross sections) connected by a distributing channel (500 μm x 3.5 mm x 100 μm) in series with eighteen additional smaller channels (2.5 mm x 100 μm x 100 μm). Furthermore, as overall channel geometry and architecture is fully user defined by controlled laser scanning, it is demonstrated that one can readily form biomimetic vascular networks that recapitulate native vasculature (**Figure 5-3D**). After biomimetic construct formation, red fluorescent beads (2 μm diameter) roughly the size scale of platelets were perfused and imaged as they travelled through the vascular network. Though material processing is likely to be slower than other techniques to generate large-scale vascular networks (minutes to hours depending on network design and light parameters), overall process cytocompatibility enables large networks to be generated without uncontrolled cellular perturbation. Together, these data demonstrate that multiphoton photodegradation enables stable vasculature to be

generated that recapitulates both the physiological size and complexity of native blood vessel networks.

While other techniques have demonstrated the ability to control channel network design, photodegradation-based subtractive strategies further and uniquely enable micromachining of intraluminal topography. Inspired by recent findings that topographical cues and geometries can alter cell adhesion, migration, differentiation, cytoskeletal organization, and morphology,[154,155] we sought to embed such physical cues locally within devices. Further recognizing a growing interest in creating cell capture-devices[156,157] to examine single cell function and behavior, we also sought to engineer customizable microtraps within channels. Though both tasks have proven impossible using conventional techniques, we hypothesized that such architectures could be generated readily within the lumen of microfluidic channels by multiphoton photolithography. In **Figure 5-4**, a microfluidic network consisting of a single inlet and three outlets was generated within a fluorescent hydrogel. Different intravessel architectures were sculpted into each of the three outlets. The first two outlets were created with parallel microgrooves (10 μm width) perpendicularly oriented between individual outlets, highlighting the ability to pattern channel microtopography. Within the third outlet, intravessel cell traps (~50 μm size scale) were successfully created and used for cell isolation (Supplementary Figure 5-8), demonstrating the capacity to micromachine 3D functional capture devices. We anticipate that such topographical microarchitectures will provide vascular engineers with new tools to simultaneously control endothelial cell function and study vessel structure, while probing perfusate and blood constituents in a novel and user-designed manner.

Native vascular networks are not only complex and hierarchical, but also endothelial-lined. To demonstrate that our photodegradable material is capable of generating and supporting

3D microvasculature, human umbilical vein endothelial cells (HUVECs) were perfusion seeded within the lumen of photodegraded channels generated in fluorescein-modified PEG hydrogels (**Figure 5-5**). Within these devices, two identical layers of parallel vessels (~100 μm x 100 μm cross sections) were stacked directly above each other (100 μm separation in the Z direction). Each layer was constructed with curved interconnecting channels in the XY plane (**Figure 5-5A-E**) while the two layers were connected together by circular vertical channels in the Z direction (100 μm in diameter) (**Figure 5-5F**). Curved interconnected channels were selected to encourage overall fluid flow within the device, increasing efficiency of cell seeding and perfusion through channels while limiting cellular accumulation and potential channel clogging, as well as to promote overall endothelial attachment and function[158]. Ten days following endothelialization, samples were fixed, stained for cytoskeletal actin (Alexa Fluor 532 Phalloidin) and nuclei (Hoechst 33342), and imaged by multiphoton fluorescent microscopy. Seeded HUVECs attached and spread to cover the walls of the photodegraded channel with well-formed lumens, indicating successful generation of endothelialized vessels. Finally, to probe the spatial limitations of endothelialization, microchannels with even smaller features sizes (cross sections of 45 μm x 45 μm, 60 μm x 60 μm) were also demonstrated (**Figure 5-5G-J**, Supplementary Figure 5-9). To our knowledge, this represents the smallest endothelialized synthetic vessel to date within a material that supports cell encapsulation.

Though synthetic vascular beds are extremely valuable tools in vascular biology and hemodynamics, the most basic and critical roles of blood vessels is to support complex organ function. To date, the ability to create 3D multicellular vascularized tissues remains one of the most critical – if not the most critical – engineering feats hindering the use of metabolically demanding engineered tissues clinically. While there are few demonstrations of controlled 3D

endothelialization, there are fewer still that permit simultaneous encapsulation of cells in the stroma and endothelialization without incurring cellular damage. To highlight that photodegradation can be performed in a cytocompatible manner, a single layer set of parallel channels with rounded interconnecting channels was generated in the presence of human bone marrow-derived hS5 stromal cells constitutively expressing green fluorescent protein (GFP). Four days after endothelialization with HUVECs, samples were fixed and subsequently imaged (**Figure 5-6**). hS5 cells above and below the photodegraded channels remained viable during the entire culture time course, as evidenced by their continued production of GFP as well as quantitative LIVE/DEAD analysis (Supplementary Figure 5-10). The ability to create customizable endothelialized vessels in the presence of encapsulated cells represents a powerful step towards engineering complex heterogeneous tissue for clinical transplantation. Ongoing work seeks to explore both the enzyme-mediated matrix remodeling of encapsulated cells and endothelial cells of differing origin in these matrices. Furthermore, interest exists in tailoring matrix sensitivity to endothelial cell specific MMP secretion.

D. Experimental Section

1. Synthesis of Diazide Peptide Crosslinker

H-RGPQGIWGQGRGDSGK(N_3)-NH_2 peptide was synthesized (0.5 mmol scale) by standard automated microwave-assisted Fmoc solid-phase methodologies (CEM Liberty 1). Synthesis was performed on Rink amide resin (ChemPep) using a C-terminal Fmoc-Lys(N_3)-OH (synthesized *via* known synthetic routes[159,160]). N-terminal couplings were performed by treating resin with protected amino acid (2 mmol), 2-(1H-benzotriazol-1-y1)-1,1,3,3-tetramethyluronium hexafluorophosphate (2 mmol), and N,N-diisopropylethylamine (2 mmol, DIEA) in a solution of dimethylformamide (DMF) and N-Methyl-2-pyrrolidone (9 mL and 2 mL, respectively) at 75 °C for 5 min. Fmoc deprotection reactions were performed using 1-hydroxybenzotriazole (0.1 M), piperidine in DMF (20 v/v%) at 90 °C for 90 s. Photodegradable azide functionality was then conjugated to the peptide's N-terminal amine by treating resin overnight with N_3-*o*NB-OSu[19] (0.65 mmol, 330 mg) and DIEA (2 mmol, 258 mg) in minimal DMF. Peptide deprotection and cleavage from resin was performed by two-hour treatment in trifluoroacetic acid (TFA)/triisopropylsilane/water (95:2.5:2.5 v/v%, 30 mL). Crude product was precipitated in and washed twice with ice-cold diethyl ether. The crude peptide was then purified using preparatory high-performance liquid chromatography (HPLC, C18 column) utilizing a 43.4 minute linear gradient (20-100%) of acetonitrile in aqueous TFA (0.1 v/v%). The final product was then lyophilized to yield a dark-yellow solid, denoted as N_3-*o*NB-RGPQGIWGQGRGDSGK(N_3)-NH_2. Peptide purity was confirmed by MALDI-TOF: Calculated for $C_{86}H_{129}N_{32}O_{29}^+$ $[M + {}^1H]^+$, to be 2073.9; observed 2072.6.

2. *Hydrogel Formation*

Hydrogels were formed by combining PEG-tetraBCN (M_n ~ 20,000 Da, synthesized as previously described)[124] with the diazide N_3-*o*NB-RGPQGIWGQGRGDSGK(N_3)-NH_2 peptide in a 1:2 stoichiometric ratio in either phosphate buffered saline (PBS, pH = 7.4) or stromal cell culture media (described below) to achieve a final 7 wt% of prepolymer solution. This mixture was then quickly pipetted between two glass coverslips (one Rain-X® treated, the other untreated) separated by silicone spacers (thickness = 500 μm) and allowed to react for 1 hour at room temperature. After gelation, the Rain-X® coated coverslip was removed, yielding hydrogels of defined thickness that remained bound to the untreated glass coverslip. For fluorescein-conjugated hydrogels, PEG-tetraBCN (0.01 mmol) was pre-reacted with 5-FAM azide (AAT Bioquest, 0.002 mmol) in PBS for 2 hours at room temperature. Product was then dialyzed (MWCO ~ 1kDa, Spectra/Por® 7) against water, lyophilized, and reconstituted in PBS. To form fluorescent hydrogels, FAM-conjugated PEG-tetraBCN was mixed with unconjugated PEG-tetraBCN in a 1:10 ratio and then reacted with diazide peptide crosslinkers as described above.

3. *Multiphoton Photodegradation*

Photodegradation was performed by multiphoton lithography using an Olympus FV1000 MPE BX61 Microscope equipped with a variable wavelength Mai Tai DeepSee Ti:S laser with a maximum power of 2.7W and a water-immersion objective lens (25x, NA = 1.05) (Garvey Imaging Center, University of Washington) in conjunction with Olympus FluoView imaging software. Channel patterns within a single field of view (500 μm x 500 μm) were generated by defining regions of interest followed by laser rastering to intended Z-depths (Z-step size = 1 μm).

Networks larger than a single field of view were programmed by stitching together single fields of view with defined regions of interest using the FluoView mosaic feature. Individual scans were performed at $\lambda = 740$ nm using 1.9W laser power with a pixel dwell time of 2 μs and with 5-7 frame repeat scans to ensure complete photodegradation.

4. Endothelialization of Photodegraded Channels

HUVECs were cultured in Endothelial Cell Basal Media (Lonza) supplemented with Endothelial Cell Growth Media (EGM) SingleQuots (Lonza). Cell cultures were passaged upon reaching 80% confluency onto gelatin-coated tissue culture flasks and were used prior to passage 8. Seeding of endothelial cells within channel lumens was performed by trypsin treatment (0.05 mM in PBS, 5 min) of HUVEC monolayers, centrifugation, and media washing, followed by direct pipetting of cell solution (5×10^7 cells mL^{-1}) onto device microchannel inlets. Capillary action and differential pressure pushed the cell-rich solution through the channel network. Cells were allowed to attach to vessel walls for 1 hour, rinsed twice with growth media, and maintained in culture (37 °C, 5% CO_2).

5. 3D Cell Encapsulation and Cell Culture

Human bone marrow-derived hS5 stromal cells constitutively expressing GFP were cultured in RPMI 1640 basal media (Corning) supplemented with fetal bovine serum (10%, Corning) and penicillin/streptomycin (1%, Corning). Cells were trypsinized and passaged upon reaching 80% confluency. To prepare cells for encapsulation, stromal cells were treated with trypsin (0.05 mM in PBS, 5 min), centrifuged (1,200 RPM for 4 mins), and resuspended in hydrogel precursor formulations (5×10^6 cells mL^{-1}). Mixtures were gently vortexed to ensure

homogenous encapsulation, pipetted onto coverslips, and allowed to gel at room temperature (1 hr). After microchannel fabrication and endothelialization, hydrogels containing encapsulated hS5 stromal cells and HUVEC endothelialized vessels were maintained using EGM SingleQuot-supplemented Endothelial Growth Basal Media.

6. Cellular Staining and Visualization

Constructs were fixed by replacing culture media with and gently perfusing formaldehyde in PBS (3.7 wt/vol %, 30 min). Fixative was removed by performing three PBS washes (5 min each). To minimize nonspecific binding and to permeabilize cells, constructs were incubated in PBS containing bovine serum albumin (BSA, 3 wt/vol %) and Triton X-100 (1 vol/vol %) for 1 hr. Samples were then stained using either or both Alexa Fluor 532 Phalloidin (1:100, Thermo Fisher Scientific) and Hoechst 33342 (1:1000, Thermo Fisher Scientific) in PBS supplemented with BSA (1 wt/vol %). Imaging was performed by multiphoton microscopy (Olympus FV1000 MPE BX61), with data analysis and visualization performed with FluoView (Olympus), ImageJ (NIH), and Imaris software (Bitplane).

E. Figures:

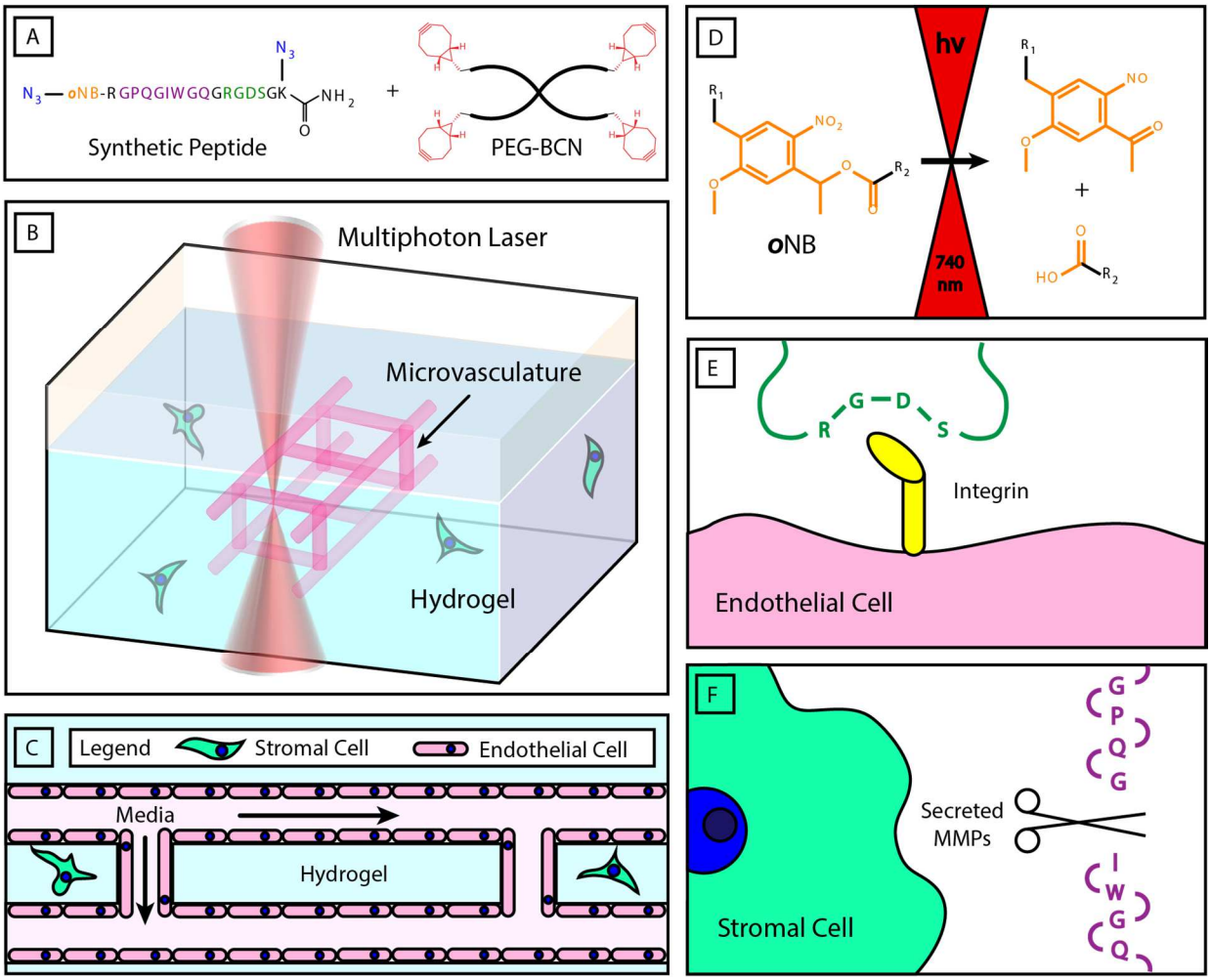

Figure 5-1: Schematic outline of hydrogel design and vessel fabrication

A) Hydrogels are generated by cytocompatible strain-promoted azide-alkyne cycloaddition (SPAAC) between a poly(ethylene glycol) tetrabicyclononyne (PEG-tetraBCN, where BCN is shown in red) and a diazide-modified synthetic peptide (azides shown in blue). The peptide contains a photodegradable ortho-nitrobenzyl linker (oNB, orange), a matrix metalloproteinase (MMP)-cleavable sequence (GPQGIWGQ, purple), and a cell-adhesive region (RGDS, green). B) User-programmed multiphoton excitation induces localized degradation of the hydrogel through oNB photocleavage, resulting in the microchannel (pink) generation in the presence of encapsulated stromal cells (green). C) Photodegraded networks are then seeded with endothelial cells (pink) to created cell-laden hydrogels with perfusable, endothelialized vasculature. D) oNB photocleavage yields nitroso- and acid-terminated byproducts. E) RGDS moieties included within the peptide crosslinker promote cell attachment and proliferation. F) The GPQGIWGQ peptide sequence is cleaved enzymatically by secreted MMPs, enable cell-mediated matrix remodeling of the hydrogel network.

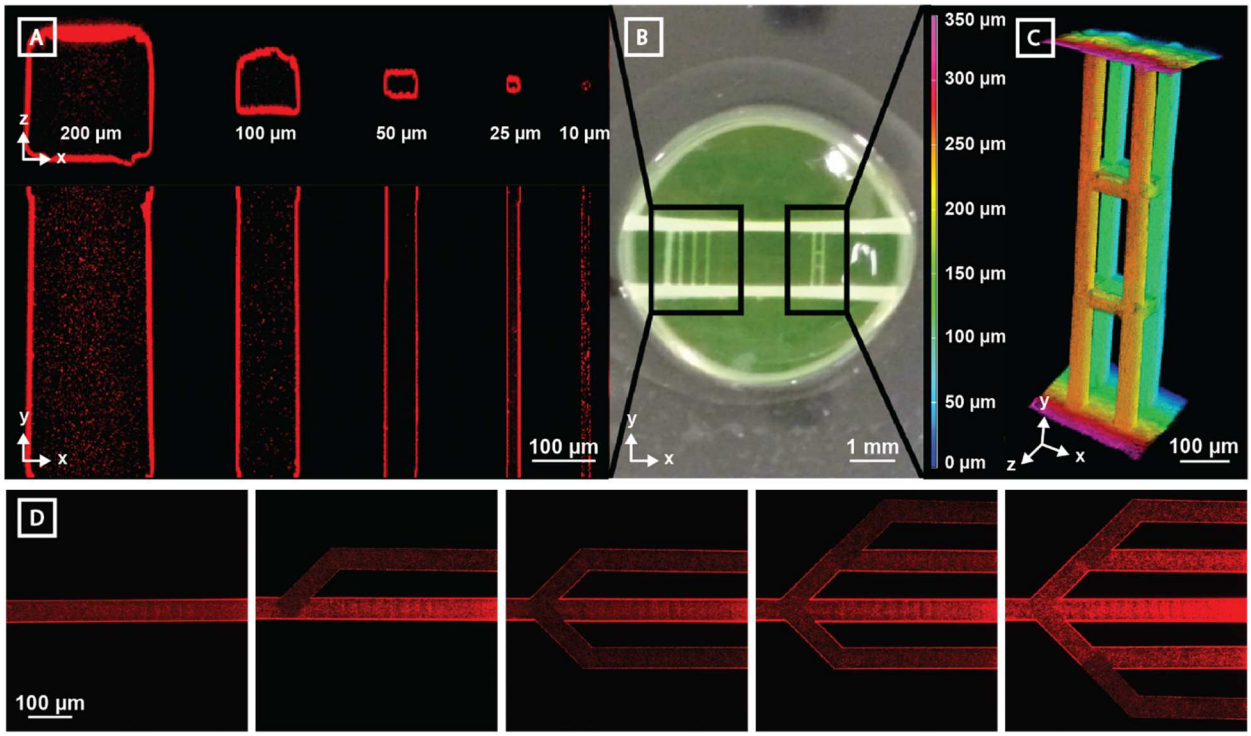

Figure 5-2: Microvessel generation is readily controlled in 3D with micron-scale resolution

Vertical channel sets were generated between two horizontal channels (~500 µm diameter) spaced ~1.5 mm apart. Vessel perfusion with fluorescent polymer beads (red, 0.22 µm diameter) enabled channel visualization by multiphoton microscopy. **A)** Channels with a wide range of cross-sectional sizes (200 µm x 200 µm, 100 µm x 100 µm, 50 µm x 50 µm, 25 µm x 25 µm, and 10 µm x 10 µm) are fully patent. **B)** Photographic image of hydrogel displays both parallel microchannel and 3D multilayered channel sets. **C)** Photodegraded channels can be generated with full 3D control. Four parallel 50 µm x 50 µm (width x height) channels generated in the Y direction (X-spacing = 150 µm, Z-spacing = 100 µm) connect the horizontal channels. 8 bridging channels (50 µm x 50 µm, cross sectional) interconnect features in the X and Z directions. Microbead fluorescence is viewed using Z-depth color-coding. **D)** Perfusable vascular network geometry can be altered over time through iterative network photodegradation (channel cross section of 40 µm x 40 µm, red beads = 0.22 µm diameter).

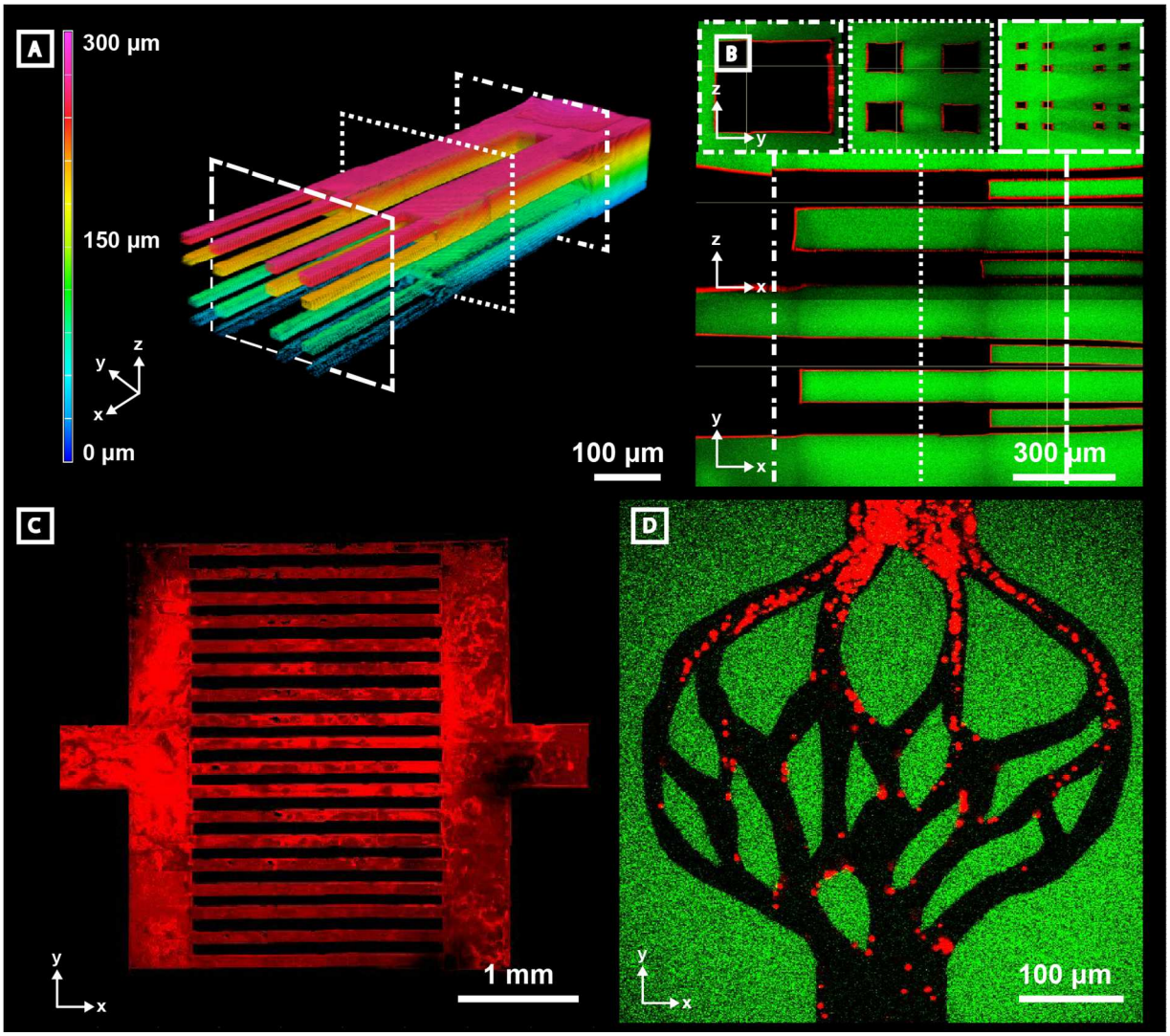

Figure 5-3: Microvessels generated by programmable photodegradation exhibit complex hierarchy, scalability, and biomimetic design.

Channels were generated in fluorescein-modified hydrogels (green) and perfused with fluorescent microbeads (red, 0.22 µm diameter in A-C, 2 µm in D). **A)** A 3D hierarchical vascular network is visualized using Z-depth color-coding of fluorescent beads. Device is comprised of one 300 µm x 300 µm channel which branches into four 100 µm x 100 µm channels and then terminates in 16 channels, each with 25 µm x 25 µm cross section. Each segment was approximately 500 µm in length in the X dimension. Corresponding dashed squares indicate respective cross sections demonstrated in panel B. **B)** Cross-sectional views of the branched microvascular network indicate intact vascular lumens. **C)** A centimeter-sized device was generated by creating two 500 µm x 500 µm x 100 µm inlets and outlets connected by two 500 µm x 3.5 mm x 100 µm distributing channels joined by 18 individual 2.5 mm x 100 µm x 100 µm (X x Y x Z dimensions) connecting channels. **D)** Biomimetic vascular networks can be created with user-defined geometrical control.

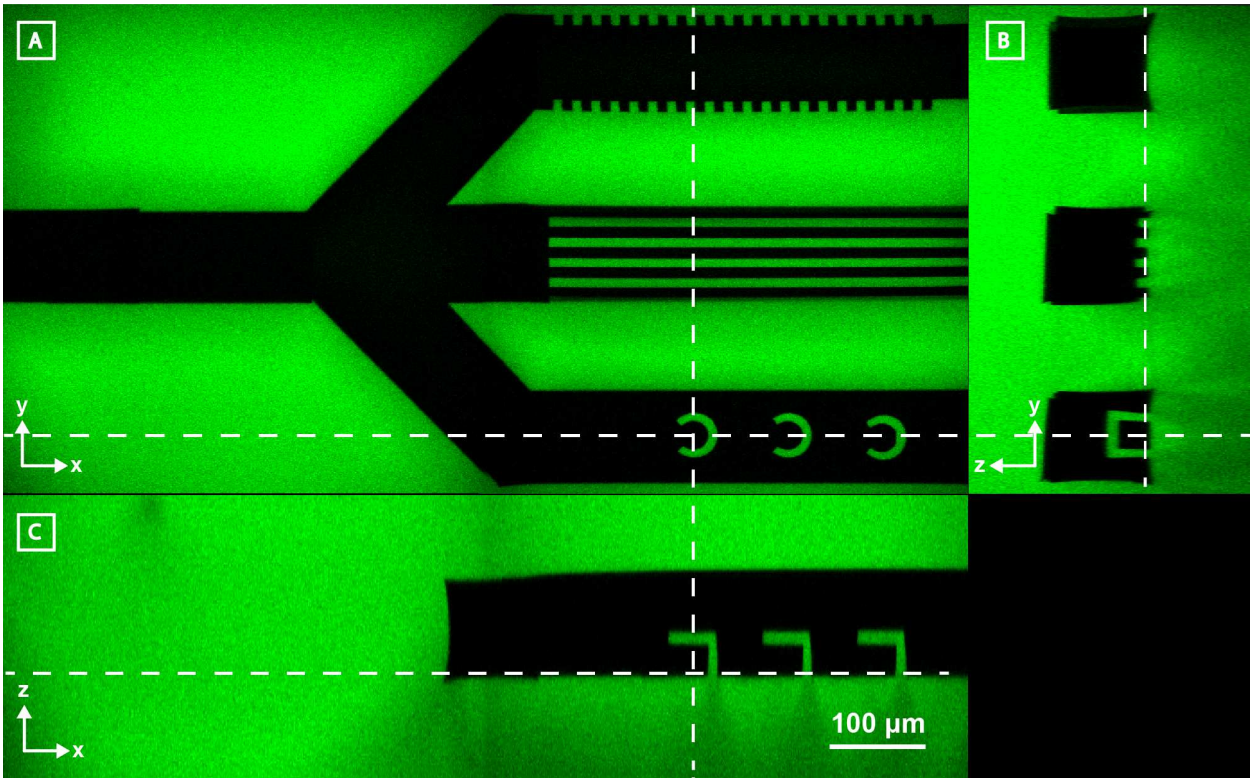

Figure 5-4: Photodegradation-mediated microfabrication of intraluminal channel architectures within hydrogel biomaterials

A-C) Z, Y, X cross-sectional views of a three-branched channel modified with different intraluminal architectures. The top channel has been micromachined to contain microgrooves in the XZ plane, the middle microgrooves in the XY plane, and the bottom cylindrical cell traps. Dashed lines indicate cross-sectional areas as observed in each of the three perspective views. All images are to scale.

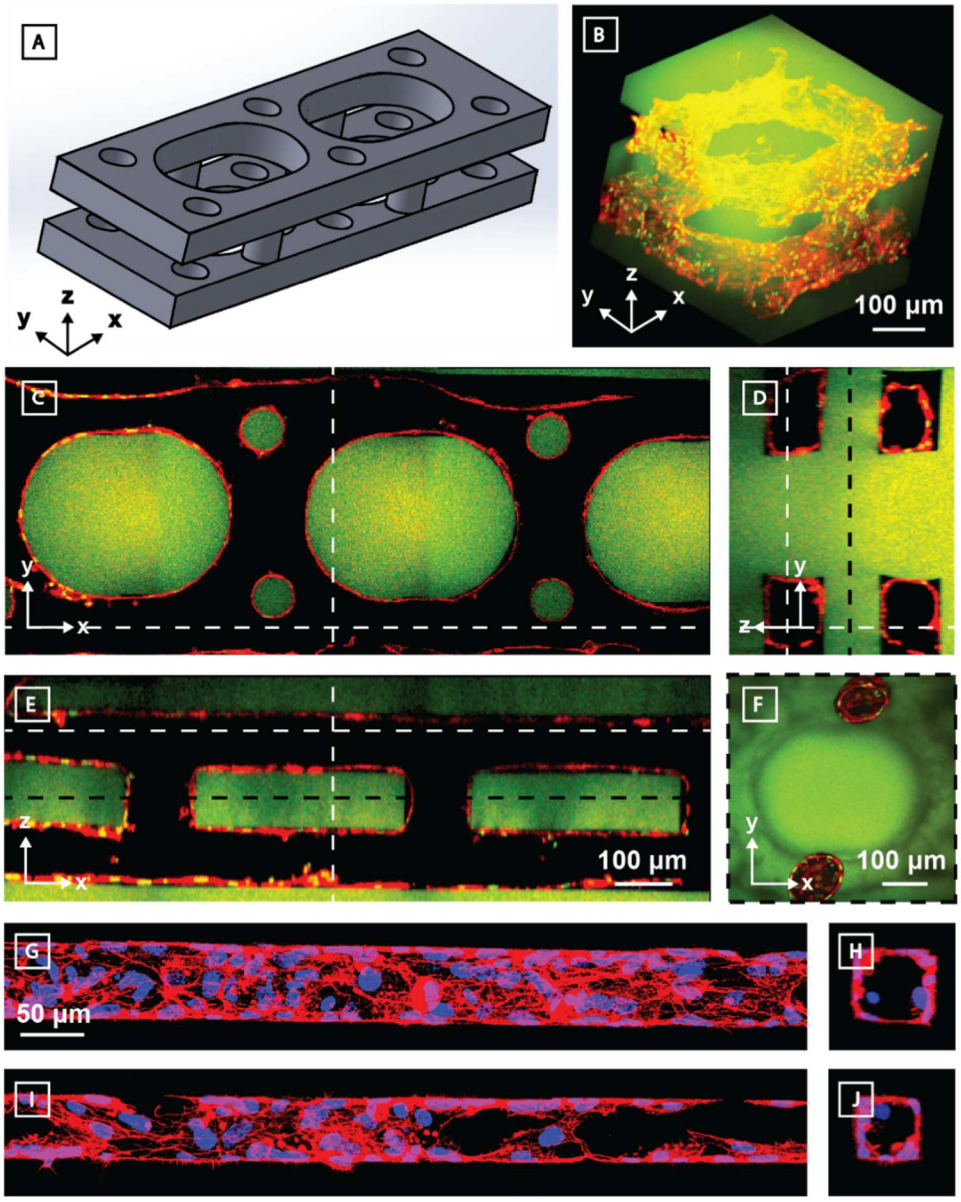

Figure 5-5: 3D endothelialized channels generated within photodegradable fluorescent gels

Two identical parallel-oriented channels are interconnected with cylindrical channels in the Y-direction. 10 days following microvessel endothelialization with HUVECs, samples were fixed and stained prior to imaging by multiphoton microscopy. F-actin is shown in red, nuclei in green. **A)** 3D model of patterned channels. Endothelialized sample is visualized **B)** as a 3D render and **C-F)** as Z-, X-, and Y-cross sectional views. Dashed white lines indicate cross-sectional areas observed. An additional Z-cross-sectional area between the two channel sets (location denoted by dashed black line) demonstrates interconnectivity in the Z direction. Endothelialization of **G-H)** 60 µm x 60 µm and **I-J)** 45 µm x 45 µm (width x height) channels was obtained. F-actin is shown in red, nuclei in blue. G) and I) represent XY projections; H) and J) are YZ slices. C-E) are all to scale, as are G-J).

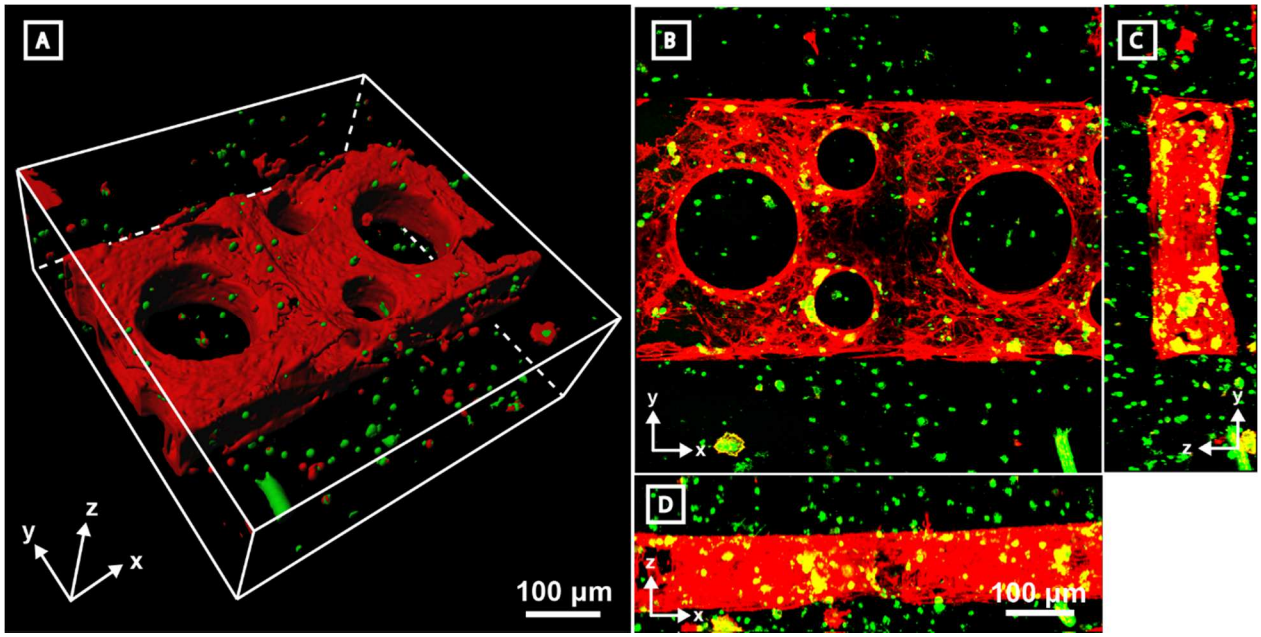

Figure 5-6: Endothelialized channels are readily fabricated in the presence of encapsulated stromal cells

A single-layer channel was generated by photodegradation in the presence of encapsulated GFP-expressing hS5 stromal cells (green). Channels were then endothelialized with HUVECs, cultured for 4 days, fixed, and stained for F-actin (red) prior to imaging by fluorescent multiphoton microscopy. Co-stained and single-stained green cells are identified as hS5 cells while singly red-stained cells represent HUVECs. Sample is viewed **A)** as a 3D surface render of a 300 µm Z-stack and **B-D)** as Z-, X-, and Y-direction maximum intensity projections. B-D) are all to scale.

F. Supplemental Information

1. Photogeneration of Microchannels at Various Depths Throughout Gels

To assess whether photodegradation was significantly hindered as a function of depths below gel surfaces, we sought to generate identical channels at increasing Z coordinates. Hydrogels (~1.2 mm thick) were generated as previously described followed by photodegradation of 11 channels (30 µm x 30 µm cross sections) spaced at 100 µm increments throughout the full construct thickness. Each degraded channel was generated 100 µm below in the Y direction to ensure an unobstructed laser path. Channels were visualized with red fluorescent beads (0.22 µm diameter) in conjunction with multiphoton microscopy.

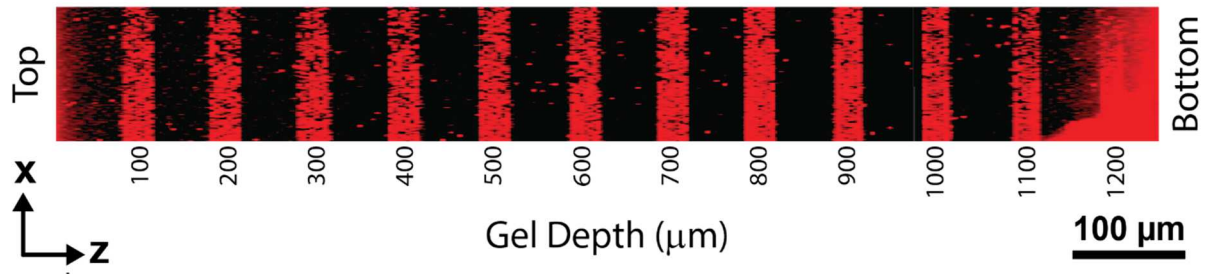

Figure 5-7: Photodegraded microvasculature can be generated throughout thick samples

Channels (30 µm x 30 µm cross sections) were generated in PEG-peptide hydrogels at increments of 100 µm in the Z direction and then filled with red fluorescent beads (0.22 µm diameter). Vascularized constructs were imaged by multiphoton microscopy and displayed as a maximum intensity projection across the XZ plane. Perfusable channels were observed throughout the entire thickness of the sample.

2. *Live Cell Capture within Microfabricated Intravessel Cell Traps*

Fluorescent hydrogels were generated by mixing FAM-conjugated PEG-tetraBCN with unconjugated PEG-tetraBCN (1:20) and then reacted with diazide peptide crosslinkers as previously described. Channels (300 μm x 100 μm cross sections) were generated that contained two different intravessel cell trap designs: one type similar to those depicted in **Figure 5-4**, and a second containing a small outlet to encourage media flow through the cell capture device. Networks were perfused with media containing hS5 stromal cells (10^6 cells mL^{-1}). Successful capture events were imaged using brightfield microscopy.

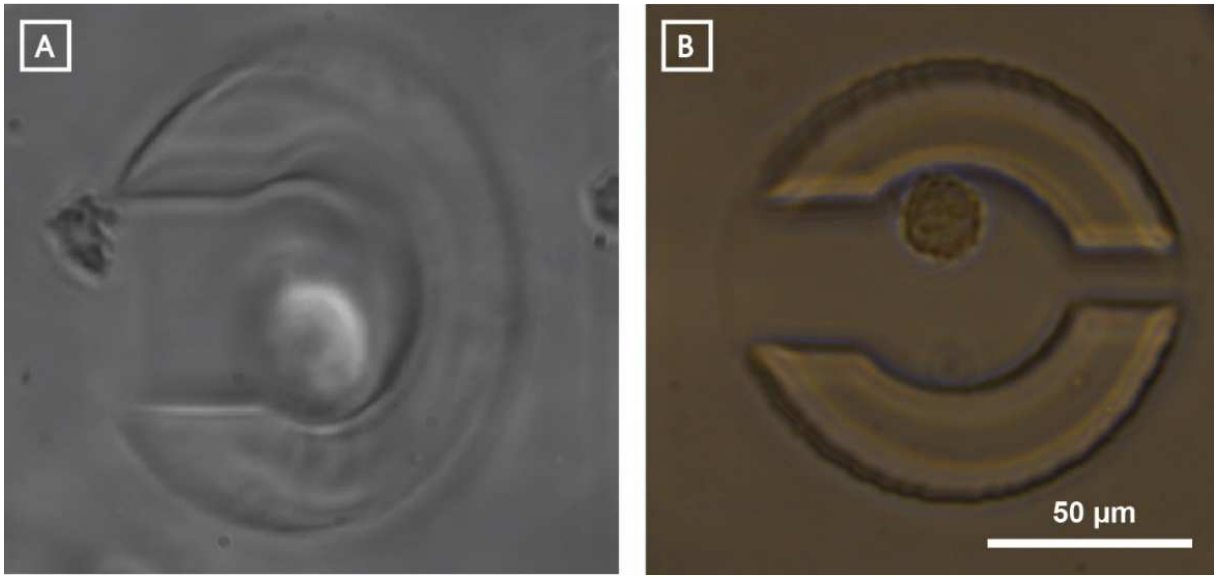

Figure 5-8: Intraluminal single cell traps.

Photodegraded channels (300 μm x 100 μm cross section) were generated containing single-cell capture devices (outer diameter = 100 μm, inner diameter = 50 μm) **A)** without or **B)** with an outlet to encourage flow through the capture device. Perfusion of cell suspensions (10^6 hS5 cells mL^{-1}) in stromal cell growth media revealed individual cell capture events, as imaged by brightfield microscopy.

3. Endothelialization of Photodegraded Channels with Sub-100 µm Feature Sizes

To assess the capacity of HUVECs to endothelialize channels with sub-100 µm feature sizes, 60, 45, and 30 µm square cross-sectional microchannels were photodegraded in non-fluorescent hydrogels (generated as previously described). HUVECs (passage 7) were perfused through the device by direct pipetting of cell solution (5 x 10^7 cells mL^{-1}) onto device microchannel inlets. Cells were allowed to attach to vessel walls for 1 hour, rinsed twice with growth media, and maintained in culture (37 °C, 5% CO_2). Brightfield images were acquired 6 hours after attachment.

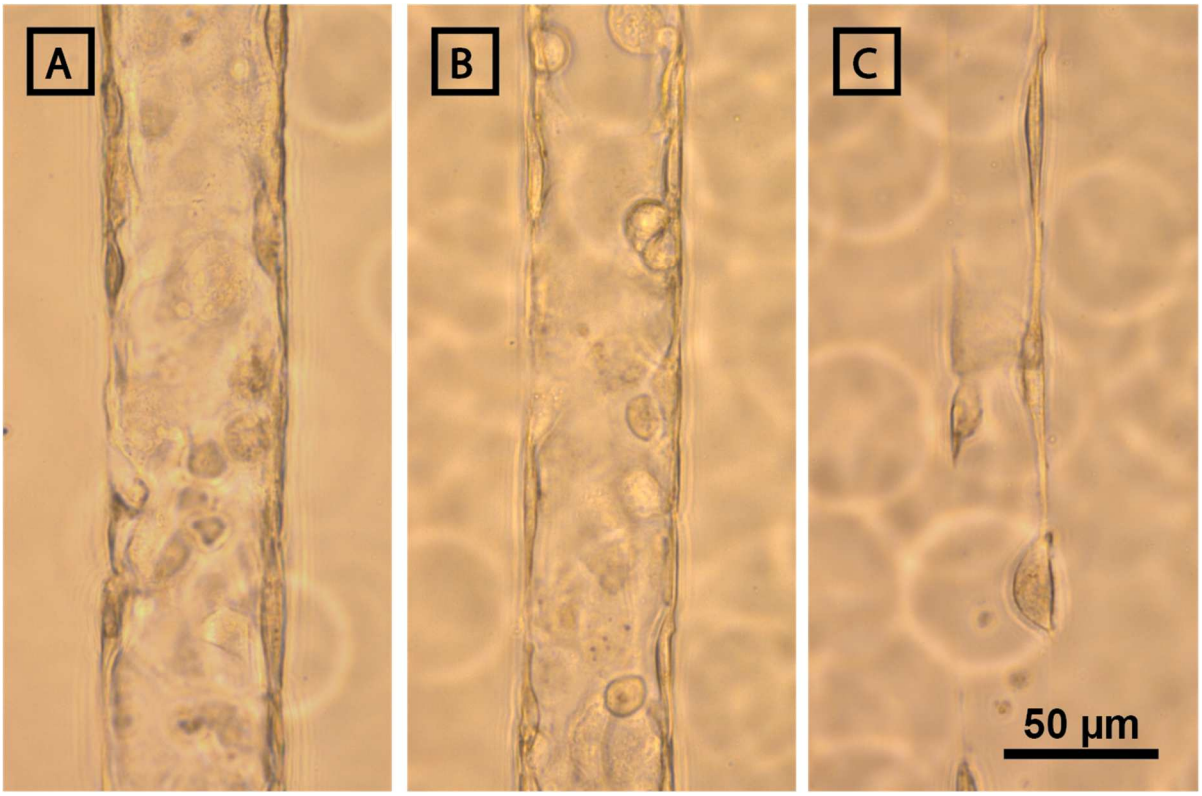

Figure 5-9: Sub-100 µm photodegraded channels are readily endothelialized.

A) 60, B) 45, and C) 30 µm square cross-sectional photodegraded channels were generated in non-fluorescent hydrogels and subsequently endothelialized. Brightfield Images were acquired 6 hours post endothelialization. All images are to scale.

4. Cell Viability Post-Encapsulation and Vessel Fabrication

Hydrogels (7 wt% total prepolymer) were formed by combining PEG-tetraBCN (M_n ~ 20,000 Da) with diazide N_3-*o*NB-RGPQGIWGQGRGDSGK(N_3)-NH_2 peptide (1:2 stoichiometric ratio) in stromal cell culture medium containing hS5 cells ($5*10^6$ cells mL^{-1}). 24 hours after encapsulation, a single 100 μm x 50 μm channel was generated in the cell laden hydrogel. After a 2 hour incubation at 37 °C, hydrogels were then stained with calcein-ethidium homodimer using a LIVE/DEAD assay (Invitrogen) at 37 °C for 20 mins. Samples were then imaged by confocal microscopy to a Z-depth of 300 μm and then displayed as a maximum intensity projection of the XY plane. Comparing areas above and below the location of channel degradation with other locations throughout the material reveals little difference in viability; viability above and below channel fabrication were ~92%, while those outside degradation regions were ~93%.

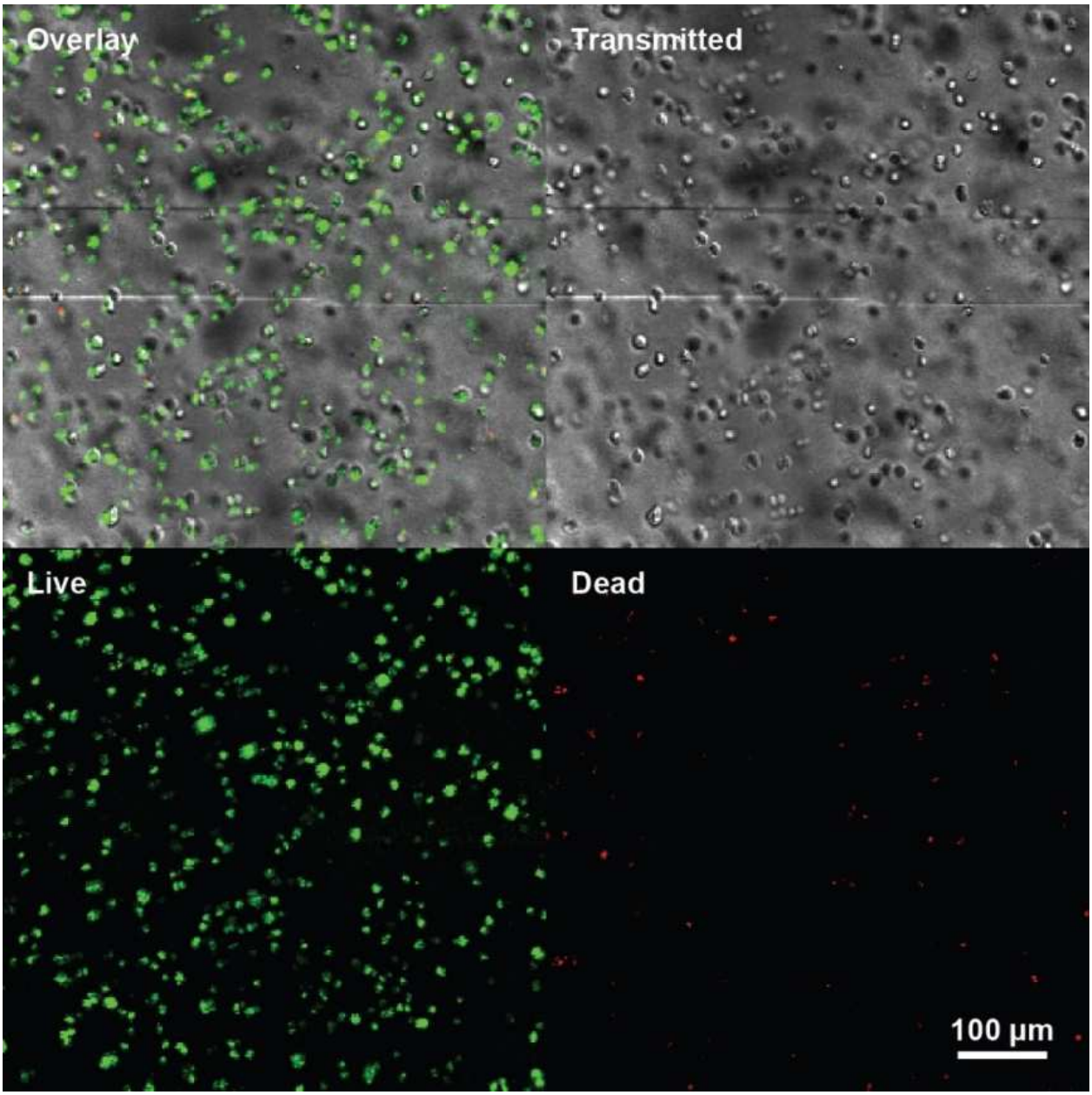

Figure 5-10: Encapsulated stromal cells remain viable above and below areas of microchannel fabrication.

Channel fabrication was performed in cell-laden hydrogels containing encapsulated hS5 stromal cells (5 x 10^6 cells mL^{-1}) and then stained with a LIVE/DEAD kit (Invitrogen, green = live, red = dead). No significant difference in viability was observed for regions above vessel patterning compared with those elsewhere in the material.

CHAPTER 6: AIM 2 - BIOPHYSICAL AND BIOMOLECULAR INTERACTIONS OF MALARIA-INFECTED ERYTHROCYTES IN ENGINEERED HUMAN CAPILLARIES

A. Abstract

Plasmodium falciparum malaria is one of the deadliest and most prevalent infectious diseases, claiming an estimated half-million lives per year[161]. Severe disease is associated with massive parasite sequestration in the capillary and post-capillary venules, with multi-organ system failure and complications. It has been hypothesized that sequestration may result from a combination of parasite-induced pathologic alterations to host erythrocyte biomechanical and cytoadhesive properties yet, as no model system of human malaria infection exists, the exact mechanisms giving rise to sequestration in these small-diameter vessels remains unclear. To meet this need, we developed the first fully engineered *in vitro* human capillary model and utilize this platform to study IRBC sequestration in small-diameter microvasculature. Our capillary model is validated through the perfusion of single RBCs through capillary networks demonstrating both normal and pathologic RBC modes of motion while confirming IRBC mechanical stiffening. Comparison of IRBCs diluted within physiological hematocrits at severe infection parasitemia revealed no evidence of mechanical trapping while indicating synergistic effects of mechanical stiffening and cytoadhesion. Recapitulation of post-capillary venule sequestration with greater vaso-occlusion observed in virulent parasite strains reflects observations previously only observed in post-mortem autopsies.

B. Results and Discussion

Sequestration of *Plasmodium falciparum*-infected red blood cells in capillaries and post-capillary venules is central to development of severe malarial disease[89]. As sequestration moves upstream into the capillaries and pre-capillaries, disease-associated mortality also increases[87]. IRBCs display knob-like protrusions that stiffen the erythrocyte membrane[94], as well as membrane-bound PfEMP1 ligands that mediate cytoadhesion to the vascular endothelium[101]. Both knobs and PfEMP1s are thought to contribute to sequestration and disease severity[162–165]. How these mechanisms cause sequestration in small-diameter vessels remains unclear due to lack of an appropriate animal model[166] and difficulties recapitulating the capillary microenvironment *in vitro*.

PDMS-based microfluidics have demonstrated thresholds for mechanical trapping of IRBCs in the absence of cytoadhesion[167], while endothelialized models have established shear- and PfEMP1-dependent cytoadhesion in geometries where effects of mechanical trapping are negligible. These models fail to recapitulate the cellular and geometric properties of the capillary, where cytoadhesion and stiffening may both contribute to sequestration. As vessel size approaches the size of blood constituents, the two-phase nature of blood becomes increasingly important, and unique blood cell dynamics not observed in large-diameter vessels arise. Under these geometric constraints, RBCs must deform to traverse the capillary; however IRBC deformability decreases by up to ten-fold upon malaria infection[168]. In addition to difficulties traversing physical constraints, reduced deformability can give rise to margination of stiffened IRBCs toward the vessel wall as more deformable RBCs migrate to the vessel axial center due to flow velocity gradients[112]. Together, margination and geometric confinement simultaneously increase endothelial-blood cell contact as well as the frequency, duration, and extent of

interactions between PfEMP1 and host receptors. These factors, uniquely observed in small-diameter vessels, may drive parasite tropism for capillary and post-capillary endothelium. Here, we present the first demonstration of endothelialized *in vitro* capillaries with controllable geometries and utilize this platform to understand the individual contributions of cytoadhesion and mechanical stiffening to sequestration.

Capillary networks were rapidly fabricated using a two-step process wherein multiphoton photoablation was used to anastomose two parallel main channels (d = 200 μm, spaced 450 μm apart- Supplementary Figure 6-4) created in collagen by soft lithography (7.5 mg/mL, ~200-500 Pa[169]). Channels were seeded with endothelial cells and cultured under gravity-driven flow for 3-7 days (as in previous work[170]) prior to photoablation-mediated capillary network generation. Here, a multiphoton microscopy-guided femtosecond laser is used to induce optical breakdown of the collagen in defined regions (**Figure 6-1A**). By programming laser paths in conjunction with a piezoelectric motorized stage, void spaces of user-defined and physiologically relevant geometries were generated. Over an 18-hour period after photoablation, endothelial cells readily migrated into void space regions and were observed to form stable 20 μm diameter vessels (**Figure 6-1B-C,** Supplementary Figure 6-5).

We first sought to determine the fabrication limitations of capillary generation. To confirm void space creation, regions were visualized before and after photoablation using second harmonic generation imaging of collagen fibers (Supplementary Figure 6-6) and then perfused with red fluorescent polystyrene beads (0.22 μm diameter, Supplementary Figure 6-7). Perfusable networks could be generated with vessels as small as 5 μm in diameter and at densities roughly ten times the capillary density observed in the human heart (~11,600 vs 1,100 capillaries/mm^2 *in vivo*[171]).

As endothelial cells actively remodel collagen, we then sought to determine how endothelialization affects capillary density and lumen diameter. 2 x 2 arrays of straight channels consisting of either 10 μm or 20 μm diameter vessels spaced 5, 10 or 20 μm apart were created. 7-day culture revealed that vessels could be generated as close as 20 μm from each other while still maintaining vessel diameter fidelity (Supplementary Figure 6-8). When vessels were spaced 5 or 10 μm apart, collagen was enzymatically degraded by the seeded endothelial cells, resulting in vessel fusion. Cryosectioned 20 μm diameter vessels exhibited clear lumens upon H&E staining and deposited abundant type IV collagen suggesting the generation of a robust basement membrane (**Figure 6-1D-E**). In contrast, 10 μm diameter capillaries consistently displayed patchy endothelial coverage. Interestingly, both 20 μm and more commonly 10 μm capillaries demonstrate regions where a single endothelial cell forms the entire capillary lumen, suggesting regions of self-signaling and junction formation with itself (Supplementary Figure 6-8). Using this design, only 20 μm diameter capillaries maintained uninterrupted endothelial cell coverage.

Comparisons of stable and unstable capillaries revealed a distinct relationship between vessel aspect ratio (length (l): lumen width (w)) and capillary stability (Supplementary Figure 6-9). 20 μm diameter vessels demonstrated continuous endothelialization over nearly the entire vessel length (365 ± 105.4 μm) while 10 μm diameter capillaries were observed to only be stable over 126.7 ± 60.2 μm, corresponding to aspect ratios (AR) of 18.3 ± 5.3 and 12.7 ± 6.0, respectively. These findings approach human *in vivo* measurements where capillaries average 60 - 100 μm in length[71,172].

As fabrication is not constrained by vessel design (Supplementary Figure 6-10), considering aspect ratio criteria, and to better represent the hierarchical change in vessel diameter observed *in vivo*, channels were fabricated in a constrict-type geometry. Five symmetric regions

were created: distally a precapillary arteriole and post capillary venule (w = 40 μm, AR: 2.1), two transition regions (w = 40 μm to 5 μm), and medially a capillary (w = 5 μm, AR: d). In addition, vessel design effectively decreased the length of smallest portion of the capillary, further encouraging cell ingrowth and uninterrupted endothelial coverage. After 7-14 days of culture, these new constriction-shaped vessel designs demonstrated robust, consistent, and perfusable 5-10 μm diameter capillaries (**Figure 6-1F-H**). In contrast, a comparable angiogenesis model, in which capillary regions were left unablated and capillaries were allowed to sprout across the same 100 μm distance, resulted in vessels with uncontrolled directionality and diameter (average diameter = 36.96 +/- 15.51 μm) (Supplementary Figure 6-11). Culture of constriction vessels longer than 14-day periods resulted in capillary widening upon endothelial remodeling of the collagen matrix.

Having constructed stable endothelialized capillaries, we sought to study their importance on physiological and pathological red blood cell dynamics, deformation, and sequestration. We perfused red blood cells through constriction-design channels at velocities similar to *in vivo* capillary flow rates (≈ 250 – 1500 μm/s) and captured their motion using high-speed video **(Figure 6-2A-B)**[173]. Red blood cells readily traversed channels as small as 6 μm in diameter, reorienting and elongating along their major axes by up to two-fold. In the capillary region, red blood cells assumed a variety of deformations, including parachute-like, slipper-like and discocyte shapes, in agreement with prior *in vivo* observations[174], computational simulations[175], and microfluidic studies (**Figure 6-2C**). To further characterize deformation dynamics, we developed and implemented an edge detection-based image analysis regime to track the position, velocity, shape, and orientation of individual red blood cells throughout the channel (**Figure 6-2D,** Supplementary Figure 6-12). Experiments revealed two major modes of

motion: 1) elongating, characterized by stretching along the major axis, and 2) tumbling, characterized by oscillations in major axis orientation. These observations validate our capillary model and reflect similar modes of motion reported in microfluidic models[176].

As intraerythrocytic development is thought to alter deformability, we next sought to characterize how these changes manifest under shear flow by perfusing 2G2, a knobless IRBC variant[99]. In contrast to normal RBCs under equal flow, 2G2 exhibited less elongation and greater tumbling frequencies while traversing the constriction vessel. To gain further insight into the deformation behavior of IRBCs, we selected elongating RBC and IRBC from each experiment and compared normalized elongation for both groups. Strikingly, IRBC reached maximum elongation earlier and exhibited a slightly decease in maximum elongation compared to RBC. Taken together, these findings suggest that IRBC show altered deformation and motion through capillaries compared to RBC. As rolling and tumbling along the microvascular endothelium enhances cytoadhesion at high shear stress[177], we hypothesize that these differences in deformability may both enhance malaria-infected red blood cells' ability to either mechanically trap or cytoadhere in capillaries.

In the microcirculation, IRBCs are subjected to hydrodynamic interactions with uninfected RBCs, which promote IRBC margination toward the vessel wall, enhancing cytoadhesive interactions with endothelial cells[112,178]. We sought to understand how IRBCs sequester at physiological hematocrit concentrations (**Figure 6-3A**). As both PfEMP1-mediated cytoadhesion and mechanically stiffening through knob expression (K) may enhance sequestration, three isogenic EPCR-binding parasite variants with differing levels of knob and PfEMP1 expression were compared to normal red blood cells (Supplementary Figure 6-13). Fluorescently labeled IRBCs or RBCs were added to a 40% Hct RBC suspension to match

physiological parasitemia (2 – 4%)[86], then perfused through capillaries by gravity-driven flow. After 20 minutes, parasite sequestration at end-point was compared with flow modeling to relate expected flow properties with cytoadhesion and occlusion events (**Figure 6-3B**).

As expected, normal RBCs traversed the entire constriction vessel with minimal sequestration in any vessel region (**Figure 6-3Ci**, representative confocal image Supplementary Figure 6-15). Both labeled and unlabeled RBCs deformed as necessary to pass through the capillary, suggesting that the membrane-labelling procedure did not significantly increase sequestration potential. Next, we perfused IT4var19, a variant expressing both knobs and PfEMP1 ($K^+PfEMP1^+$) that is strongly cytoadhesive under static conditions[102]. Kinetic video analysis demonstrated sequestration in the post-capillary and capillary spaces with steady accumulation closer to the narrowest region. Complete occlusion of the capillary region could be observed within minutes after initiation of flow, followed by accumulation of IRBCs upstream of the blockage. At end-point, $K^+PfEMP1^+$ IRBCs demonstrated high levels of sequestration centered in the capillary region, extending into the post- and pre-capillary regions.

To elucidate the contributions of knobs and PfEMP1s, we trypsinized IT4var19 IRBCs to remove surface presentation of PfEMP1s while leaving knobs intact ($K^+PfEMP1^-$) (Supplementary Figure 6-14). Perfusion of $K^+PfEMP1^-$ IRBCs demonstrated minimal sequestration throughout the constriction vessel, with binding levels like that of normal RBCs and significantly lower than $K^+PfEMP1^-$ IRBCs in all vessel regions (**Figure 6-3**). Our findings suggest that while mechanical stiffening may contribute to IRBC margination toward the vessel wall in post-capillary regions[178], surface-active PfEMP1 is necessary to cause IRBC sequestration. Furthermore, despite the geometric confinement in capillaries, mechanical stiffening alone is insufficient to induce trapping in 5 – 10 μm capillaries. This finding is

consistent with previous microfluidic studies, which demonstrate mechanical trapping only in non-deformable channels below 4 μm in diameter[167]. While reduced IRBC deformability may impair flow through small vessels, it is possible that vessel dilation facilitates IRBC passage through small vessels. Stiffening likely contributes to splenic elimination, where interendothelial slits are as narrow as 3 μm[179], but knobs alone are not sufficient for sequestration in other peripheral capillaries.

As knobs are thought to enhance PfEMP1-mediated adhesion[93], we next perfused 2G2, a knobless strain expressing PfEMP1 ($K^-PfEMP1^+$). Although $K^-PfEMP1^+$ IRBCS are weakly cytoadhesive under static conditions and only partially stiffened as they lack knobs[94], moderate sequestration and partial occlusion was observed (**Fig. 3Cii**). Findings suggest that knobs are required for sequestration to extend into the capillary. Consistent with findings from with post-mortem autopsies[89], accumulation was focused at the post-capillary region (~3 fold increase as compared with pre-capillary regions). Although differences in pre- and post-capillary sequestration are thought to arise from arterial-venous differences in host receptor expression[180], we show IRBC sequestration localized to the post-capillary within vessels of a single cell type, suggesting this effect is partially geometry- and flow-dependent. While knobless IRBCs likely bind with lower affinity than knob-expressing IRBCs, the capillary geometry may nonetheless facilitate binding due to its high curvature and surface area to volume ratio, which increases contact area between IRBCs and endothelial cells.

C. Figures

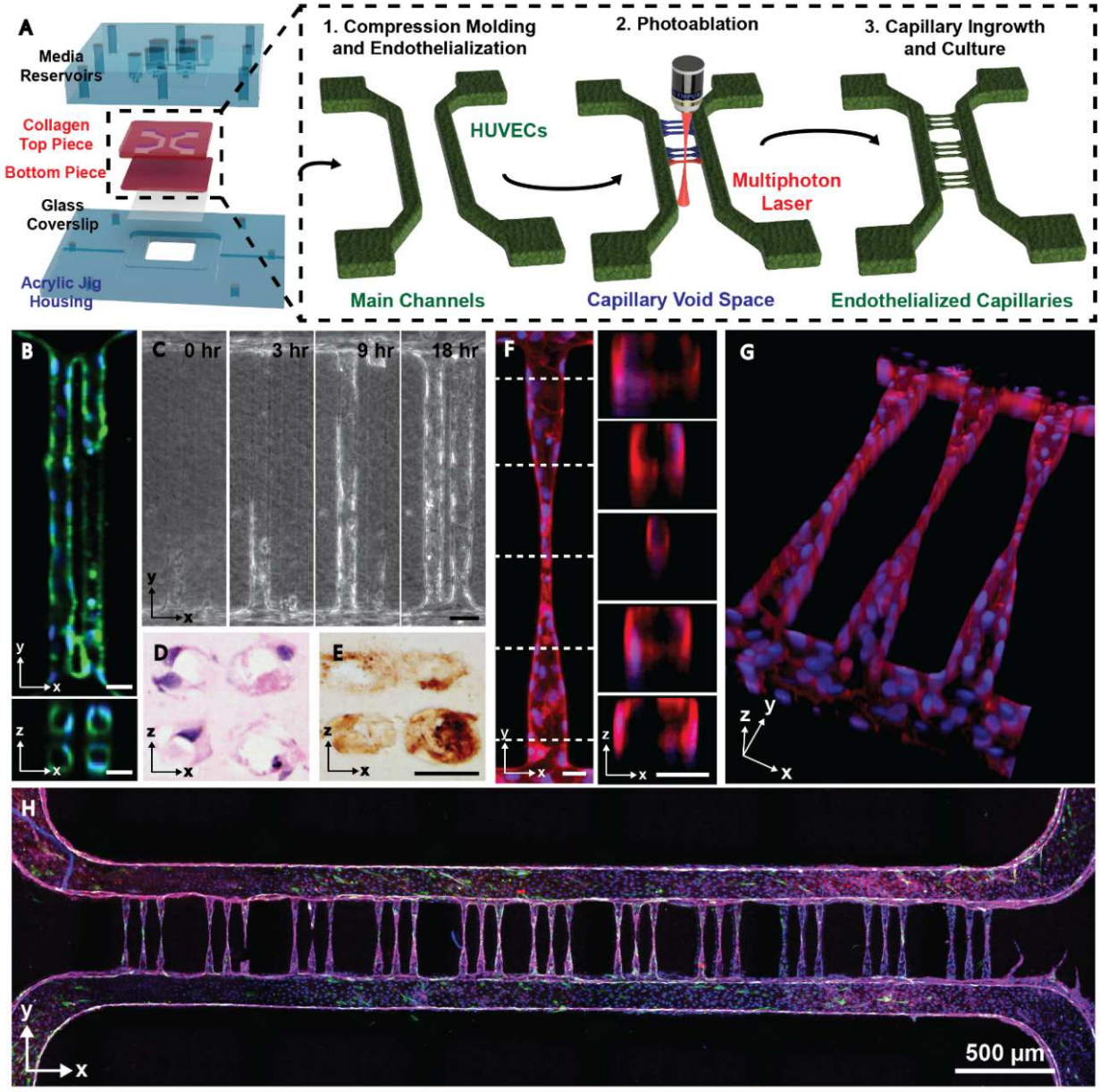

Figure 6-1: Fabrication of capillary networks in soft-lithography microvessel devices generated by photoablation.

A) Diagram of device assembly and capillary fabrication. Main channels were generated by soft-lithography in acrylic jigs followed by capillary generation by photoablation and endothelial ingrowth. **B)** 2 x 2 array of 20 µm diameter vessels demonstrate stable vessel lumens. **C)** Endothelial ingrowth over 18 hours demonstrates complete vessel formation. Cryosectioned capillaries were stained with **D)** H&E as well as **E)** type IV collagen demonstrating lumen formation by single endothelial cells and robust basement membrane deposition. **F-G)**

Constriction vessel design allows for the generation of sub 10 μm diameter capillaries shown both in cross-section and as a 3D render. **H)** Stitched confocal image demonstrates complete vessel network consisting of 33 capillaries. (Green: vWF, Blue: Nuclei, Red: VE-cadherin, Purple: F-actin, all scale bars = 25 μm unless otherwise specified)

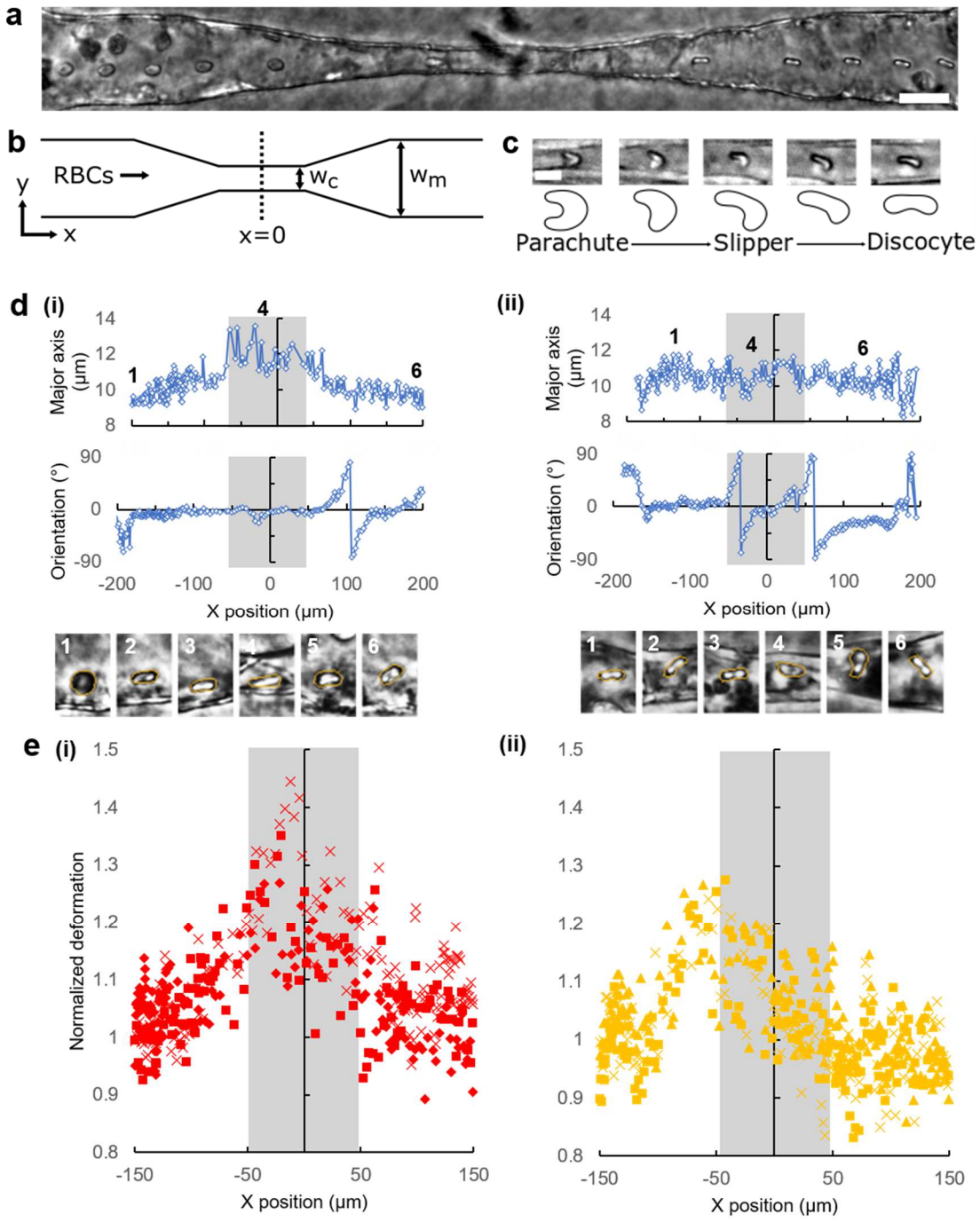

Figure 6-2: Motion and deformation of red blood cells in capillaries

A) Superimposed time lapse image series of RBC motion through an endothelialized vessel. Time lapse interval = 0.1 s; scale bar = 25 μm. **B)** Schematic showing RBC perfusion through

constriction-shaped vessel. w_c = 10 μm; w_m = 40 μm. **C)** Representative examples of parachute-like, slipper-like and complex deformations in constrictions. Scale bar = 10 μm. **D)** Trace of RBC major axis length and orientation for (i) stretching and (ii) tumbling red blood cells, where x = 0, y = 0 is the center of the capillary; grey box = capillary extents. 1-6 annotates images of RBC traversing vessel with edge detection shown in yellow **E)** Normalized extent of deformation for (i) normal red blood cells and (ii) knobless malaria-infected red blood cells demonstrate higher degrees of deformation in normal RBCs as compared with IRBCs. (n = 3, data points from individual trials are reported as x, ♦, ■)

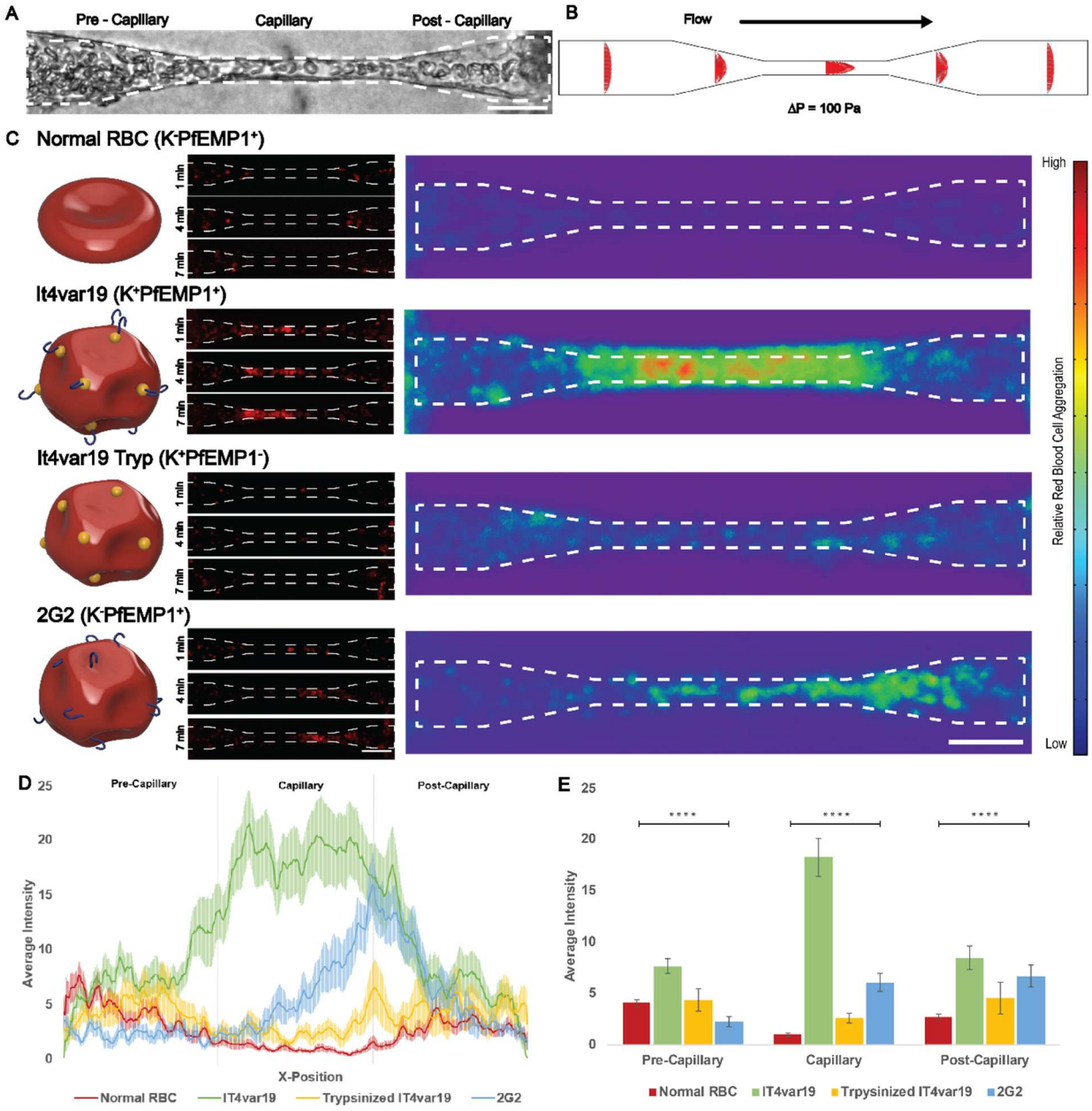

Figure 6-3: Population dynamics analysis of red blood cell flow and adherence within constriction capillaries.

A) Bright-field image of RBCs flowing through a constriction vessel. Dotted lines demonstrate capillary outline trace. B) Flow velocity model of a single capillary based on fabrication dimensions. C) Diagrammatic models of RBCs and IRBCs (Left) depicting RBC shape and constitution are followed by representative sequestration of RBCs within a capillary (Center). Image averaging of RBC sequestration after 20 mins is portrayed as a relative heatmap (Right). D) Quantification of average intensity as a measure of x-position as well as E) pre-capillary, capillary, and post-capillary regions. n = 24, 26, 17, and 19 for Normal RBC, IT4var19,

trypsinized IT4var19, and 2G2, respectively. ANOVA F= 11.61, P < .00001 for pre-capillary region, ANOVA F = 47.83, P < .00001 for capillary region, and ANOVA F = 6.41, P < .001 for post-capillary region.

D. Supplemental

1. Mammalian Cell Culture

Primary human umbilical vein endothelial cells (HUVECs) and human pulmonary artery endothelial cells (HPAECs) were cultured in endothelial growth media and used up to passage 7 (HUVECs: CC-2519, HPAECs: CC-2539, EGM: CC-3124 from Lonza). Primary human brain microvascular endothelial cells (HBMECs) (abcri 376; Cell Systems) were cultured according to manufacturer's recommendations in serum-containing CSC Complete media (4Z0-500; Cell Systems) with attachment factor as growth support (4Z0-210; Cell Systems). Brain endothelial cells were used up to passage 12.

2. Generation of Microvessel Network Silicon Wafer Master Mold

Channel network geometry was designed using computer-aided design software and fabricated using a standard photolithography process. Briefly, a silicon wafer was spin coated with SU-8 photoresist (Microchem), soft-baked at 65 ºC for 7 min, at 95 ºC for 1 hour, then cooled to 20 ºC. A negative chrome photomask was placed on the spin-coated wafer, and the wafer was exposed to UV light (λ = 365 nm), then baked at 65 ºC for 19 min, at 95 ºC for 1 hour, and cooled to 20 ºC. The exposed wafer was submerged in SU-8 developer, then cleaned with isopropyl alcohol and evaporation silanized overnight with trichloro(3,3,3-trifluoropropyl)silane (Sigma). Liquid PDMS (Dow Corning) was poured over the wafer pattern, cured at 65°C overnight, then peeled off the mold to generate a micropatterned stamp for vessel fabrication.

3. Microvessel Fabrication

Type I collagen was isolated from rat tails, lyophilized and resuspended to a stock concentration of 15 mg/ml in 0.1% acetic acid following a standard protocol[172], then diluted with cell culture media and neutralized to 7.5 mg/ml on ice before microvessel fabrication. Microvessels were fabricating using soft lithography and injection molding as previously described[73], which involves four major steps: (i) defining a micropatterned silicone stamp with parallel channel geometry, (ii) injecting collagen onto micropatterned stamp to form channel-patterned collagen gel and onto flat silicone stamp to form flat collagen gel, (iii) assembly by sealing patterned collagen gel onto flat collagen gel, (iv) seeding assembled channel with endothelial cells to create endothelialized collagen microvessel. The microvessels were cultured under gravity-driven flow for 3 – 7 days before multiphoton ablation.

4. Multiphoton Photoablation

Capillary fabrication was performed by multiphoton photoablation using a Mai Tai DeepSee Ti:S laser (maximum power 2.57W) coupled with an Olympus FV1000 MPE BX61 Microscope fitted with a water-immersion objective lens (25x, NA = 1.05). Vessel regions were first identified by second harmonic generation of collagen microfibers (λ_{ex} = 860 nm, $\lambda_{detector}$ = 420-460 nm). Individual capillaries were designed by designating 3D regions of interest using the Olympus Fluoview software then ablated by laser rastering (λ = 800 nm, I = 100%, pixel dwell time = 2 μs, 10-15 line repeat scans). Laser scanning in the X, Y, and Z dimensions were performed at ~1 μm step sizes. Cellular and collagen damage was confirmed by second harmonic generation of collagen microfibers. After fabrication, ablated vessels were cultured an additional 2 – 7 days to allow for endothelial ingrowth.

5. *Immunofluorescence Microscopy*

Microvessels were fixed *in situ* in 3.7% paraformaldehyde and washed with twice with PBS, then incubated in Background Buster (Innovex) for 30 minutes and blocking buffer (2% bovine serum albumin, 0.1% Triton-X in PBS) for 1 hour. Blocked microvessels were incubated overnight in primary antibodies (rabbit anti-VE-Cadherin, ab33168 from Abcam; FITC-conjugated sheep anti-VWF, ab8822 from Abcam) diluted in blocking buffer, washed, then incubated with secondary antibodies (goat anti-rabbit Alexa Fluor 568, A11031 from Invitrogen; goat anti-rabbit Alexa Fluor 647, A21244 from Invitrogen; and goat anti-mouse Alexa Fluor 647, A21235 from Invitrogen) for 1 hour. Stained microvessels were imaged using a Nikon A1R confocal microscope, and image stacks were acquired with a ~3 μm z-step distance between optical slices. Cross-sections and projections were produced from z-stacks using ImageJ software.

6. *Histological Analysis (Cryosectioning, H&E/ABC staining)*

Fixed microvessels were removed from their acrylic housing and equilibrated in OCT compound (Thermofisher) overnight at 4°C before transferring into fresh OCT and freezing in a 100% ethanol and dry ice slurry. Frozen blocks were sectioned at 10 μm thickness on a Leica CM1850 cryostat. Sections were stained with H&E, then viewed on a light microscope. Additional sections were stained for collagen IV by ABC immunoperoxidase method using an ABC-HRP kit (Vectorlabs), then developed with SIGMAFAST DAB (Sigma-Aldrich).

7. RBC Isolation

Normal red blood cells were isolated from whole blood by centrifugation on a Ficoll-Paque (Sigma-Aldrich; specific gravity = 1.077 g/mL) gradient at 1500 rpm for 20 minutes. The platelet-rich plasma and buffy coat were aspirated, and the packed RBC volume was washed three times in Dulbecco's phosphate buffered saline solution (DPBS) buffer. Purity of the RBC preparation was assessed with a thick blood smear, which was fixed in 100% methanol, stained with 1x Field's stain and visualized at 40X to confirm absence of white blood cells.

8. Parasite Culture

P. falciparum parasite lines were cultured under standard conditions[181], using anonymized human O+ type red blood cells (Valley Biomedical) in RPMI-1640 (Gibco) supplemented with 10% human type A+ serum in a gas mixture of 90% N_2, 5% CO_2 and 5% O_2. Both lines predominantly express a single *var* gene and were derived from the IT4/FCR3 parasite genotype. The knobless parasite line 2G2 was derived by limited dilution cloning[181], while the IT4var19 line was generated after repeatedly panning on transformed human brain microvascular endothelial cells (THBMEC) followed by limited clonal dilution[182]. Mature-stage infected red blood cells were enriched to 60-90% parasitemia by magnetic separation (MACS Cell Separator, LD columns, Miltenyi Biotech) prior to capillary perfusion for single cell and population dynamics experiments.

9. Determination of var Transcription by qRT-PCR.

Because *var* gene expression switches over time, the *var* transcription profile of the parasite lines was regularly monitored by qRT-PCR with a specific set of primers specific to the

IT4 *var* gene repertoire[99]. RNA was obtained from synchronized ring parasites (8-12h post-invasion), extracted in Trizol LS (Invitrogen) and reversed transcribed using random hexamers and MultiScribe reverse transcriptase (Thermo Fisher). qRT-PCR reactions were performed using Power-SYBR green Master Mix (Thermo Fisher) in an ABI Prism 7500 Thermal Cycler following published amplification conditions[99]. Relative transcription of *var* genes was determined by normalization to the control housekeeping gene seryl-tRNA-synthetase (STS; PF07_0073) and the level of expression was represented as transcript units (TU) and calculated as $TU=2^{(-\Delta CT)}$.

10. Single-cell Dynamics Experiments

Enriched mature stage *P. falciparum*-IRBC or packed red blood cells were resuspended in serum-containing EGM at $5x10^6$ cells/mL, allowing visualization of individual cells. The dilute cell suspension was perfused through individual capillaries at different hydraulic gradients by gravity-driven flow. Motion of individual red blood cells was visualized with a Nikon TiE inverted widefield microscope, and videos were acquired at 20x and 250-500 frames per second using an Orca-Flash4.0 V2 Digital CMOS camera (Hamamatsu).

11. Single-cell Dynamics Data Analysis

After acquisition, videos were analyzed using custom MATLAB scripts. Briefly, individual frames containing red blood cells were smoothed using a Wiener filter, inverted, then background subtracted using a mean filter. Red blood cells were detected using Canny's method. Small gaps in red blood cell outlines were closed automatically using an edge-linking algorithm[183] or manually. Individual red blood cell outlines were linked into trajectories based

on displacement between outlines in different frames[184]. Out-of-focus and overlapping red blood cells were excluded from analysis.

12. Population Dynamics Experiments

Enriched mature stage *P.* falciparum-IRBC or packed red blood cells were fluorescently labeled according to the PKH26 Red Fluorescent Cell Linker Kit (Sigma-Aldrich). To simulate blood with physiological parasitemia[86], labeled cells were added to normal, unlabeled red blood cells at a concentration of 1 – 4% (vol/vol), then diluted to 40% hematocrit in serum-containing EGM. RBCS were encouraged to flow across the device using an approximately 100 Pa pressure drop for 20 minutes. Location and extent of binding was determined by fluorescence microscopy after 1, 4, 7 and 20 minutes of perfusion.

13. Trypsin Treatment and Flow Cytometry Analysis.

IT4var19 Trophozoite-stage enriched IRBC were treated with a 66.67µg/ml trypsin (Sigma-Aldrich) solution in PBS for 30 min at 37ºC, followed by an inhibition in an equal volume of FBS. To determine were incubated for 30 min at 4°C with a 1:10 dilution malaria hyperimmune serum from Kenya. Antibody labeling was detected with goat anti-human IgG-Alexa 488 (Molecular Probes) at a 1:400 dilution for 30 min. Infected erythrocyte nuclei were detected with ethidium bromide (Invitrogen) at a 1:500 dilution added with the secondary antibody. Stained cells were washed in phosphate-buffered saline (PBS) and analyzed on an LSRII fluorescence-activated cell sorter (FACS) machine (BD Biosciences). Analysis was performed using FlowJo 8 (Tree Star, Inc., Ashland, OR).

14. Population Dynamics Data Analysis

Quantification of population dynamics was performed on fluorescent images taken after 20 minutes of perfusion. Images were normalized between average background values and peak fluorescent intensity values and a 2-pixel radius median filter was used to remove speckle noise using MATLAB. Masks were manually drawn to outline individual capillaries using ImageJ. Average fluorescent intensity was calculated at each x-position as the sum of intensity values across the y-dimension divided by the diameter of the capillary at this position. The central point of each capillary was determined, and the average intensity maps were lined up across all images at this central point. Intensity groupings into pre-capillary, capillary, and post-capillary regions was done by dividing each intensity map into even thirds.

15. Numerical Simulation

Flow characteristics of individual constriction-shaped capillaries were estimated using COMSOL Multiphysics software, package version 5.1. As IRBC perfusion occurred at relatively slow flow velocity in small-diameter microvessels, flow through the capillary was assumed to be laminar, and the stationary solver for laminar flow was used with pre-defined Navier-Stokes equations. Flow was assumed Newtonian and IRBC suspension was assumed to have similar fluid properties to water (viscosity of 10^{-3} Pa s and density of 10^{3} kg/m3) due to the low hematocrit used during perfusion. Inlet boundary conditions were defined for the perfusion pressure 100 Pa, and the outlet boundary conditions were set at zero pressure. Flow velocity, pressure and shear stress were imported into MATLAB 2017a via LiveLink.

16. CAD Design of Silicon Wafer

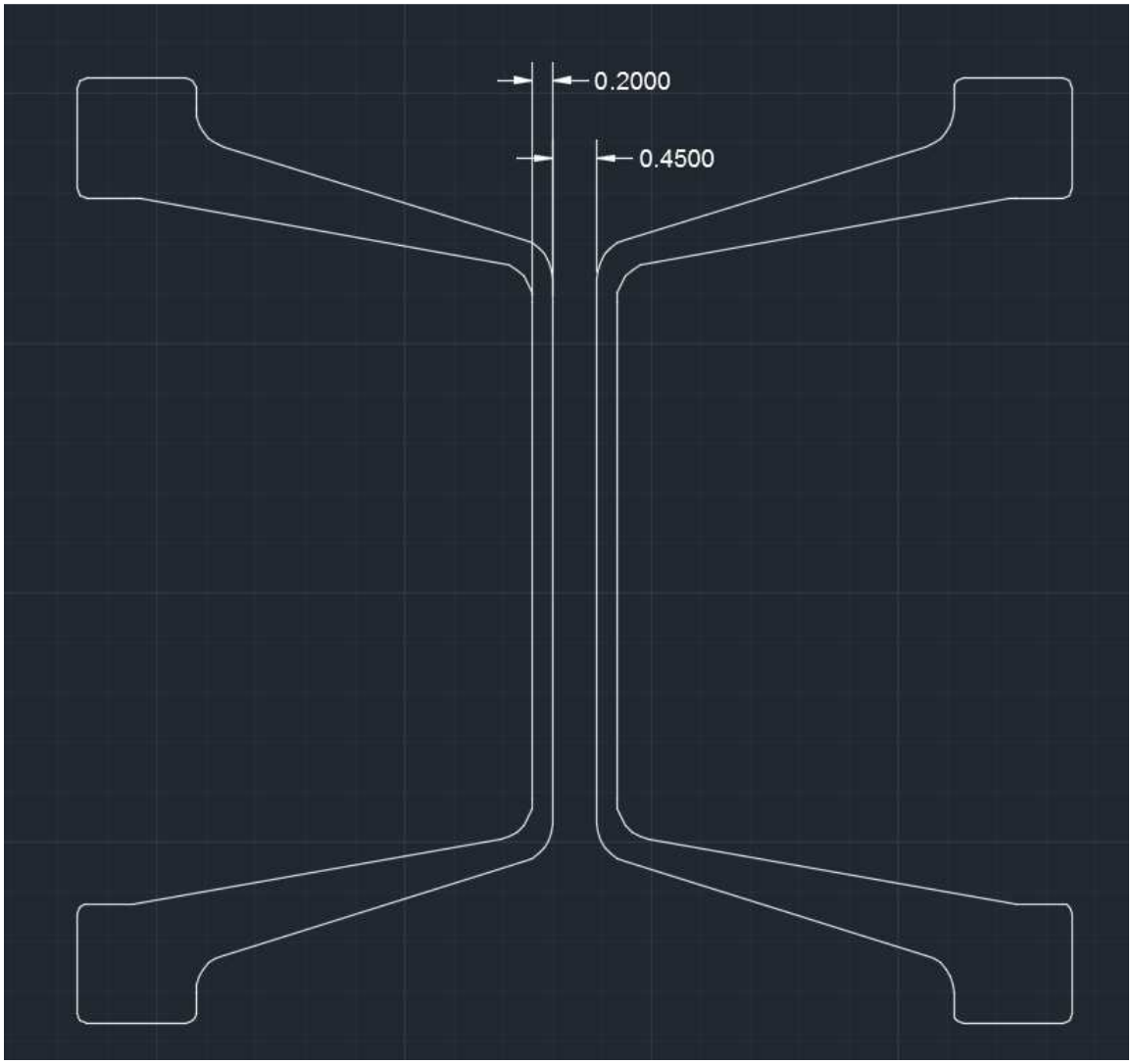

Figure 6-4: Design of silicon wafer using CAD software

A silicon wafer master mold was utilized to generate PDMS soft lithography stamps. Main channel design consisted of two parallel and identical vessels (200 µm x 200 µm, in cross-section) spaced 450 µm apart. Vessels were designed with two inlets and two outlets.

17. Photoablation Fabrication Limitations

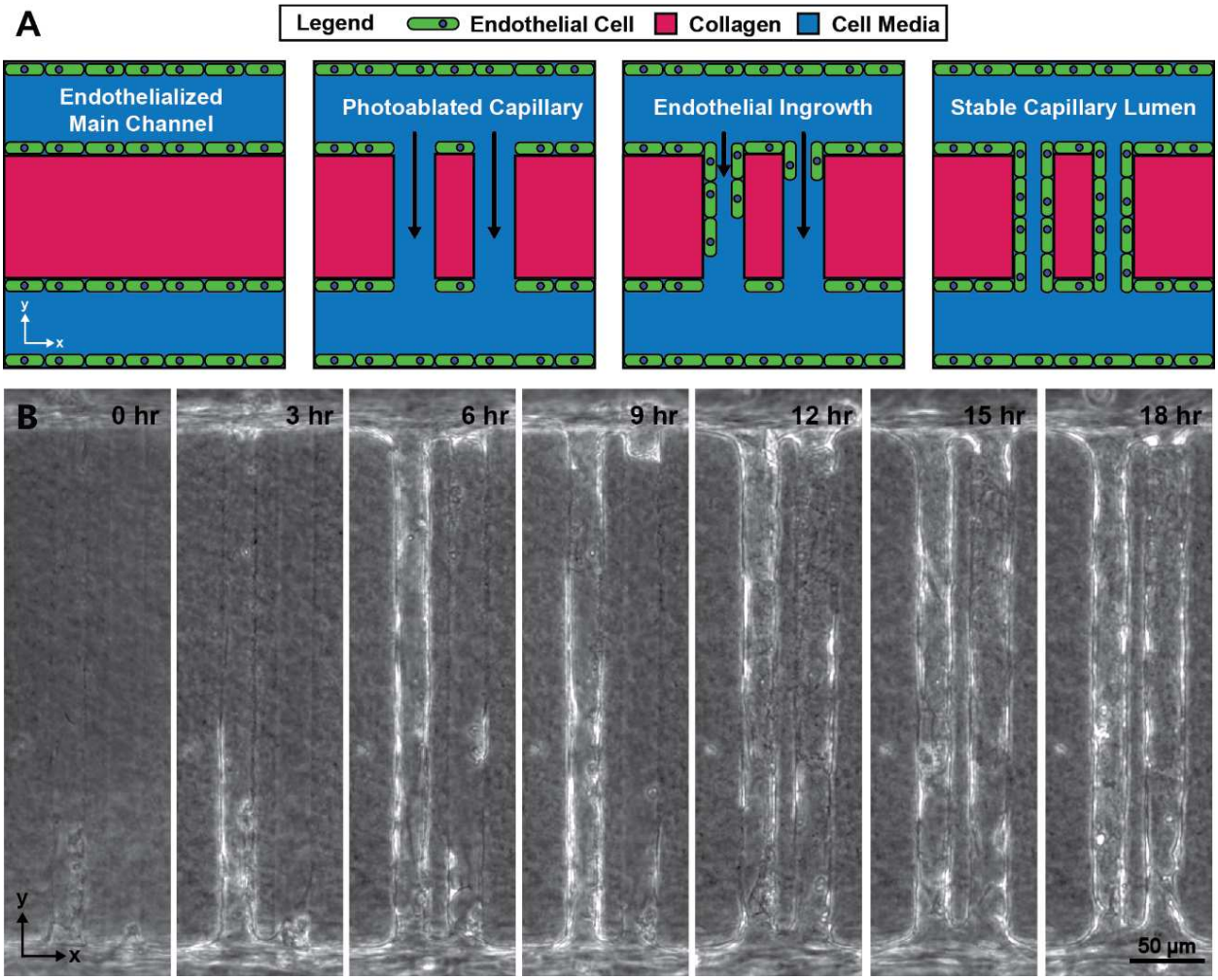

Figure 6-5: Endothelial ingrowth into capillary networks

To determine the time scale over which endothelial cells were able to populate photoablated capillaries, straight channel capillaries were generated and then imaged using phase-contrast live imaging. **A)** Schematic diagram demonstrates vessel damage giving rise to endothelial ingrowth. **B)** Endothelial cells readily populate two 20 µm channels spaced 20 µm apart over an 18-hour growth period.

18. *Collagen Photoablation Confirmed through Imaging of Collagen Second Harmonic Generation Imaging*

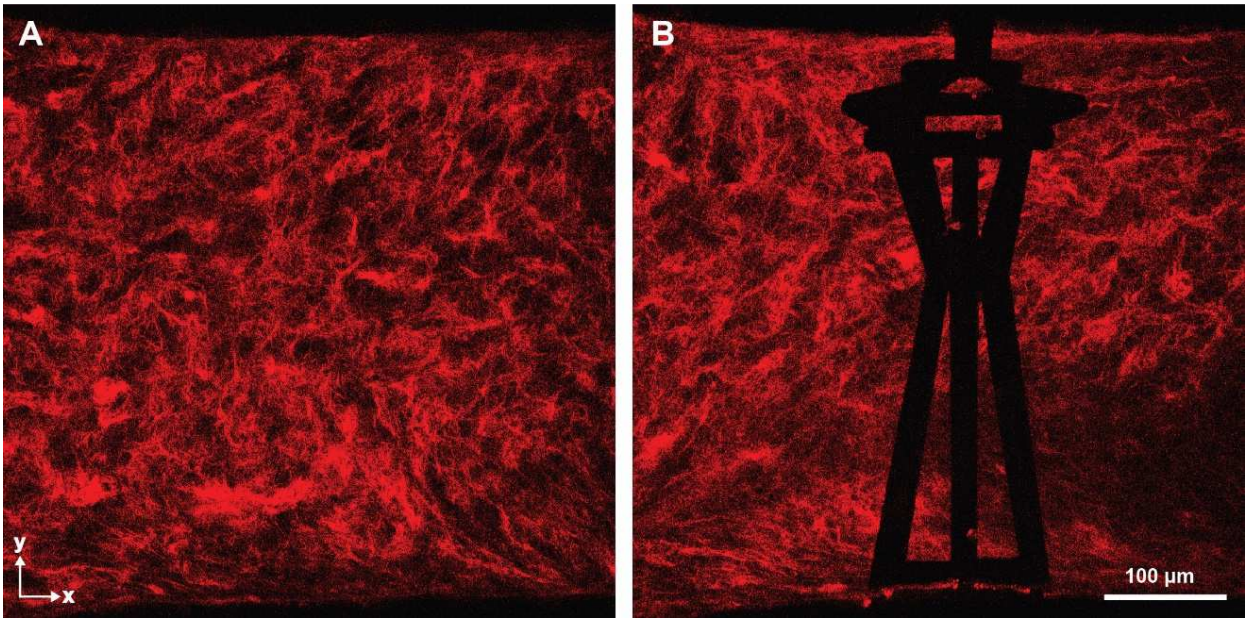

Figure 6-6: Collagen photoablation confirmed through imaging of collagen second harmonic generation

To confirm void space generation following photoablation, second harmonic generation was used to visualize collagen fibrils A) before and B) after fabrication (red = collagen). Here, a vessel design of the Seattle Space Needle was generated using photoablation.

19. Photoablated Capillary Fabrication Limitations

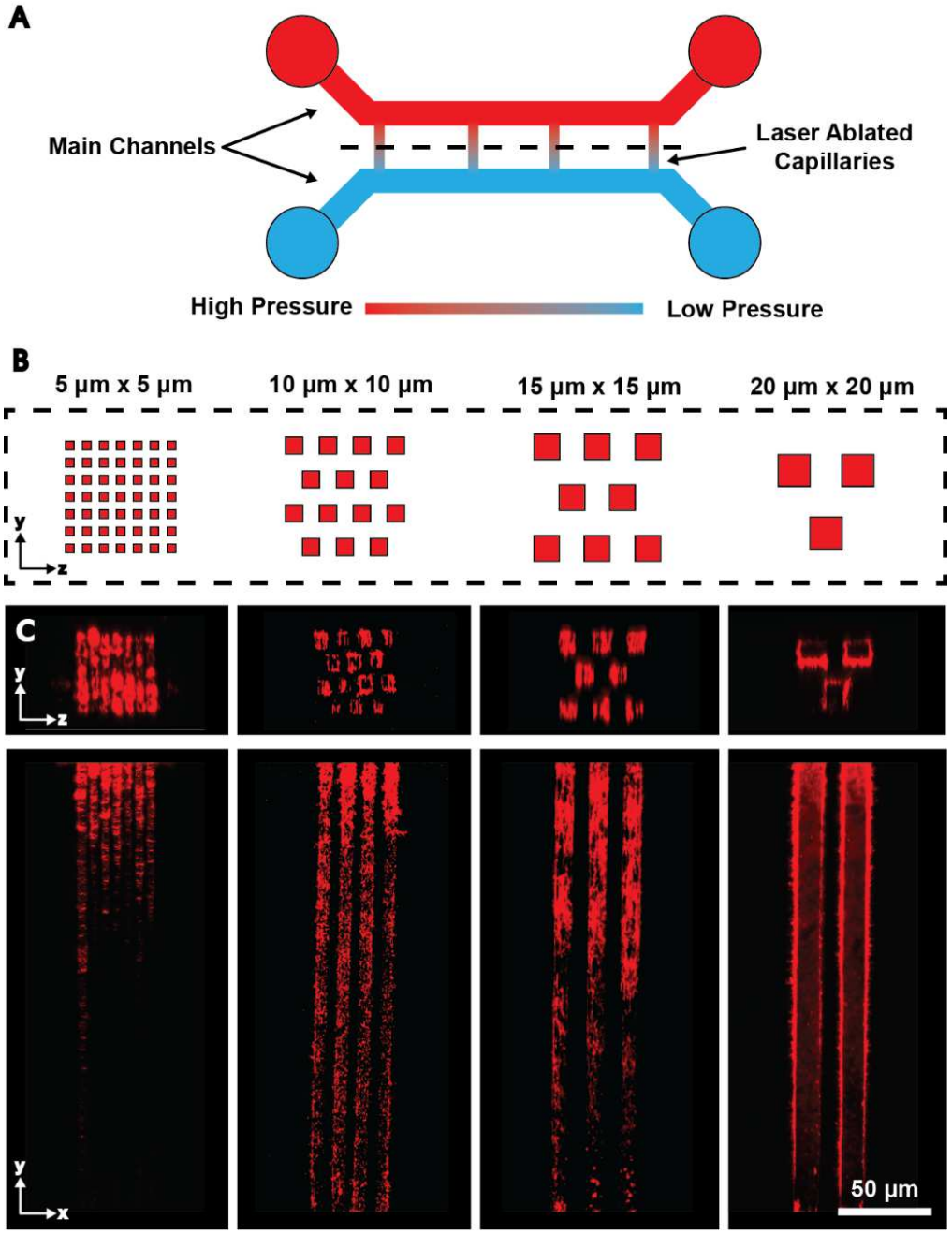

Figure 6-7: Photoablated capillary fabrication limitations

To determine fabrication limitations of photoablation within microvessel devices, acellular devices were subjected to photoablation and perfused with red fluorescent beads (d = 0.22 µm). Schematic representations demonstrate A) direction of perfusion and B) cross-section of ablated channels. Vessels ranged from 5 µm x 5 µm to 20 µm x 20 µm, where spacing and cross-sectional dimensions were made equal in size. (Red = fluorescent beads)

20. Cellular Limitations of Capillary Fabrication

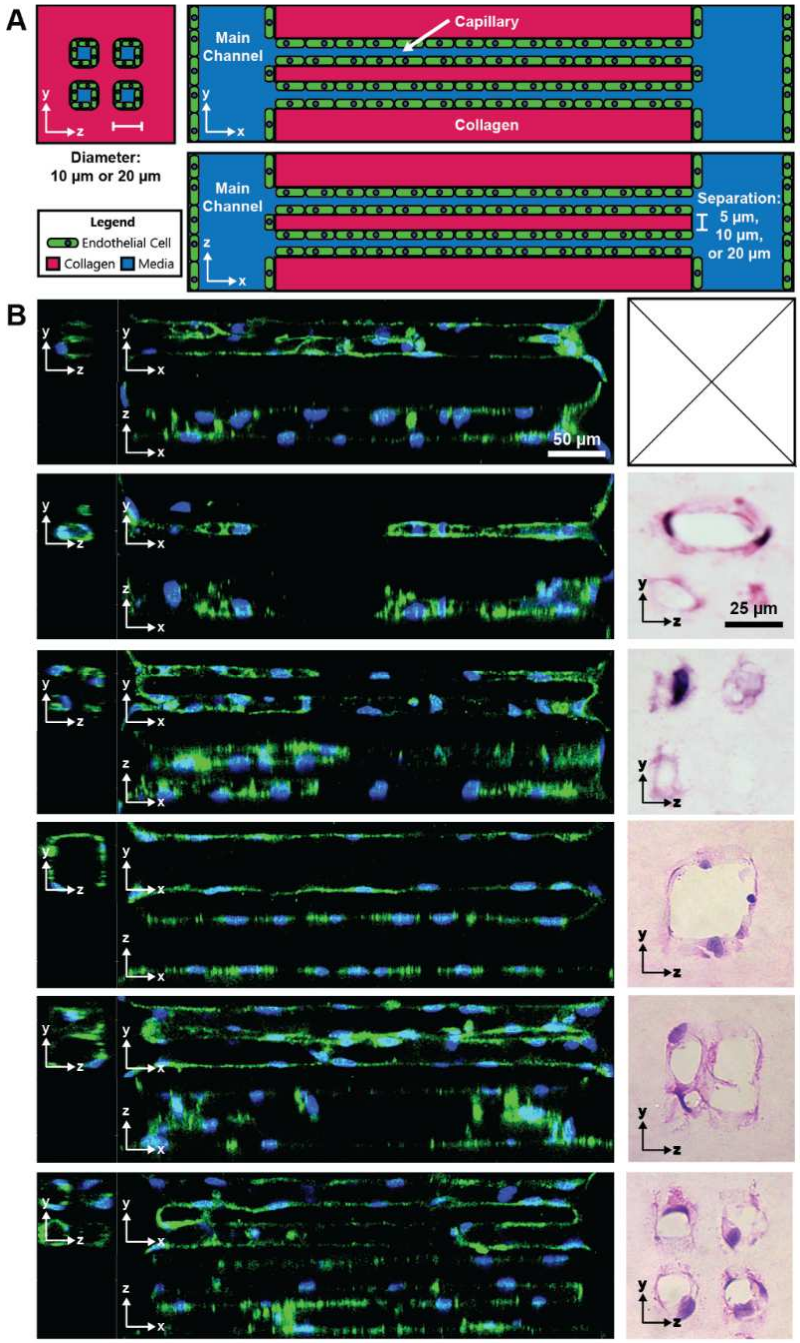

Figure 6-8: Cellular limitations of capillary fabrication

As endothelial cells readily remodel their surrounding matrix, experiments were conducted to determine the size and density limitations of capillary generation over a 7-day time period. Straight channel capillaries were generated, cultured for 7 days and then imaged by confocal microscopy. **A)** Diagrammatic cross-sections represent intended vessel design. **B)** 2x2 arrays of

either 10 μm or 20 μm diameter vessels (right panel) were generated using photoablation joining the two main channels together. Vessels were separated by either 5, 10, or 20 μm, cultured for 7 days, fixed, stained, and imaged by confocal microscopy (blue = nuclei, green = vWF). C) H&E stained cryosections demonstrate that endothelial cells remodel the vessels from square to circular lumens.

21. Stable Vessel Length is Diameter Dependent

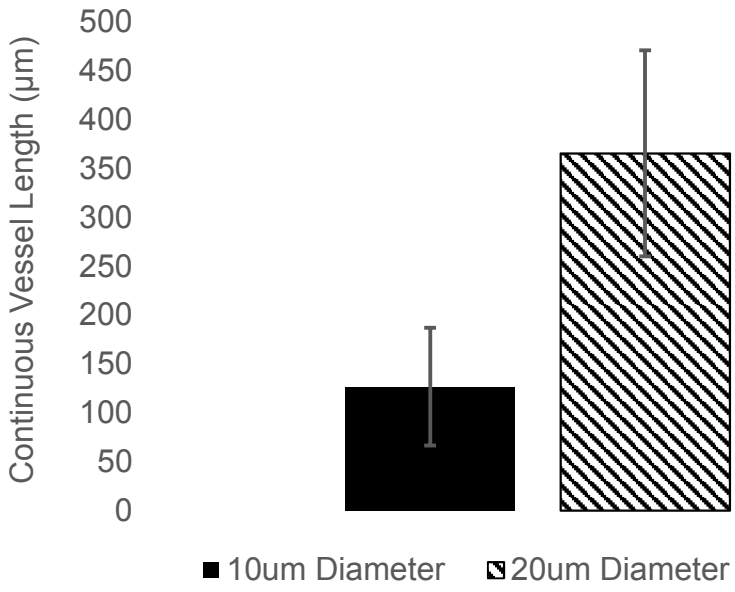

Figure 6-9: Stable vessel length depends on vessel diameter

10 µm and 20 µm diameter vessels were generated by photoablation spanning 450 µm in length. Vessels were then imaged by confocal microscopy to determine average stable vessel. Statistically significant differences between continuous vessel length was observed ($p=7.85*10^{-6}$ <0.05, two-tailed t-test of unequal variance)

22. Equal Wall Shear Stress Vessel Design

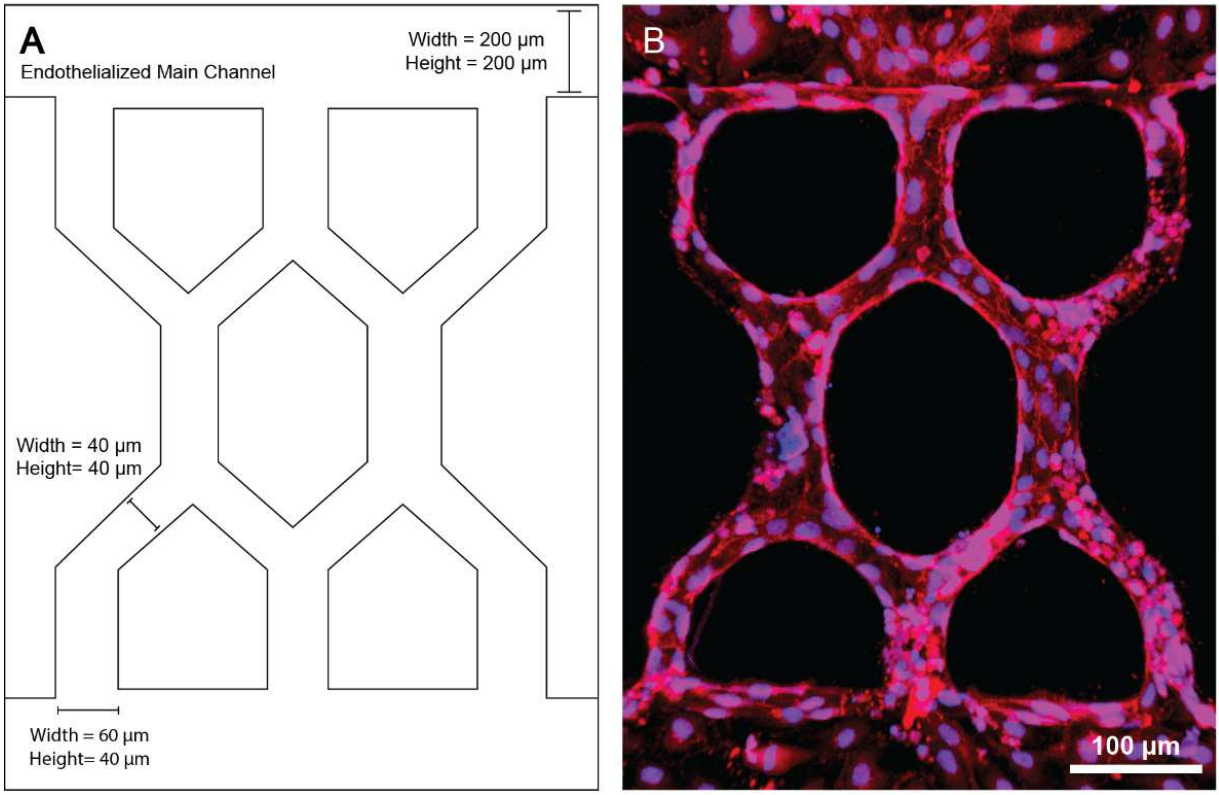

Figure 6-10: Equal wall shear stress vessel design

As vessel fabrication is completely user-defined, we sought to generate vessel networks that demonstrate hierarchical branching with equal wall shear stress through each vessel branch. Networks consisted of alternating 60 µm and 40 µm diameter vessels connecting the main channels. A) A schematic representation of the intended vessel design is demonstrated. B) Confocal imaging of an endothelialized equal wall shear stress vessel after 7 days of culture under gravity driven flow. (red = VE-cadherin, blue = nuclei)

23. Sprouting

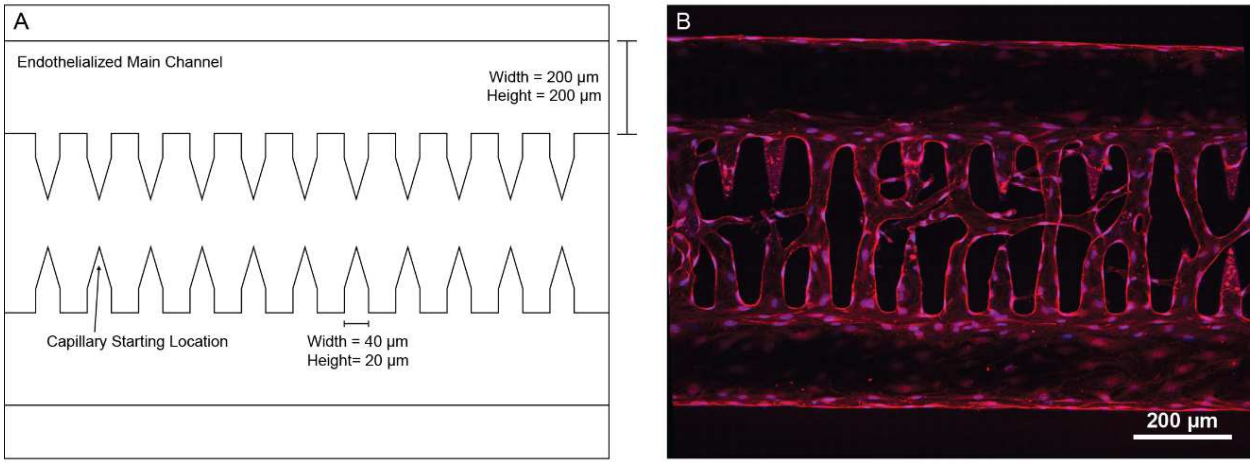

Figure 6-11: Sprouting

As angiogenic models have been proposed to generate interconnected capillary networks, we attempted to recreate an angiogenic capillary sprouting. Rather than completely anastomosing endothelialized main channels, tooth-like void space protrusions from the main channel were generated using multiphoton photoablation. Devices were subsequently cultured for 3 days in angiogenic media consisting of endothelial growth media supplemented with 50 ng/ml PMA (phorbol myristate acetate) and 40 ng/ml VEGF (vascular endothelial growth factor). Resulting sprouts demonstrate directed but uncontrolled and large sprouts (diameter = 36.96 +/- 15.51 µm, red = VE-cadherin, blue = nuclei).

24. Single Cell Image Processing Edge Detection Workflow

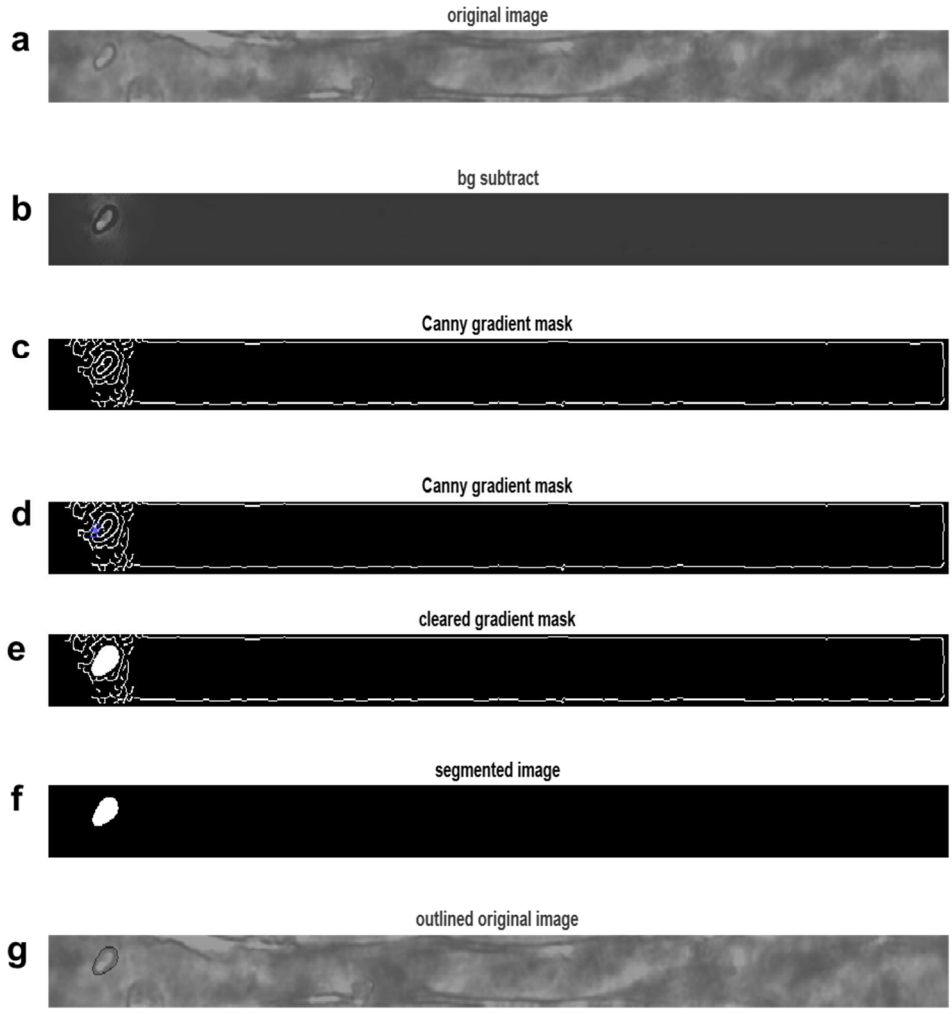

Figure 6-12: Edge detection workflow

To track red blood cells traversing the capillary vessels, an edge detection-based algorithm was implemented. A) A single frame from a brightfield video was B) background subtracted using the mean of all frames, then C) edge detected. The edge detection result was D) manually edited to close the contour, E) filled and F) eroded to yield G) a contour outlining the red blood cell.

25. qPCR of var Gene Expression by 2G2 and IT4var19

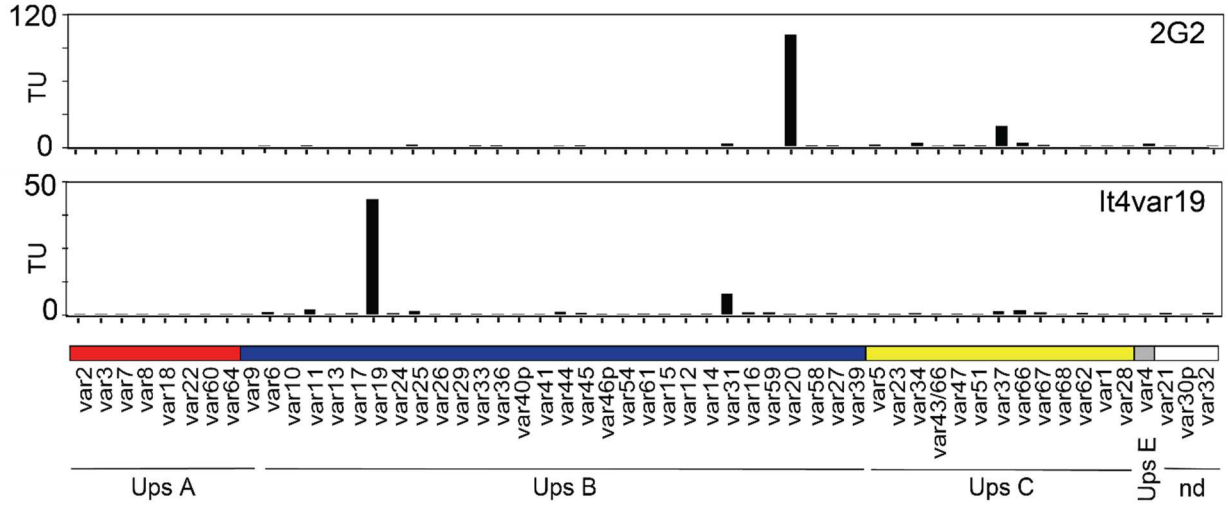

Figure 6-13: qPCR of var gene expression by parasite strains

Quantitative PCR was performed on MACS purified parasite strains 2G2 and IT4var19 to determine relative expression and purity of var gene expression. Gene expression analysis demonstrates relatively pure expression of var 20 and var 19, respectively indicating nearly pure populations of the intended parasite strains and PfEMP1 expression as expected.

26. Flow Cytometry of IT4var19 IRBCs Before and After Trypsinization

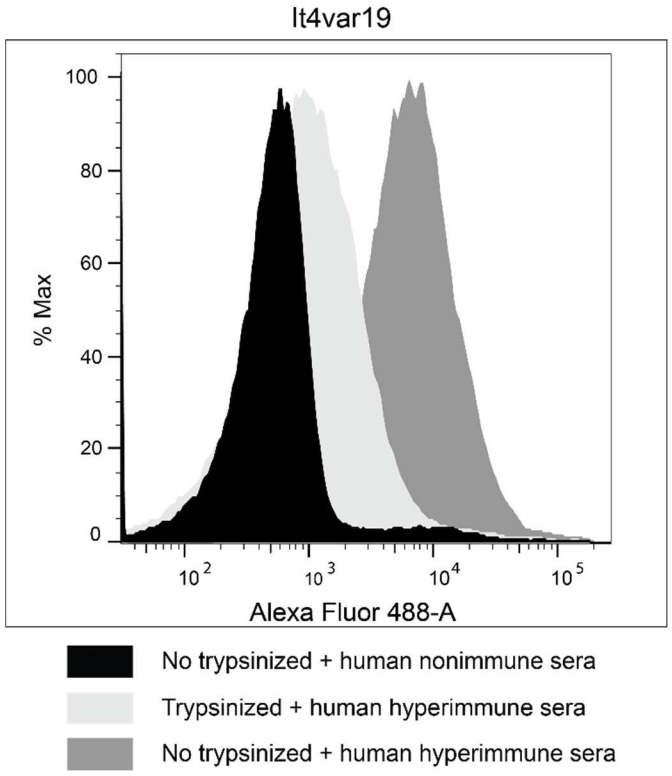

Figure 6-14: Flow cytometry of IT4var19 parasite infected RBCs before and after trypsinization

Flow cytometry was performed on trypsinized and non-trypsinized IT4var19 IRBCs using patient human derived sera against PfEMP1. Findings were compared with non-trypsinized IT4var19 IRBCs treated with nonimmune human sera. Findings demonstrate clear reduction in var19 PfEMP1 surface expression after trypsinization.

27. Representative Confocal Image of RBC Sequestration in Capillary

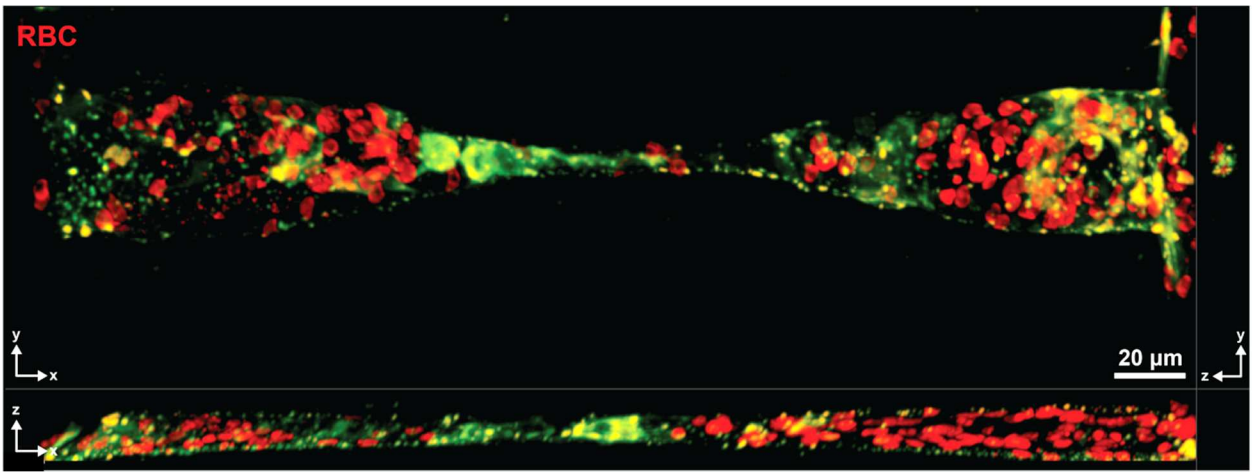

Figure 6-15: 3D confocal image of RBC sequestration in a synthetic capillary

After a population flow experiment, a single IT4var19 IRBC perfused capillary was selected for post-analysis imaging by confocal microscopy. Vessel device containing sequestered capillaries was washed with PBS, fixed and subsequently imaged. 3D rendering using IMARS image processing software demonstrates the capacity to view sequestered IRBCS within synthetic capillaries after fixation.

CHAPTER 7: CONCLUSIONS AND FUTURE DIRECTIONS

A. Conclusion

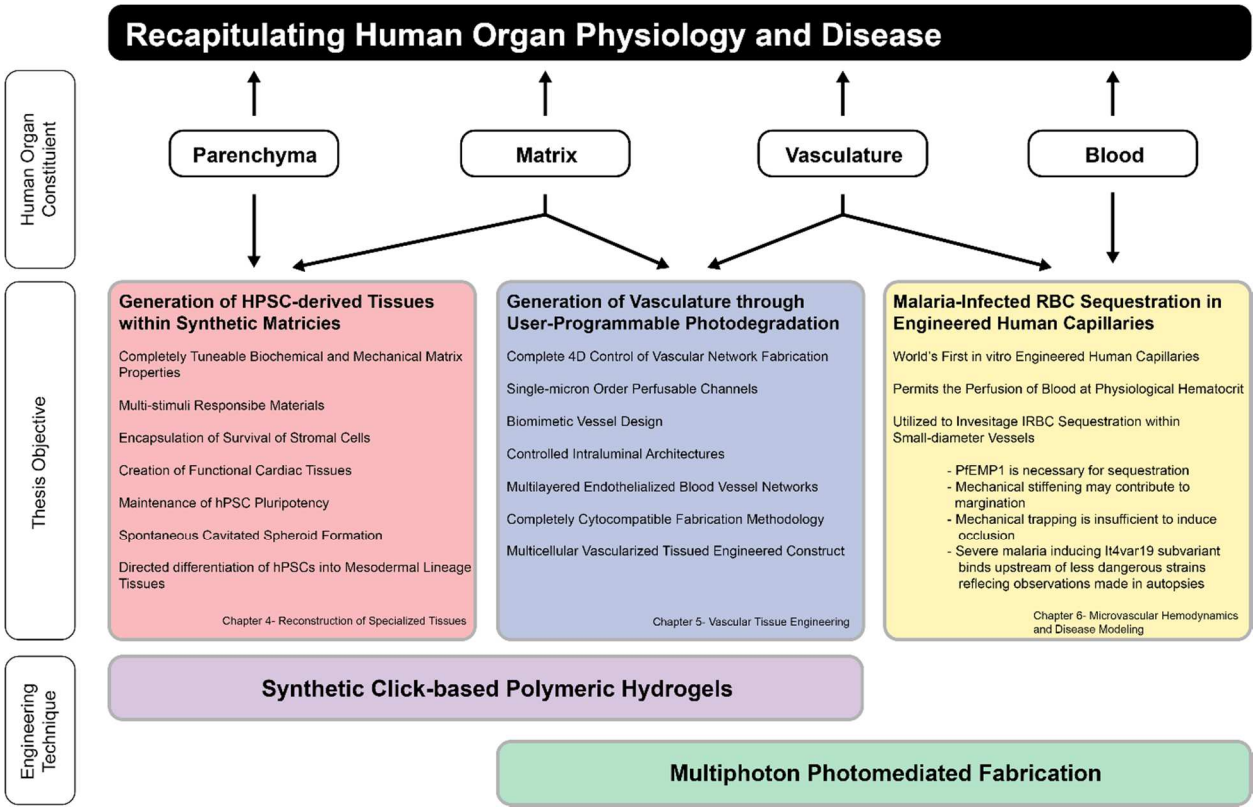

Figure 7-1: 4D Control of tissue development and vasculature using photo-mediated chemistries thesis organization

This thesis utilized a combination of synthetic click-based polymeric hydrogels and multiphoton photomediated fabrication techniques to recapitulate the dynamic interactions between parenchyma, matrix, vasculature, and blood to better understand and study human organ physiology and disease.

From cells to tissues, tissues to organs, and organs to organisms, there exists a hierarchy of life with increasing complexity at each stage. Through efforts in tissue engineering, stem cell biology, and regenerative medicine, we are now just beginning to understand those factors which

govern the mechanics and machinery of cells and specialized tissues. We and others have shown that directed differentiation of hPSCs can give rise to specific cell types and even self-organizing organoids, suggesting that stem cells can one day be used to replace damaged organs and better understand disease. However, to apply these cells to construct higher-order tissues requires more than any one differentiated cell type. Organs consist of cells, matrix, vasculature and blood constructed in a conserved architecture to permit organ function and maximize efficiency. In this body of work, we address these hurdles in tissue engineering by developing novel biomaterials and fabrication techniques to construct functional tissues with engineered vasculature that permit blood perfusion (**Figure 7-1**).

We began by exploring those factors necessary to construct specialized tissues using synthetic 3D hydrogel platforms. In Chapter 4, we first optimized material, cellular, and chemical conditions to support the culture and generation of mature cardiac tissues. Building off the successes of others in our lab, we chose to utilize a two component SPAAC-based hydrogel network consisting of a 20 kDa PEG tetra-BCN[19,124] and a synthetic diazide functionalized, MMP-cleavable peptide sequence[117]. To allow for cell attachment and to encourage cells to grow and migrate through our hydrogels, RGDS-azide peptides were synthesized and implemented. Next, we confirmed our hydrogels could be remodeled by encapsulating several stromal cell lines. hS5 cells were ultimately utilized for their ability to degrade and compact our synthetic matrices. Cardiomyocytes were then produced using an established differentiation protocol, co-encapsulated with hS5s and cultured for 7 weeks. Mirroring findings in natural-based materials[123], our hydrogels supported cardiomyocyte culture, allowed for tissue compaction, and resulted in functional contractile cardiac tissues. Findings here validate that our

platform could be used interchangeably with natural based materials, granting users access to all future material developments made in our laboratory.

Encouraged by our successes to generate mature cardiac tissues, we then attempted to recapitulate the embryonic stem cell niche by using our tunable PEG hydrogels to better understand the dynamics between hPSC culture and their microenvironment. As material components can be added or removed on cue, our hydrogels were able to serve as a blank slate upon which individual soluble and matrix factors could be probed. Again, material and cellular properties were optimized. Softer 5 wt% hydrogels were utilized and no RGDS was incorporated, so as to minimize the influence of the hydrogel network on differentiation. Encapsulation of both hiPSCs and hESCs were extremely successful, not only demonstrating high viability of hPSCs in 3D but also maintaining complete pluripotency. Upon extended culture, hPSCs readily degraded the hydrogel matrix and demonstrated a cavitated spheroid-like morphology, noted as a critical step in the differentiation of kidney organoids[55]. Next, by modifying existing differentiation protocols, exclusive manipulation of canonical Wnt activation and inactivation at defined periods was used to successfully direct the differentiation of both hiPSCs and hESCs into mesoderm lineage cell types. Cardiomyocyte colonies could be observed beating throughout the hydrogel, initially as small colonies followed by subsequent coalescence. Here we expanded our application of our PEG matrices to not only support differentiated cells but also better understand the 3D and matrix-associated factors which govern mesodermal differentiation.

As these and all tissues necessitate the delivery of oxygen and nutrients to survive and function, in Chapter 5, a photodegradation based vascular fabrication technique was developed[125]. By using a combination of multiphoton microscopy in conjunction with novel

photodegradable biomaterials, users can generate free-form vasculature within cell-laden hydrogels with complete spatiotemporal control. Leveraging multiphoton photodegradation, we created some of the smallest perfusable microfluidic channels to date, pushing the limitations of vascular fabrication while simultaneously demonstrating that channels could be made with complete 3D control and evolve with time. As this process is fully programmable and as void space generation is completely user-defined, complex fluidic devices were created including ones with unique intraluminal geometries. We then proved that our multiphoton photodegradation methodology was completely cytocompatible by generating endothelialized hierarchical vasculature within stromal cell-laden hydrogels. These higher-order tissues demonstrate not only a capacity to generate multicellular tissue engineered constructs, but also establish a methodology to create user-designed vasculature to study the interactions between vessels and parenchyma.

Expanding our photodegradation technique to non-degradable materials and to better understand the interactions between blood and vasculature, in Chapter 6, we then set out to create the world's first engineered *in vitro* human capillaries. By combining multiphoton photoablation with soft-lithography injection molding of collagen[71], we created perfusable endothelialized microvascular devices. In this work, we determined the engineering constraints which govern small vessel stability and successfully created the smallest endothelialized blood vessels to date. These sub-10 μm capillary networks were generated with complete 4D control, endothelialized within 24 hours, exhibited robust junctional staining, and remained stable for up to two weeks in culture.

As sequestration of infected erythrocytes in capillary-sized vessels is a hallmark of severe malaria and as there are currently no *in vivo* models of human infection, we then implemented

our capillary devices to understand the hemodynamic interactions between malaria-infected blood and small-diameter vasculature. We first perfused low hematocrit knobless parasites and normal RBCs and imaged individual cells as they traversed through our capillary networks. Analysis by a custom MATLAB script revealed marked differences in elongation and percent tumbling, with potential margination. To then assess the individual contributions of mechanical stiffening resulting from knob expression and PfEMP1-mediated cytoadhesion to sequestration, blood of physiological hematocrits with parasitemia reflective of infection were perfused through our devices. In the very first model of IRBC sequestration in a human *in vitro* capillary model, we demonstrate a unique binding phenomenon very similar to post-mortem analysis with sequestration observed in the capillary and post-capillary venule. Comparison of highly cytoadhesive/knob-expressing, knobless, and PfEMP1-cleaved IRBCs with normal RBCs revealed knob-associated contributions to cytoadhesion, a lack of mechanically trapping, and necessity of PfEMP1 to sequestration. Together this data identifies factors which can be targeted for anti-malaria therapy and more broadly provides a first look at the application of our capillary devices to answer biological questions which could otherwise only be observed in a human model.

In summary, this thesis demonstrates the capacity to create complex higher-order multicellular tissues with controlled vasculature that can be perfused with blood. While generating vascularized tissues has become a cornerstone of tissue engineering[63], work here highlights the key aspects of light-based techniques, focusing on the free-form nature of fabrication, sub-micron resolution, site-specific chemical degradation, and user-programmability. In comparison with 3D bioprinting[64–66], vasculature generated using sacrificial polysaccharide-based wires[67,70], and even soft-lithography injection molding, light-based chemistries remain

one of the few potential means to generate complex 3D vascular channels with single-micron resolution[143]. Using photodegradation and photoablation to generate void spaces, we gain the ability to create user-defined geometries inside biomaterials with complete 4D control. Taking advantage of this photoresponsive property, we are able to generate microvascular patterns one to two orders of magnitude greater in resolution than 3D printing (near single-micron resolution[19,119]) within synthetic and natural biomaterials using cytocompatible photochemistries[185].

B. Future Directions

Successes in each of these material and fabrication technologies encourage future explorations in tissue engineering, malaria biology and hematologic disease. Both short-term and long-term directions are suggested.

1. Cardiac Tissue Engineering

Preliminary data from Chapter 4 indicates that cardiac tissues can be generated within PEG hydrogels and that material properties can be optimized for both cell remodeling and tissue function. While we and others have explored three-dimensional cardiac tissue-engineered constructs, major challenges concerning vascularization and recapitulation of the complex double-helical muscle fiber organization have yet to be addressed. Current constructs are limited in size due to an inability to support the high metabolic demand of cardiomyocytes and exhibit suboptimal tissue contraction and electrical wave propagation due to inadequate control over cardiomyocyte organization and orientation[186,187]. The most important challenge that has evaded researchers is the ability to support the metabolically demanding cardiomyocytes at cell densities reflective of the native myocardium[186]. In the human heart, every myocardial cell is within 20 μm of a perfused capillary[188] to facilitate transport of nutrients and oxygen to and wastes from the parenchyma. Second is the directed generation of the complex double-helix fiber architecture of the myocardium. It is known that the helical architecture of the heart enhances the contractility of bulk tissue[189,190] to generate efficient pumping[191,192].

Supplying cardiac tissues with adequate nutrients and building orientation and structure might both be achieved by constructing user-defined vasculature within cardiac tissue engineering constructs. Endothelialization of artificial blood vessels and co-culture of endothelial

cells with cardiomyocytes have been shown to regulate CM contraction, promote survival[193], guide orientation[194], and modulate maturation via the production and release of growth factors[195]. Furthermore, endothelial cells have been shown to promote synthesis of connexin 43, enhance coordinated contraction of CMs, and maintain electrical stability of cardiac tissue[193]. Having created functional cardiac tissues in PEG hydrogels and having developed means to generate robust user-defined blood vessels in cell-laden PEG hydrogels, we should be encouraged to construct cardiac tissues with helical vasculature. It is likely that defined vascular architectures and void spaces can guide CM orientation and encourage helical tissue formation, as well as promote maturation, coordinated contraction and electrical synchronization.

2. *Renal Tissue Engineering*

While vascularization of cardiac tissues may be the next obvious application of either photo-mediated fabrication technique, it is not the only high-impact application. Chronic kidney disease, as previously described, is a major health concern afflicting nearly 10% of the world's population with a growing waiting list of patients in need of kidney transplant and a stagnant number of donors[53]. Findings in Chapter 4 and work by the Freedman lab have demonstrated a capacity to create self-organizing kidney organoids from hPSCs, suggesting that regenerative medicine solutions might be used to both study renal disease[62] and create replacement tissues[61]. Yet unlike cardiac tissue engineering, renal tissue engineering remains nascent. Kidney organoids, though self-organizing, have not demonstrated a capacity to function as they require complex vasculature and tubule organization to perform any measurable filtration. Vasculature in the kidney both supplies these tissues with nutrients and participates in the

filtration process. Blood from the renal arteries are distributed to both the renal cortex and medulla. In the glomerulus, vessels directly interact with nephron podocytes to allow for solute exchange, while the vessels of the vasa recta and peritubular capillaries participate in the countercurrent multiplication mechanism[196]. Though no experimental work has been conducted towards this specific application, it is possible that using either photodegradation or photoablation one could construct an endothelialized glomerulus or create void spaces to guide tubule development. Creating glomerulus-like structures in the proximity of encapsulated kidney organoids may encourage interaction between vessel and organoid and demonstrate an ability to filter fluids or reabsorb nutrients.

3. Malaria Biology and Capillary Improvements

Chapter 6 demonstrates the ability to study and better understand microvascular sequestration of *P. falciparum*-infected RBCs through the creation of engineered human capillaries. While we investigated the role of mechanical stiffening and cytoadhesion in sequestration, many pertinent questions are yet to be resolved with respect to signaling, vascular damage and inflammation, endothelial specificity, and geometry-dependent margination.

As previously mentioned, parasite binders specific to EPCR are correlated with cerebral malaria[103], however ICAM-1 and chondroitin sulfate A (CSA) binders as well as rosetting phenotypes have been implicated in severe disease and should be studied within our capillary model[197]. Differences between these binders regarding endothelial cell specificity[182], binding affinity, and differences in target ligand expression during states of inflammation provide a myriad of variables which can be isolated to determine those factors that give rise to tissue damage and clinical pathology.

First, differences in endothelial specificity can be studied by creating capillaries from different endothelial sources. While not shown here, we have successfully generated capillary networks using lung, brain, arteriole-derived, and venule-derived endothelial cells. Varying both binders and endothelial cell sources, it is likely that binding patterns will be significantly different depending on the combination of parasite and endothelial organ specificity. It has been observed that significant differences in affinity arise from different shear stress[93] as well as endothelial organ source which will likely give rise to very different sequestration patterns[182].

Second, rosetting (a phenomenon in which IRBCs bind to normal RBCs) and clumping (a CD36-binder and platelet-mediated aggregation of IRBCs) are believed to result in trapping and vaso-occlusion of small vessels[198]. These phenomena should also be studied in the capillary model. While these large aggregates demonstrate little to no cytoadhesive properties, their large size might induce mechanical trapping. No trapping was observed in our capillary model when utilizing trypsinized IT4var19 IRBCs, however both rosettes and IRBC clumps may incur tissue damage and occlusion.

In terms of hemodynamics, we hypothesized that the high sequestration of 2G2 IRBCs focused at the post-capillary venule in our devices was largely a consequence of margination, wherein non-deformable IRBCs were pushed toward the vessel wall[112]. This speculation can be proved through experimentation and the engineering criteria giving rise to these observations should be determined. This can be measured by performing similar particle tracking as was conducted during the single cell experiments of Chapter 6 but applied to IRBCs diluted in solutions of physiological hematocrits. It is likely that margination will be observed, however to determine the geometric and size dependent nature of this phenomenon, vessel geometry, aspect ratio, and scale can be modified and compared with theoretical flow models.

In terms of pathology and tissue damage, it would be difficult to study vessel permeability, inflammation, and exudate transport as our devices tend to be solute-permeable. Endothelial barrier dysfunction most likely indicates either a state of moderate endothelial activation or incomplete wall coverage. While the source of these leaks is unclear, others have demonstrated strong barrier properties in analogous soft-lithography injection molded devices by using an interpenetrating agarose-gelatin hydrogel network chemically crosslinked together[199]. Though these systems do not permit the encapsulation of cells in the bulk hydrogel and are significantly stiffer than native vasculature, intact vascular networks with strong tight junctions can be generated. As our photoablation technique can be performed in most hydrogel constructs, we might consider utilizing biomaterials other than collagen to create more stable vessels and then use multiphoton photoablation to create capillary networks. Using devices that permit the investigation of fluid and protein leakage upon insult would allow us to study the effects and signaling associated with IRBC sequestration and inflammation. These experiments would be critical as expression of prominent PfEMP1 ligands like ICAM-1 are highly inflammation-dependent[200]. Finally, these models would also allow us to test the efficacy of small-molecule modulators of endothelial cell signaling, using permeability as a proxy for tissue and vessel damage.

4. Sickle Cell Anemia and Hematologic Disease

As described in Chapter 6, unique capillary specific hemodynamic, flow, and pathologies arise at the capillary level because of their size and geometry. By design of its small cross-sectional area (diameter ~ 5-10 μm) and single cell layered endothelium, all relevant mass

transport occurs exclusively at the capillary including: pulmonary gas exchange, gut nutrient absorption and renal filtration. Pathologic alterations to blood constituent structure, mechanics and propensity to coagulate can manifest in widespread tissue damage originating at the capillary[201]. While malaria is one such instance, there are many blood and vasculature related diseases focused at the microvasculature.

Based on findings in chapter 6, interesting biophysical experiments could be conducted to study vaso-occlusion associated with sickle cell disease, spherocytosis, and elliptocytosis, wherein hereditary or *de novo* mutations in spectrin, ankyrin, or other membrane and cytoskeletal proteins give rise to abnormal RBC deformability and mechanics[202]. Comparison with IRBCs and their resultant sequestration may both further validate the capillary model and provide insight into the constraints that determine occlusion. Further investigation involving endothelial cell signaling may also highlight the pathologic differences specific to sequestration as compared with vaso-occlusion.

Though hematologic disease is a clear next direction for capillary work, other critical pathologies also arise within small vessels. Abnormalities in biochemical signaling, metabolic, and infection are just a few of the many disease states which could be studied within our capillary devices. Stroke, diabetic mellitus associated vascular disease and disseminated intravascular coagulation all require a capillary model to study disease.

C. Closing

The future of regenerative medicine is optimistic with tissue engineering solutions to remedy and better understand pathology just on the horizon. It is critical that we as engineers, biologists, and physicians remain dedicated to expand our knowledge of both physiology and disease through active collaboration. As reiterated throughout this thesis, those mechanisms that sustain life are complex and to understand them requires intricate knowledge of all components and their dynamic interactions. As no one individual is capable nor tasked to broadly understand all of medicine or biological function, only through a genuine and concerted effort can we as a community continue to create innovative tools and effective therapies.

CHAPTER 8: REFERENCES

[1] C. Frantz, K. M. Stewart, V. M. Weaver, *J. Cell Sci.* **2010**, *123*, 4195.

[2] H. Bae, A. S. Puranik, R. Gauvin, F. Edalat, B. Carrillo-Conde, N. A. Peppas, A. Khademhosseini, *Sci. Transl. Med.* **2012**, *4*, 160ps23.

[3] G. C. Gurtner, S. Werner, Y. Barrandon, M. T. Longaker, *Nature* **2008**, *453*, 314.

[4] S. F. Gilbert, *Developmental Biology*, Sinauer Associates, **2000**.

[5] T. Brade, J. Männer, M. Kühl, *Cardiovasc. Res.* **2006**, *72*, 198.

[6] C. K. Arakawa, C. A. DeForest, *Biol. Eng. Stem Cell Niches* **2017**, 295.

[7] C. Bonnans, J. Chou, Z. Werb, *Nat. Rev. Mol. Cell Biol.* **2014**, *15*, 786.

[8] R. Akhtar, M. J. Sherratt, J. K. Cruickshank, B. Derby, *Mater. Today* **2011**, *14*, 96.

[9] F. Gattazzo, A. Urciuolo, P. Bonaldo, *Biochim. Biophys. Acta - Gen. Subj.* **2014**, *1840*, 2506.

[10] D. G. Belair, N. N. Le, W. L. Murphy, *Chem. Commun.* **2014**, *50*, 15651.

[11] M. Xue, C. J. Jackson, *Adv. wound care* **2015**, *4*, 119.

[12] J. D. Humphries, A. Byron, M. J. Humphries, *J. Cell Sci.* **2006**, *119*, 3901.

[13] D. S. Harburger, D. A. Calderwood, *J. Cell Sci.* **2009**, *122*, 159.

[14] F. G. Spinale, H. Nagase, *Circ. Res.* **2002**, *90*, 520.

[15] M. W. Tibbitt, K. S. Anseth, *Biotechnol. Bioeng.* **2009**, *103*, 655.

[16] S. R. Caliari, J. A. Burdick, *Nat. Methods* **2016**, *13*, 405.

[17] C. A. Deforest, K. S. Anseth, *Annu. Rev. Chem. Biomol. Eng* **2012**, *3*, 421.

[18] I. Tomatsu, K. Peng, A. Kros, *Adv. Drug Deliv. Rev.* **2011**, *63*, 1257.

[19] C. A. DeForest, K. S. Anseth, *Nat. Chem.* **2011**, *3*, 925.

[20] P. B. Malafaya, G. A. Silva, R. L. Reis, *Adv. Drug Deliv. Rev.* **2007**, *59*, 207.

[21] J. K. Mouw, G. Ou, V. M. Weaver, *Nat. Rev. Mol. Cell Biol.* **2014**, *15*, 771.

[22] T. Elsdale, J. Bard, *J. Cell Biol.* **1972**, *54*, 626.

[23] T. Eschenhagen, C. Fink, U. Remmers, H. Scholz, J. Wattchow, J. Weil, W. Zimmermann, H. H. Dohmen, H. Schäfer, N. Bishopric, T. Wakatsuki, E. L. Elson, *FASEB J.* **1997**, *11*, 683.

[24] J. S. Graham, A. N. Vomund, C. L. Phillips, M. Grandbois, *Exp. Cell Res.* **2004**, *299*, 335.

[25] H. K. Kleinman, G. R. Martin, *Semin. Cancer Biol.* **2005**, *15*, 378.

[26] C. S. Hughes, L. M. Postovit, G. A. Lajoie, *Proteomics* **2010**, *10*, 1886.

[27] J. Israelachvili, **1997**, *94*, 8378.

[28] L. Griffith, *Acta Mater.* **2000**, *48*, 263.

[29] J. A. Burdick, K. S. Anseth, *Biomaterials* **2002**, *23*, 4315.

[30] J. Zhu, *Biomaterials* **2010**, *31*, 4639.

[31] P. M. Kharkar, K. L. Kiick, A. M. Kloxin, *Chem. Soc. Rev.* **2013**, *42*, 7335.

[32] H. C. Kolb, M. G. Finn, K. B. Sharpless, *Angew. Chem. Int. Ed. Engl.* **2001**, *40*, 2004.

[33] D. L. Alge, M. A. Azagarsamy, D. F. Donohue, K. S. Anseth, *Biomacromolecules* **2013**, *14*, 949.

[34] J. Lahann, *Click Chemistry for Biotechnology and Materials Science*, Wiley, **2009**.

[35] Y. Jiang, J. Chen, C. Deng, E. J. Suuronen, Z. Zhong, *Biomaterials* **2014**, *35*, 4969.

[36] C. Chang, Z. Werb, *Trends Cell Biol.* **2001**, *11*, S37.

[37] H. Nagase, G. B. Fields, *Biopolymers* **1996**, *40*, 399.

[38] J. Patterson, J. A. Hubbell, *Biomaterials* **2010**, *31*, 7836.

[39] G. D. Nicodemus, S. J. Bryant, *Tissue Eng. Part B Rev.* **2008**, *14*, 149.

[40] R. Chandrawati, *Exp. Biol. Med. (Maywood).* **2016**, *241*, 972.

[41] G. Pasparakis, T. Manouras, P. Argitis, M. Vamvakaki, *Macromol. Rapid Commun.* **2012**, *33*, 183.

[42] E. R. Ruskowitz, C. A. DeForest, *Nat. Rev. Mater.* **2018**, *3*, 17087.

[43] S. Karthik, N. Puvvada, B. N. P. Kumar, S. Rajput, A. Pathak, M. Mandal, N. D. P. Singh, *ACS Appl. Mater. Interfaces* **2013**, *5*, 5232.

[44] K. T. Nguyen, J. L. West, *Biomaterials* **2002**, *23*, 4307.

[45] J. A. Benton, C. A. DeForest, V. Vivekanandan, K. S. Anseth, *Tissue Eng. Part A* **2009**, *15*, 3221.

[46] A. A. Aimetti, A. J. Machen, K. S. Anseth, *Biomaterials* **2009**, *30*, 6048.

[47] J. Hu, Y. Hou, H. Park, B. Choi, S. Hou, A. Chung, M. Lee, *Acta Biomater.* **2012**, *8*, 1730.

[48] S. L. Murphy, J. Xu, K. D. Kochanek, *Natl. Vital Stat. Rep.* **2013**, *61*, 1.

[49] A. S. Go, D. Mozaffarian, V. L. Roger, E. J. Benjamin, J. D. Berry, M. J. Blaha, S. Dai, E. S. Ford, C. S. Fox, S. Franco, H. J. Fullerton, C. Gillespie, S. M. Hailpern, J. A. Heit, V. J. Howard, M. D. Huffman, S. E. Judd, B. M. Kissela, S. J. Kittner, D. T. Lackland, J. H. Lichtman, L. D. Lisabeth, R. H. Mackey, D. J. Magid, G. M. Marcus, A. Marelli, D. B. Matchar, D. K. McGuire, E. R. Mohler, C. S. Moy, M. E. Mussolino, R. W. Neumar, G. Nichol, D. K. Pandey, N. P. Paynter, M. J. Reeves, P. D. Sorlie, J. Stein, A. Towfighi, T. N. Turan, S. S. Virani, N. D. Wong, D. Woo, M. B. Turner, *Circulation* **2014**, *129*, e28.

[50] B. Ovbiagele, L. B. Goldstein, R. T. Higashida, V. J. Howard, S. C. Johnston, O. A. Khavjou, D. T. Lackland, J. H. Lichtman, S. Mohl, R. L. Sacco, J. L. Saver, J. G. Trogdon, *Stroke.* **2013**, *44*, 2361.

[51] P. W. Burridge, E. Matsa, P. Shukla, Z. C. Lin, J. M. Churko, A. D. Ebert, F. Lan, S. Diecke, B. Huber, N. M. Mordwinkin, J. R. Plews, O. J. Abilez, B. Cui, J. D. Gold, J. C. Wu, *Nat. Methods* **2014**, *11*, 855.

[52] N. J. Palpant, L. Pabon, C. E. Friedman, M. Roberts, B. Hadland, R. J. Zaunbrecher, I. Bernstein, Y. Zheng, C. E. Murry, *Nat. Protoc.* **2016**, *12*, 15.

[53] *Lancet* **2014**, *385*, 117.

[54] NIDDK, **2016**.

[55] B. S. Freedman, C. R. Brooks, A. Q. Lam, H. Fu, R. Morizane, V. Agrawal, A. F. Saad, M. K. Li, M. R. Hughes, R. Vander Werff, D. T. Peters, J. Lu, A. Baccei, A. M. Siedlecki, M. T. Valerius, K. Musunuru, K. M. McNagny, T. I. Steinman, J. Zhou, P. H. Lerou, J. V Bonventre, *Nat. Commun.* **2015**, *6*, 8715.

[56] M. Takasato, P. X. Er, H. S. Chiu, B. Maier, G. J. Baillie, C. Ferguson, R. G. Parton, E. J. Wolvetang, M. S. Roost, S. M. Chuva de Sousa Lopes, M. H. Little, *Nature* **2015**, *526*, 564.

[57] M. H. Little, *Kidney Development, Disease, Repair and Regeneration*, **n.d.**

[58] M. Takasato, P. X. Er, M. Becroft, J. M. Vanslambrouck, E. G. Stanley, A. G. Elefanty, M. H. Little, *Nat. Cell Biol.* **2014**, *16*, 118.

[59] Y. Xia, I. Sancho-Martinez, E. Nivet, C. Rodriguez Esteban, J. M. Campistol, J. C. Izpisua Belmonte, *Nat. Protoc.* **2014**, *9*, 2693.

[60] Y. Xia, E. Nivet, I. Sancho-Martinez, T. Gallegos, K. Suzuki, D. Okamura, M.-Z. Wu, I. Dubova, C. R. Esteban, N. Montserrat, J. M. Campistol, J. C. Izpisua Belmonte, *Nat. Cell Biol.* **2013**, *15*, 1507.

[61] R. Morizane, A. Q. Lam, B. S. Freedman, S. Kishi, M. T. Valerius, J. V Bonventre, *Nat. Biotechnol.* **2015**, *33*, 1193.

[62] N. M. Cruz, X. Song, S. M. Czerniecki, R. E. Gulieva, A. J. Churchill, Y. K. Kim, K. Winston, L. M. Tran, M. A. Diaz, H. Fu, L. S. Finn, Y. Pei, J. Himmelfarb, B. S. Freedman, *Nat. Mater.* **2017**, *16*, 1112.

[63] H. Naderi, M. M. Matin, A. R. Bahrami, *J. Biomater. Appl.* **2011**, *26*, 383.

[64] S. V Murphy, A. Atala, *Nat. Biotechnol.* **2014**, *32*, 773.

[65] Y.-J. Seol, H.-W. Kang, S. J. Lee, A. Atala, J. J. Yoo, *Eur. J. Cardiothorac. Surg.* **2014**, *46*, 342.

[66] K. Jakab, C. Norotte, F. Marga, K. Murphy, G. Vunjak-Novakovic, G. Forgacs, *Biofabrication* **2010**, *2*, 022001.

[67] J. S. Miller, K. R. Stevens, M. T. Yang, B. M. Baker, D.-H. T. Nguyen, D. M. Cohen, E. Toro, A. A. Chen, P. A. Galie, X. Yu, R. Chaturvedi, S. N. Bhatia, C. S. Chen, *Nat. Mater.* **2012**, *11*, 768.

[68] M. A. Roberts, S. S. Kotha, K. T. Phong, Y. Zheng, *J. Vis. Exp.* **2016**, e54457.

[69] Y. Zheng, J. Chen, J. A. López, P. Paulinska, A. Spiel, B. Jilma, H. M. Tsai, A. W. Tsai, S. F. De Meyer, B. De Maeyer, H. Deckmyn, K. Vanhoorelbeke, J. P. Giblin, L. J. Hewlett, M. J. Hannah, J. A. Van Mourik, W. T. R. de, J. Voorberg, J. F. Dong, E. Di Stasio, R. De Cristofaro, L. H. Nolasco, M. Schwameis, C. Schorgenhofer, A. Assinger, M. Steiner, B. Jilma, J. Chen, H. Shankaran, P. Alexandridis, S. Neelamegham, Y. Zheng, H. C. Han, Q. Liu, D. Mirc, B. M. Fu, L. Guglielmini, R. Rusconi, S. Lecuyer, H. A. Stone, M. Furlan, R. Robles, B. Lamie, K. Shim, P. J. Anderson, E. A. Tuley, E. Wiswall, J. E. Sadler, G. G. Levy, K. Kokame, M. Furlan, H. M. Tsai, E. C. Lian, D. W. Chung, M. Uemura, O. J. McCarty, M. Schouten, W. J. Wiersinga, M. Levi, T. van der Poll, G. E. Grau, H. Wolinsky, V. L. Cross, *Nat. Commun.* **2015**, *6*, 7858.

[70] L. E. Bertassoni, M. Cecconi, V. Manoharan, M. Nikkhah, J. Hjortnaes, A. L. Cristino, G. Barabaschi, D. Demarchi, M. R. Dokmeci, Y. Yang, A. Khademhosseini, *Lab Chip* **2014**, *14*, 2202.

[71] J. P. Morgan, P. F. Delnero, Y. Zheng, S. S. Verbridge, J. Chen, M. Craven, N. W. Choi, A. Diaz-Santana, P. Kermani, B. Hempstead, J. A. López, T. N. Corso, C. Fischbach, A.

D. Stroock, *Nat. Protoc.* **2013**, *8*, 1820.

[72] J. A. López, Y. Zheng, *J. Thromb. Haemost.* **2013**, *11 Suppl 1*, 67.

[73] Y. Zheng, J. Chen, M. Craven, N. W. Choi, S. Totorica, A. Diaz-Santana, P. Kermani, B. Hempstead, C. Fischbach-Teschl, J. A. López, A. D. Stroock, *Proc. Natl. Acad. Sci. U. S. A.* **2012**, *109*, 9342.

[74] M. A. Roberts, D. Tran, K. L. K. Coulombe, M. Razumova, M. Regnier, C. E. Murry, Y. Zheng, *Tissue Eng. Part A* **2016**, DOI 10.1089/ten.TEA.2015.0482.

[75] L. G. Griffith, M. A. Swartz, *Nat. Rev. Mol. Cell Biol.* **2006**, *7*, 211.

[76] *WHO* **2018**.

[77] S. R. Meshnick, T. E. Taylor, S. Kamchonwongpaisan, *Microbiol. Rev.* **1996**, *60*, 301.

[78] L. Roberts, *Science* **2016**, *352*, 398.

[79] M. Imwong, K. Suwannasin, C. Kunasol, K. Sutawong, M. Mayxay, H. Rekol, F. M. Smithuis, T. M. Hlaing, K. M. Tun, R. W. van der Pluijm, R. Tripura, O. Miotto, D. Menard, M. Dhorda, N. P. J. Day, N. J. White, A. M. Dondorp, *Lancet Infect. Dis.* **2017**, *17*, 491.

[80] R. Ataide, E. A. Ashley, R. Powell, J.-A. Chan, M. J. Malloy, K. O'Flaherty, E. Takashima, C. Langer, T. Tsuboi, A. M. Dondorp, N. P. Day, M. Dhorda, R. M. Fairhurst, P. Lim, C. Amaratunga, S. Pukrittayakamee, T. T. Hien, Y. Htut, M. Mayxay, M. A. Faiz, J. G. Beeson, F. Nosten, J. A. Simpson, N. J. White, F. J. I. Fowkes, *Proc. Natl. Acad. Sci.* **2017**, *114*, 3515.

[81] J. Burrows, *Nature* **2015**, *520*, 628.

[82] R. G. Ridley, *Nature* **2002**, *415*, 686.

[83] K. Marsh, *Lancet* **1998**, *352*, 924.

[84] L. H. Miller, H. C. Ackerman, X. Su, T. E. Wellems, *Nat. Med.* **2013**, *19*, 156.

[85] L. Roberts, *Science (80-.).* **2017**, DOI 10.1126/science.aar1899.

[86] A. Trampuz, M. Jereb, I. Muzlovic, R. M. Prabhu, *Crit. Care* **2003**, *7*, 315.

[87] V. Barrera, I. J. C. MacCormick, G. Czanner, P. S. Hiscott, V. A. White, A. G. Craig, N. A. V. Beare, L. H. Culshaw, Y. Zheng, S. C. Biddolph, D. A. Milner, S. Kamiza, M. E. Molyneux, T. E. Taylor, S. P. Harding, *Elife* **2018**, *7*, e32208.

[88] G. G. MacPherson, M. J. Warrell, N. J. White, S. Looareesuwan, D. A. Warrell, *Am. J.*

Pathol. **1985**, *119*, 385.

[89] N. J. White, G. D. H. Turner, N. P. J. Day, A. M. Dondorp, *J. Infect. Dis.* **2013**, *208*, 192.

[90] A. G. Maier, B. M. Cooke, A. F. Cowman, L. Tilley, *Nat. Rev. Microbiol.* **2009**, *7*, 341.

[91] N. J. White, *Malar. J.* **2017**, *16*, 88.

[92] M. Aikawa, M. Iseki, J. W. Barnwell, D. Taylor, M. M. Oo, R. J. Howard, *Am. J. Trop. Med. Hyg.* **1990**, *43*, 30.

[93] B. S. Crabb, B. M. Cooke, J. C. Reeder, R. F. Waller, S. R. Caruana, K. M. Davern, M. E. Wickham, G. V. Brown, R. L. Coppel, A. F. Cowman, *Cell* **1997**, *89*, 287.

[94] Y. Zhang, C. Huang, S. Kim, M. Golkaram, M. W. A. Dixon, L. Tilley, J. Li, S. Zhang, S. Suresh, *Proc. Natl. Acad. Sci.* **2015**, *112*, 6068.

[95] J. D. Smith, J. A. Rowe, M. K. Higgins, T. Lavstsen, *Cell. Microbiol.* **2013**, *15*, 1976.

[96] C. Mayer, L. Slater, M. C. Erat, R. Konrat, I. Vakonakis, *J. Biol. Chem.* **2012**, *287*, 7182.

[97] K. Flick, Q. Chen, *Mol. Biochem. Parasitol.* **2004**, *134*, 3.

[98] T. Lavstsen, L. Turner, F. Saguti, P. Magistrado, T. S. Rask, J. S. Jespersen, C. W. Wang, S. S. Berger, V. Baraka, A. M. Marquard, A. Seguin-Orlando, E. Willerslev, M. T. P. Gilbert, J. Lusingu, T. G. Theander, *Proc. Natl. Acad. Sci. U. S. A.* **2012**, *109*, E1791.

[99] J. H. Janes, C. P. Wang, E. Levin-Edens, I. Vigan-Womas, M. Guillotte, M. Melcher, O. Mercereau-Puijalon, J. D. Smith, *PLoS Pathog.* **2011**, *7*, e1002032.

[100] W. C. Aird, L. O. Mosnier, R. M. Fairhurst, *Blood* **2014**, *123*, 163.

[101] L. Turner, T. Lavstsen, S. S. Berger, C. W. Wang, J. E. V Petersen, M. Avril, A. J. Brazier, J. Freeth, J. S. Jespersen, M. A. Nielsen, P. Magistrado, J. Lusingu, J. D. Smith, M. K. Higgins, T. G. Theander, *Nature* **2013**, *498*, 502.

[102] M. Avril, A. J. Brazier, M. Melcher, S. Sampath, J. D. Smith, *PLoS Pathog.* **2013**, *9*, e1003430.

[103] M. Bernabeu, J. D. Smith, *Trends Parasitol.* **2017**, *33*, 295.

[104] N. J. White, S. Pukrittayakamee, T. T. Hien, M. A. Faiz, O. A. Mokuolu, A. M. Dondorp, *Lancet (London, England)* **2014**, *383*, 723.

[105] A. G. Craig, G. E. Grau, C. Janse, J. W. Kazura, D. Milner, J. W. Barnwell, G. Turner, J. Langhorne, on behalf of the participants of the H. R. meeting on "Animal M. for R. on S. participants of the Hinxton Retreat meeting on Animal Models for Research on Severe

Malaria, *PLoS Pathog.* **2012**, *8*, e1002401.

[106] B. Franke-Fayard, J. Fonager, A. Braks, S. M. Khan, C. J. Janse, *PLoS Pathog.* **2010**, *6*, e1001032.

[107] A. Moreno, J. L. Pérignon, S. Morosan, D. Mazier, A. Benito, *Trends Parasitol.* **2007**, *23*, 254.

[108] I. Angulo-Barturen, M. B. Jiménez-Díaz, T. Mulet, J. Rullas, E. Herreros, S. Ferrer, E. Jiménez, A. Mendoza, J. Regadera, P. J. Rosenthal, I. Bathurst, D. L. Pompliano, F. Gómez de las Heras, D. Gargallo-Viola, *PLoS One* **2008**, *3*, e2252.

[109] H. Fujioka, P. Millet, Y. Maeno, S. Nakazawa, Y. Ito, R. J. Howard, W. E. Collins, M. Aikawa, *Exp. Parasitol.* **1994**, *78*, 371.

[110] R. Udomsangpetch, A. E. Brown, C. D. Smith, H. K. Webster, *Am. J. Trop. Med. Hyg.* **1991**, *44*, 399.

[111] B. al-Khedery, J. W. Barnwell, M. R. Galinski, *Mol. Cell* **1999**, *3*, 131.

[112] H. W. Hou, A. A. S. Bhagat, A. G. Lin Chong, P. Mao, K. S. Wei Tan, J. Han, C. T. Lim, *Lab Chip* **2010**, *10*, 2605.

[113] P. Gascoyne, J. Satayavivad, M. Ruchirawat, *Acta Trop.* **2004**, *89*, 357.

[114] M. E. Warkiani, A. K. P. Tay, B. L. Khoo, X. Xiaofeng, J. Han, C. T. Lim, *Lab Chip* **2015**, *15*, 1101.

[115] S. Muñoz-Descalzo, A. K. Hadjantonakis, A. M. Arias, *Semin. Cell Dev. Biol.* **2015**, *47–48*, 101.

[116] Y. Lei, D. Jeong, J. Xiao, D. V Schaffer, *Cell. Mol. Bioeng.* **2014**, *7*, 172.

[117] B. A. Badeau, M. P. Comerford, C. K. Arakawa, J. A. Shadish, C. A. DeForest, *Nat. Chem.* **2018**, DOI 10.1038/nchem.2917.

[118] T. R. Cox, J. T. Erler, *Dis. Model. Mech.* **2011**, *4*, 165.

[119] C. A. DeForest, B. D. Polizzotti, K. S. Anseth, *Nat. Mater.* **2009**, *8*, 659.

[120] E. Ruoslahti, *Annu. Rev. Cell Dev. Biol.* **1996**, *12*, 697.

[121] W.-Z. Zhu, B. Van Biber, M. A. Laflamme, *Methods Mol. Biol.* **2011**, *767*, 419.

[122] S. D. Lundy, W.-Z. Zhu, M. Regnier, M. A. Laflamme, *Stem Cells Dev.* **2013**, *22*, 1991.

[123] A. Leonard, A. Bertero, J. D. Powers, K. M. Beussman, S. Bhandari, M. Regnier, C. E.

Murry, N. J. Sniadecki, *J. Mol. Cell. Cardiol.* **2018**, *118*, 147.

[124] C. A. DeForest, D. A. Tirrell, *Nat. Mater.* **2015**, *14*, 523.

[125] C. K. Arakawa, B. A. Badeau, Y. Zheng, C. A. DeForest, *Adv. Mater.* **2017**, *29*, 1703156.

[126] P. E. Farahani, S. M. Adelmund, J. A. Shadish, C. A. DeForest, *J. Mater. Chem. B* **2017**, *5*, 4435.

[127] J. K. Van Camp, S. Beckers, D. Zegers, W. Van Hul, *Stem Cell Rev. Reports* **2014**, *10*, 207.

[128] R. M. Arkell, N. Fossat, P. P. L. Tam, *Curr. Opin. Genet. Dev.* **2013**, *23*, 454.

[129] G. Murry, Charles; Keller, *Cell* **2008**, *132*, 661.

[130] X. Lian, J. Zhang, S. M. Azarin, K. Zhu, L. B. Hazeltine, X. Bao, C. Hsiao, T. J. Kamp, S. P. Palecek, *Nat. Protoc.* **2013**, *8*, 162.

[131] M. A. Laflamme, K. Y. Chen, A. V Naumova, V. Muskheli, J. A. Fugate, S. K. Dupras, H. Reinecke, C. Xu, M. Hassanipour, S. Police, C. O'Sullivan, L. Collins, Y. Chen, E. Minami, E. A. Gill, S. Ueno, C. Yuan, J. Gold, C. E. Murry, *Nat. Biotechnol.* **2007**, *25*, 1015.

[132] P. Carmeliet, *Nat. Med.* **2000**, *6*, 389.

[133] L. Coultas, K. Chawengsaksophak, J. Rossant, *Nature* **2005**, *438*, 937.

[134] R. K. Jain, *Nat. Med.* **2003**, *9*, 685.

[135] C. Michiels, *J. Cell. Physiol.* **2003**, *196*, 430.

[136] A. Hasan, A. Paul, N. E. Vrana, X. Zhao, A. Memic, Y.-S. Hwang, M. R. Dokmeci, A. Khademhosseini, *Biomaterials* **2014**, *35*, 7308.

[137] W. Jia, P. S. Gungor-Ozkerim, Y. S. Zhang, K. Yue, K. Zhu, W. Liu, Q. Pi, B. Byambaa, M. R. Dokmeci, S. R. Shin, A. Khademhosseini, *Biomaterials* **2016**, *106*, 58.

[138] S. Khalil, W. Sun, *J. Biomech. Eng.* **2009**, *131*, 111002.

[139] W. Zhu, X. Qu, J. Zhu, X. Ma, S. Patel, J. Liu, P. Wang, C. S. E. Lai, M. Gou, Y. Xu, K. Zhang, S. Chen, *Biomaterials* **2017**, *124*, 106.

[140] V. K. Lee, D. Y. Kim, H. Ngo, Y. Lee, L. Seo, S.-S. Yoo, P. A. Vincent, G. Dai, *Biomaterials* **2014**, *35*, 8092.

[141] S. Bersini, I. K. Yazdi, G. Talò, S. R. Shin, M. Moretti, A. Khademhosseini, *Biotechnol.*

Adv. **2016**, *34*, 1113.

[142] Y. Nahmias, R. E. Schwartz, C. M. Verfaillie, D. J. Odde, *Biotechnol. Bioeng.* **2005**, *92*, 129.

[143] A. M. Kloxin, A. M. Kasko, C. N. Salinas, K. S. Anseth, *Science* **2009**, *324*, 59.

[144] N. Brandenberg, M. P. Lutolf, *Adv. Mater.* **2016**, *28*, 7450.

[145] K. A. Heintz, M. E. Bregenzer, J. L. Mantle, K. H. Lee, J. L. West, J. H. Slater, *Adv. Healthc. Mater.* **2016**, *5*, 2153.

[146] C. A. DeForest, K. S. Anseth, *Angew. Chemie - Int. Ed.* **2012**, *51*, 1816.

[147] P. Joshi, C. Y. Chung, I. Aukhil, H. P. Erickson, *J. Cell Sci.* **1993**, 389.

[148] E. Iivanainen, V.-M. Kähäri, J. Heino, K. Elenius, *Microsc. Res. Tech.* **2003**, *60*, 13.

[149] P. R. Somanath, N. L. Malinin, T. V Byzova, *Angiogenesis* **2009**, *12*, 177.

[150] C. Yang, M. W. Tibbitt, L. Basta, K. S. Anseth, *Nat. Mater.* **2014**, *13*, 645.

[151] M. W. Tibbitt, A. M. Kloxin, K. U. Dyamenahalli, K. S. Anseth, *Soft Matter* **2010**, *6*, 5100.

[152] R. K. Jain, T. Stylianopoulos, *Nat. Rev. Clin. Oncol.* **2010**, *7*, 653.

[153] R. K. Jain, *Science* **2005**, *307*, 58.

[154] D.-H. Kim, K. Han, K. Gupta, K. W. Kwon, K.-Y. Suh, A. Levchenko, *Biomaterials* **2009**, *30*, 5433.

[155] D.-H. Kim, E. A. Lipke, P. Kim, R. Cheong, S. Thompson, M. Delannoy, K.-Y. Suh, L. Tung, A. Levchenko, *Proc. Natl. Acad. Sci. U. S. A.* **2010**, *107*, 565.

[156] C.-H. Lin, Y.-H. Hsiao, H.-C. Chang, C.-F. Yeh, C.-K. He, E. M. Salm, C. Chen, I.-M. Chiu, C.-H. Hsu, *Lab Chip* **2015**, *15*, 2928.

[157] H. S. Kim, T. P. Devarenne, A. Han, *Lab Chip* **2015**, *15*, 2467.

[158] M. B. Esch, D. J. Post, M. L. Shuler, T. Stokol, *Tissue Eng. Part A* **2011**, *17*, 2965.

[159] E. D. Goddard-Borger, R. V. Stick, *Org. Lett.* **2007**, *9*, 3797.

[160] R. Chapman, K. A. Jolliffe, S. Perrier, *Aust. J. Chem.* **2010**, *63*, 1169.

[161] World Health Organization, *World Malaria Report 2015*, **2015**.

[162] M. Bernabeu, J. D. Smith, *Trends Parasitol.* **2017**, *33*, 295.

[163] A. M. Dondorp, *Transfus. Clin. Biol.* **2008**, *15*, 56.

[164] M. J. Ponsford, I. M. Medana, P. Prapansilp, T. T. Hien, S. J. Lee, A. M. Dondorp, M. M. Esiri, N. P. J. Day, N. J. White, G. D. H. Turner, *J. Infect. Dis.* **2012**, *205*, 663.

[165] H. Ishioka, A. Ghose, P. Charunwatthana, R. Maude, K. Plewes, H. Kingston, B. Intharabut, C. Woodrow, K. Chotivanich, A. A. Sayeed, M. U. Hasan, N. P. Day, A. Faiz, N. J. White, A. Hossain, A. M. Dondorp, *J. Infect. Dis.* **2016**, *213*, 788.

[166] B. Franke-Fayard, J. Fonager, A. Braks, S. M. Khan, C. J. Janse, *PLoS Pathog.* **2010**, *6*, e1001032.

[167] J. P. Shelby, J. White, K. Ganesan, P. K. Rathod, D. T. Chiu, *Proc. Natl. Acad. Sci.* **2003**, DOI 10.1073/pnas.2433968100.

[168] S. M. Hosseini, J. J. Feng, *Biophys. J.* **2012**, *103*, 1.

[169] V. L. Cross, Y. Zheng, N. Won Choi, S. S. Verbridge, B. A. Sutermaster, L. J. Bonassar, C. Fischbach, A. D. Stroock, *Biomaterials* **2010**, *31*, 8596.

[170] J. P. Morgan, P. F. Delnero, Y. Zheng, S. S. Verbridge, J. Chen, M. Craven, N. W. Choi, A. Diaz-Santana, P. Kermani, B. Hempstead, J. A. López, T. N. Corso, C. Fischbach, A. D. Stroock, *Nat. Protoc.* **2013**, *8*, 1820.

[171] J. Escaned, A. Flores, P. Garcia-Pavia, J. Segovia, J. Jimenez, P. Aragoncillo, C. Salas, F. Alfonso, R. Hernandez, D. J. Angiolillo, P. Jimenez-Quevedo, C. Banuelos, L. Alonso-Pulpon, C. Macaya, *Circulation* **2009**, *120*, 1561.

[172] V. L. Cross, Y. Zheng, N. Won Choi, S. S. Verbridge, B. A. Sutermaster, L. J. Bonassar, C. Fischbach, A. D. Stroock, *Biomaterials* **2010**, *31*, 8596.

[173] D. Kleinfeld, P. P. Mitra, F. Helmchen, W. Denk, *Proc. Natl. Acad. Sci.* **1998**, *95*, 15741.

[174] R. Skalak, P. I. Branemark, *Science* **1969**, *164*, 717.

[175] L. Lanotte, J. Mauer, S. Mendez, D. A. Fedosov, J.-M. Fromental, V. Claveria, F. Nicoud, G. Gompper, M. Abkarian, *Proc. Natl. Acad. Sci. U. S. A.* **2016**, *113*, 13289.

[176] N. F. Zeng, W. D. Ristenpart, *Biomicrofluidics* **2014**, *8*, 064123.

[177] B. G. Yipp, M. J. Hickey, G. Andonegui, A. G. Murray, S. Looareesuwan, P. Kubes, M. Ho, *Microcirculation* **2007**, *14*, 593.

[178] Y. Imai, K. Nakaaki, H. Kondo, T. Ishikawa, C. Teck Lim, T. Yamaguchi, *J. Biomech.* **2011**, DOI 10.1016/j.jbiomech.2011.02.084.

[179] L. T. Chen, L. Weiss, *Blood* **1973**, *41*, 529.

[180] J. Lou, R. Lucas, G. E. Grau, *Clin. Microbiol. Rev.* **2001**, *14*, 810.

[181] J. H. Janes, C. P. Wang, E. Levin-Edens, I. Vigan-Womas, M. Guillotte, M. Melcher, O. Mercereau-Puijalon, J. D. Smith, *PLoS Pathog.* **2011**, *7*, DOI 10.1371/journal.ppat.1002032.

[182] M. Avril, A. K. Tripathi, A. J. Brazier, C. Andisi, J. H. Janes, V. L. Soma, D. J. Sullivan, P. C. Bull, M. F. Stins, J. D. Smith, *Proc. Natl. Acad. Sci.* **2012**, *109*, E1782.

[183] P. Kovesi, "MATLAB and Octave Functions for Computer Vision and Image Processing.," **2000**.

[184] J. C. Crocker, E. R. Weeks, "Particle tracking using IDL," **2010**.

[185] S. J. Bryant, C. R. Nuttelman, K. S. Anseth, *J. Biomater. Sci. Polym. Ed.* **2000**, *11*, 439.

[186] G. Vunjak-Novakovic, N. Tandon, A. Godier, R. Maidhof, A. Marsano, T. P. Martens, M. Radisic, *Tissue Eng. Part B. Rev.* **2010**, *16*, 169.

[187] S. Y. Lim, D. Hernández, G. J. Dusting, *J. Cardiovasc. Pharmacol.* **2013**, *62*, 122.

[188] B. Korecky, C. M. Hai, K. Rakusan, *Can. J. Physiol. Pharmacol.* **1982**, *60*, 23.

[189] F. Poveda, D. Gil, E. Martí, A. Andaluz, M. Ballester, F. Carreras, *Rev. Esp. Cardiol. (Engl. Ed).* **2013**, *66*, 782.

[190] A. A. Young, B. R. Cowan, *J. Cardiovasc. Magn. Reson.* **2012**, *14*, 49.

[191] F. Y. Chen, L. H. Cohn, *Cardiol. Rev. 10*, 326.

[192] M. J. Kocica, A. F. Corno, F. Carreras-Costa, M. Ballester-Rodes, M. C. Moghbel, C. N. C. Cueva, V. Lackovic, V. I. Kanjuh, F. Torrent-Guasp, *Eur. J. Cardiothorac. Surg.* **2006**, *29 Suppl 1*, S21.

[193] H. Sekine, T. Shimizu, K. Hobo, S. Sekiya, J. Yang, M. Yamato, H. Kurosawa, E. Kobayashi, T. Okano, *Circulation* **2008**, *118*, S145.

[194] D. A. Narmoneva, R. Vukmirovic, M. E. Davis, R. D. Kamm, R. T. Lee, *Circulation* **2004**, *110*, 962.

[195] P. C. H. Hsieh, M. E. Davis, L. K. Lisowski, R. T. Lee, *Annu. Rev. Physiol.* **2006**, *68*, 51.

[196] M. L. S. Sequeira Lopez, in *Kidney Dev. Dis. Repair Regen.*, **2016**, pp. 147–162.

[197] J. A. Rowe, A. Claessens, R. A. Corrigan, M. Arman, *Expert Rev. Mol. Med.* **2009**, *11*,

e16.

[198] A. Pain, D. J. Ferguson, O. Kai, B. C. Urban, B. Lowe, K. Marsh, D. J. Roberts, *Proc. Natl. Acad. Sci. U. S. A.* **2001**, *98*, 1805.

[199] Y. Qiu, B. Ahn, Y. Sakurai, C. E. Hansen, R. Tran, P. N. Mimche, R. G. Mannino, J. C. Ciciliano, T. J. Lamb, C. H. Joiner, S. F. Ofori-Acquah, W. A. Lam, *Nat. Biomed. Eng.* **2018**, *2*, 453.

[200] P. G. Frank, M. P. Lisanti, *Am. J. Physiol. Heart Circ. Physiol.* **2008**, *295*, H926.

[201] A. G. B. Kovách, J. Hamar, L. Szabó, *Cardiovascular Physiology, Microcirculation and Capillary Exchange*, Elsevier Science, **1981**.

[202] M. D. Hoban, G. J. Cost, M. C. Mendel, Z. Romero, M. L. Kaufman, A. V Joglekar, M. Ho, D. Lumaquin, D. Gray, G. R. Lill, A. R. Cooper, F. Urbinati, S. Senadheera, A. Zhu, P.-Q. Liu, D. E. Paschon, L. Zhang, E. J. Rebar, A. Wilber, X. Wang, P. D. Gregory, M. C. Holmes, A. Reik, R. P. Hollis, D. B. Kohn, *Blood* **2015**, *125*, 2597.